STUDY OF LIGHT EXTRACTION AND CARRIER BEHAVIOR OF CADMIUM-FREE AND LEAD-FREE QUANTUM DOT LIGHT-EMITTING DIODES

ZHAO FANGQING

PhD

The Hong Kong Polytechnic University

2025

The Hong Kong Polytechnic University

Department of Applied Physics

Study of Light Extraction and Carrier Behavior of Cadmium-free and Lead-free Quantum Dot Light-Emitting Diodes

ZHAO Fangqing

A thesis submitted in partial fulfillment of the requirements for

the degree of Doctor of Philosophy

August 2024

CERTIFICATE OF ORIGINALITY

I hereby declare that this thesis is my own work and that, to the best of my knowledge and belief, it reproduces no material previously published or written, nor material that has been accepted for the award of any other degree or diploma, except where due acknowledgement has been made in the text.

_____ (Signed)

ZHAO Fangqing (Name of student)

Abstract

Quantum dots (QDs) and their light-emitting diodes (LEDs) have shown great potential in the display industry. However, the well-studied cadmium based QDs and perovskite nanocrystals contain elements such as cadmium and lead, which pose significant threats to the environment and human health, thereby limiting their broader application. In contrast, cadmium-free and lead-free QDs and their light-emitting diodes show greater potential.

In recent years, significant research efforts have been directed toward the development of cadmium-free and lead-free quantum dot light-emitting diodes (QLEDs). Despite these efforts, the performance of cadmium-free and lead-free QLEDs, particularly in the blue and green spectral regions, remains below the thresholds required for commercialization. Indium phosphide (InP) and zinc selenide (ZnSe) QD materials have emerged as promising cadmium-free and lead-free candidates for constructing high-performance QLED emissive layers (EML), especially for blue and green QLED applications.

Enhancing light extraction efficiency and optimizing carrier behavior in the EML are two key factors for achieving high-performance QLEDs. To achieve good external quantum efficiency (EQE), this thesis focuses on the working mechanisms of cadmium-free and lead-free QLEDs concerning the above two factors and proposes strategies for efficiency improvement, leading to several innovative results.

Firstly, we analyzed the light extraction modes within the cadmium-free and lead-free QLEDs and proposed a combined scheme to improve light extraction efficiency under limited internal quantum efficiency (IQE), thereby obtaining higher-performing QLEDs. The thesis presents an effective comprehensive strategy, involving the addition of an appropriately thick spacer layer, high-index substrates, and substrate surface roughening to sequentially extract light from the SPP mode, waveguide mode, and substrate mode to the air mode of QLEDs. This combined scheme promotes optical transmission between modes within the device through optical tunneling and microcavity design. After optimization, the light extraction efficiency (LEE) was significantly improved, resulting in an EQE increase from 6.64% to 18.50% for blue ZnSe QLEDs. Approximately threefold EQE improvement provides a more universal optical optimization strategy for cadmium-free and lead-free QLEDs.

To address the issue of efficiency reduction due to unbalanced carrier injection in cadmium-free and lead-free QLEDs, an innovative design based on an electric dipole layer was proposed to enhance hole injection. An innovative electric dipole layer material, 2,2'-(perfluoronaphthalene-2,6-diylidene)dimalononitrile (F6-TCNNQ), was also applied to cadmium-free and lead-free QLEDs. The strong forward-built electric field significantly facilitates hole injection at the interface from the hole transport layer (HTL) to the emissive layer (EML). The introduction of F6-TCNNQ also regulates the interface energy level of the HTL, reducing the hole injection barrier to the emissive layer (EML). For blue ZnSe QLEDs with strong electron injection, this method bypasses the limitations of electron injection, thereby achieving a higher radiative

recombination rate. As a result, the optimized EQE of blue ZnSe QLEDs was increased from 7.44% to 12.71%.

To further enhance the efficiency of cadmium-free and lead-free QLEDs, the electron leakage mechanism was revealed and studied in depth using green InP QLEDs as an example to achieve less non-radiative recombination. An effective method was proposed to prevent electron leakage by applying LiF, which reduces the Fermi level difference between green InP QDs and the ITO anode. LiF modification not only suppressed electron leakage but also further enhanced hole injection through the tunneling effect. The optimized devices achieved more balanced carrier injection in the EML, resulting in the EQE increasing to a maximum of 9.14%.

This thesis explores cadmium-free and lead-free QLEDs with a focus on light extraction and carrier behavior. Based on an analysis of the working mechanisms, optimization strategies are proposed from both optical and electrical perspectives to achieve improved light extraction and better carrier behavior. The optimized cadmium-free and lead-free QLEDs exhibit higher EQE, making them more suitable for display applications. The mechanisms and strategies proposed in this thesis are expected to provide valuable insights for further advancements in the cadmium-free and lead-free QLEDs field.

List of Publications

1. Tianqi Zhang, **Fangqing Zhao**, Pai Liu, Yangzhi Tan, Xiangtian Xiao, Zhaojin Wang, Weigao Wang, Dan Wu, Xiao Wei Sun, Jianhua Hao, Guichuan Xing*, Kai Wang*, "Understanding and Hindering the Electron Leakage in Green InP Quantum-Dot Light-Emitting Diodes". ***Advanced Photonics Research*****,** 2023, 4(11): 2300146. (co-first author)
2. **Fangqing Zhao**, Jiahua Hao, Kai Wang*, "Cadmium-free and Lead-free Environment-friendly Blue Quantum Dots and Light-emitting Diodes". ***Chinese Journal of Liquid Crystals and Displays***, 2021, 36(1): 203-215. (Invited Paper)
3. **Fangqing Zhao**, Xiangtian Xiao, Fankai Zheng, Fumei Yang, Depeng Li, Jingrui Ma, Xiangwei Qu, Xiao Wei Sun, Jianhua Hao*, and Kai Wang*, "Enhancing Hole Injection by Electric Dipoles for Efficient Blue ZnSeTe Quantum Dot Light-emitting Diodes", 2025, under review.
4. **Fangqing Zhao**, Guanding Mei, Fankai Zheng, Fumei Yang, Weixiong Peng, Depeng Li, Yangzhi Tan, Jingrui Ma, Xiangwei Qu, Xiao Wei Sun*, Jianhua Hao*, and Kai Wang*, "Optical Tunneling Scheme under Low SPP Microcavities for Eco-friendly Blue ZnSe QLEDs", 2025, to be submitted. (co-first author)
5. Fankai Zheng, **Fangqing Zhao**, Depeng Li, Jingrui Ma, Dan Wu* and Kai Wang*, "Monolithic Integration of Indirect Electrically Pumped Colloidal Quantum Dot Light Source on Silicon Nitride Waveguide", ***IEEE Electron Device Letters***, 2025, 46(8), 1373–1376.

6. Fankai Zheng, **Fangqing Zhao**, Kai Wang*, "Colloidal Quantum Dot Light-Emitting Diode on Silicon Substrate Based on Grating Coupler", 2025, to be submitted.
7. Tianqi Zhang, Pai Liu, **Fangqing Zhao**, Yangzhi Tan, Jiayun Sun, Xiangtian Xiao, Zhaojin Wang, Qingqian Wang, Fangkai Zheng, Xiao Wei Sun, Dan Wu, Guichuan Xing*, Kai Wang*, "Electric Dipole Modulation for Boosting Carrier Recombination in Green InP QLEDs under Strong Electron Injection". ***Nanoscale Advances***, 2023, 5(2), 385–392. (Back cover)
8. Wenda Zhang, Yangzhi Tan, Xijian Duan, **Fangqing Zhao**, Haochen Liu, Wei Chen, Pai Liu, Xiaogang Liu, Kai Wang, Zhikuan Zhang, Xiao Wei Sun*, "High Quantum Yield Blue InP/ZnS/ZnS Quantum Dots Based on Bromine Passivation for Efficient Blue Light-Emitting Diodes". ***Advanced Optical Materials***, 2022: 2200685
9. Fumei Yang, Kam Lin Chan, Zehan Wu, **Fangqing Zhao**, Man Chung Wong, Sin-Yi Pang, Jianhua Hao*, "HF-free synthesis of high-entropy MXene-PVA composite film and its flexible nanogenerator". ***Science China Materials***, 2025, 68(8): 2860–2867.
10. Yangzhi Tan, Wenda Zhang, Xiangtian Xiao, Jiayun Sun, Jingrui Ma, Tianqi Zhang, Guanding Mei, Zhaojin Wang, **Fangqing Zhao**, Dan. Wu*, Wallace. C. H. Choy, Xiao Wei Sun*, Kai Wang*, "Enhancing Hole Injection by Electric Dipoles for Efficient Blue InP QLEDs". ***Applied Physics Letters***, vol.119, no.22, p.221105, 2021.

11. Taikang Ye, Siqi Jia, Zhaojin Wang, Rui Cai, Hongcheng Yang, **Fangqing Zhao**, Yangzhi Tan, Xiao Wei Sun, Dan Wu*, Kai Wang, "Fabrication of Highly Efficient Perovskite Nanocrystal Light-Emitting Diodes via Inkjet Printing". ***Micromachines***, 2022, 13(7): 983

Acknowledgements

I'd like to take this chance to sincerely thank everyone who has supported me along the way while I was working on this thesis.

First and foremost, I'm deeply grateful to my supervisors, Prof. Jianhua Hao and Prof. Kai Wang. From brainstorming research directions to polishing the final draft, they've been guiding me every step of the way. Whether it was helping me shape my research plan, giving practical suggestions on writing, or sharing their own rigorous approach to science, they've taught me far more than just how to finish a project — they've shown me what it means to do serious research. Their patience, high standards, and way of thinking have left a deep impression on me and made me realize how much more there is to learn and grow.

I also want to thank the amazing people in our research group. Dr. Guanding Mei, Dr. Tianqi Zhang and Dr. Xiangtian Xiao were incredibly helpful — from hands-on guidance in experiments to careful feedback on my writing, they were always there when I hit a wall. Mr. Fankai Zheng and Dr. Fumei Yang gave me many useful tips on data analysis, drawing scientific figures and improving thesis writing, which really helped improve the quality of my work. I'm also grateful to so many others in the group who patiently explained things, shared resources, or simply created a supportive atmosphere. To name just a few: Dr. Jianfeng Mao, Dr. Menglin Song, Dr. Sin Yi Pang,

Dr. Zehan Wu, Dr. Shang Li, Dr. Wenda Zhang, Mr. Yangzhi Tan, Dr. Jingrui Ma, Mr. Depeng Li, Mr. Jiayun Sun, Dr. Taikang Ye, Dr. Zhaojin Wang… Thank you all.

Finally, I want to thank my parents for always being there with their quiet support and unconditional love — it meant everything to me. And to my dear friends from PolyU, SUSTech, and Maydayland — thank you for all the laughs, late-night talks, and shoulders to lean on during the toughest moments. I couldn't have done this without you.

Thank you all, from the bottom of my heart.

“生命不是过程，而是美丽旅程”；每一段经历，都是予我的礼物。

在学业“百忙”下，能短暂几句随笔，竟已是十年前的高中时光。那时的知识紧凑精密，信息单调纯粹，文字细腻青涩，也会透着些青春感伤。如今百感交集，竟很难言喻。十年离家在外的学生时光，“多遥远，多纠结，多想念，多无法描写”，凝成一句感恩，暂存于此。

几张机票，将我曾经单线的生活，推向了广袤天地。每一步都是全新的，每个方向都有风景，每条道路都通向远方。走到这，才发现，原来只需埋头前进的道路，变得自由而未知。不再有固定的方向，不再有绝对的好坏，不再有唯一的标准，不再一定众望所归。曾慌张追赶怕垫底落后，却发现人人眼中瞄准不同方向；曾对大小选择瞻前顾后，却明白了对错在心各有所重；曾在标准要求条框里徘徊，却学会了挣脱隐形枷锁望向更高的山巅；曾清空灵魂目不窥园，却懂得了

恣意率性得其所哉。与其感恩学识增加几何，我更想感恩这些所有邀我探索世界的机会，所有容我停留重来的支持，所有伴我重新思考的遇见。

责任，是无私的指导和教引，是舍己的扶持和关切。善良，是慷慨的援手和合作，是无声的宽容和鼓励。感情，是坚定的陪伴和懂得，是坦率的提醒和支撑。爱，是永恒的托举和付出，是无保留的庇护和港湾。信念，是穿越时空的共鸣，是包罗万物的星火。这些词语好似华丽而虚无缥缈，却是我铭感五内的千万时刻，是一位位鲜活的人物在我读博几年生命中写下的万千故事，让我的每时每刻，都不虚此生。

“回忆是你我，生存的地方。最平凡日子，最值得珍藏。”眼下学生时代的终点时刻，会带着几年的读博时光，一同远去变成回忆。感恩这段经历里的每个瞬间，感恩每个灵魂每个人，感恩每秒心跳每滴泪，留下了好似改变许多现在的我，带着好似全新的思考和视角、勇敢和坚持，继续探索世界。

下一站，你的第二人生。

——敬谢郝建华教授、王恺教授两位导师，香港理工大学、南方科技大学两所高校，曾提供帮助的所有老师、同学、同门，所有小初高、大学、读博、共同爱好带来留下的朋友、闺蜜，永远支撑我的五月天，最最疼爱我的爸爸妈妈。

Table of Contents

List of Figures

List of Tables

Chapter 1 Introduction

1.1 Research background

The past two centuries have witnessed unprecedented industrial and technological advancements, driving a dramatic surge in global energy consumption and environmental degradation. As depicted in Figure 1.1(a), global energy demand skyrocketed from 8.6 billion tons of oil equivalent in 1990 to 15 billion tons by 2023—a staggering 75% increase. This growth is attributed not only to population expansion but also to the rise of energy-intensive industries and digital technologies. Despite efforts to transition toward renewables, fossil fuels such as coal and oil still account for over 80% of the global energy supply [Figure 1.1(b)], exacerbating carbon emissions and resource depletion. The International Energy Agency (IEA) estimates that without significant policy interventions, fossil fuel dominance will persist through 2050, underscoring the urgency for sustainable alternatives.

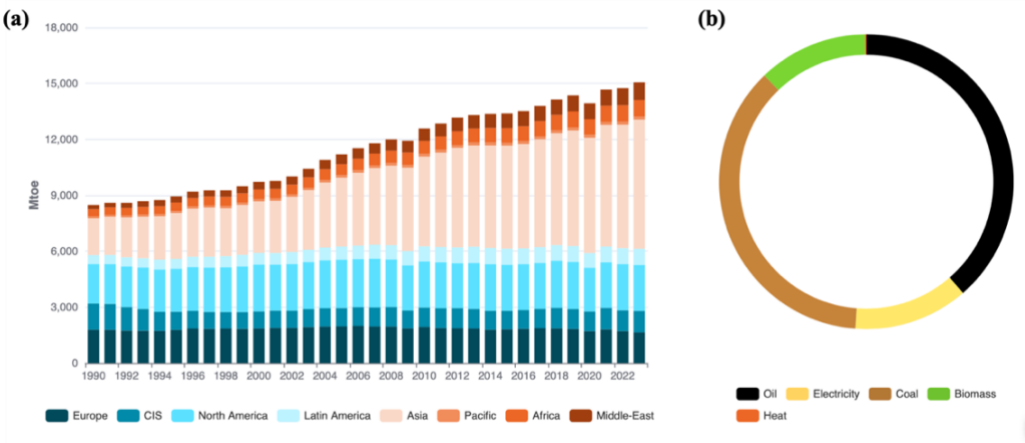

Figure 1.1 (a) Total energy consumption of the whole world from 1990 to 2023. (b) Major compositions of global energy supply in 2023.

(https://yearbook.enerdata.net/total-energy/world-consumption-statistics.html).

Parallel to this energy crisis is the rapid proliferation of digital devices. Smartphones, laptops, and AR/VR systems have become indispensable in modern life, yet their energy demands are substantial. For instance, the U.S. Energy Information Administration reported that displays and lighting consumed 20% of national electricity in 2012, equivalent to 844 billion kilowatt-hours. With the advent of 4K/8K screens and high-refresh-rate displays, this figure is projected to climb, further straining power grids. Traditional liquid crystal displays (LCDs), while cost-effective, suffer from inefficiencies: their reliance on backlighting results in over 95% energy loss due to polarizers and color filters. This inefficiency, combined with limited color gamut (72% National Television System Committee, NTSC), has spurred the search for advanced display technologies that balance performance with sustainability.[1]

Figure 1.2 Intelligent devices like smartphones, laptops, and augmented reality/virtual reality technology.

In today's digital information age, display technology plays a crucial role in the quality and efficiency of information presentation and human-computer interaction, making it an essential component of information transmission. The evolution of display technology from cathode ray tube displays to liquid crystal displays, and now to organic light-emitting diode (OLED) displays has been rapid. In recent years, there has been increasing interest in display technology based on quantum dot light-emitting diodes (QLEDs), which utilize colloidal quantum dot (QD) materials with excellent optoelectronic properties. This is considered one of the most promising directions in the display industry due to its potential for advancement. QLED has the advantages of wide viewing angle, thin size, wide color gamut, fast response speed, and low energy consumption like OLED, while QLED can achieve higher brightness, high stability，and longer lifetime.

1.2 Colloidal quantum dots (QDs)

Quantum dots (QDs) are semiconductor nanocrystals with quasi-zero-dimensional structures. Due to their small particle size, typically ranging from 3 nm to 10 nm, which is often smaller than the exciton Bohr radius, excitons are confined within this limited space, leading to quantum confinement effects. This confinement results in the energy levels of excitons becoming discrete, causing changes in the energy band. The bandwidth of QDs is not only related to the bandgap of the bulk material but also to the particle size. As a result, the same material can emit light of different wavelengths by adjusting the particle size. The emission wavelength of QDs can cover the entire visible

spectrum and extend into the near-infrared region, making them highly suitable for display applications. Additionally, QDs offer several advantages, such as a high quantum yield (QY) of over 90%, a narrow full width at half maximum (FWHM) of 20-35 nm, a wide color gamut exceeding 120% of NTSC, relatively low solution-based fabrication costs, and compatibility with inkjet printing processes[2,3]. Moreover, compared to organic luminescent materials, inorganic QD luminescent materials exhibit higher stability and brightness, making QLEDs a highly competitive candidate for next-generation display technology.

1.2.1 Fundamentals and unique properties

QDs are a class of semiconductor nanocrystals with quasi-zero-dimensional structures, whose unique physical and chemical properties arise from quantum confinement effects at the nanoscale. When the size of QDs (typically 1-20 nm) is smaller than the Bohr radius of excitons in bulk materials, the wavefunctions of electrons and holes are strongly confined in three-dimensional space, leading to the transition of energy levels from continuous states to discrete states. This quantum size effect not only makes the band gap of QDs directly related to their size but also endows them with tunable optical properties. For example, the emission wavelength of CdSe QDs can be continuously tuned from 2 nm (blue light, around 470 nm) to 6 nm (red light, around 630 nm) by adjusting the particle size. This size-dependent luminescent property enables QDs to cover the visible to near-infrared spectrum (400–2500 nm),

making them ideal materials for display, optoelectronics, and biological imaging applications.

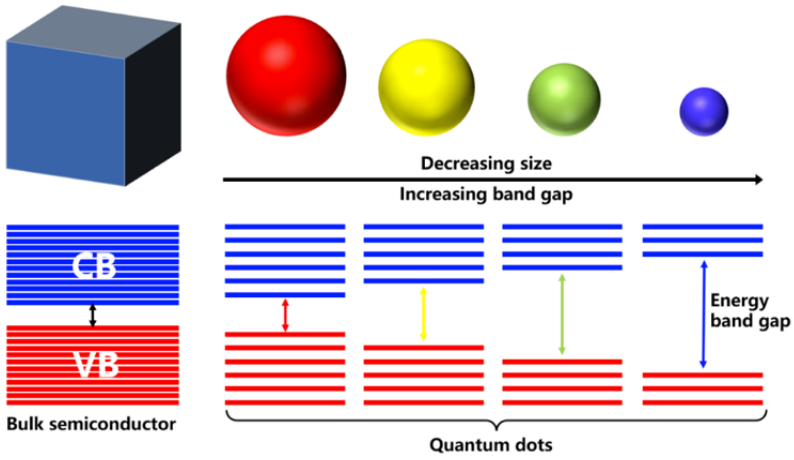

Figure 1.3 Diagram illustrating the quantum size effect[4]

A single QD is depicted in Figure. 1.4 (a) (image supported by Fullnano Ltd.). Structurally, QDs typically consist of three parts: Core: Composed of semiconductor materials (such as CdSe, ZnSeTe, InP), it is the main region for exciton recombination and light emission. The chemical composition and size of the core directly determine the band gap and emission wavelength of the QD, as a series of fluorescent QDs of different sizes shown in Figure. 1.4 (b). Shell: A wide-bandgap semiconductor layer (such as ZnS, CdS) that envelops the core, serving multiple functions: (1) passivating the surface defects of the core, reducing non-radiative recombination, and increasing the photoluminescence quantum yield (PLQY) from less than 10% for the bare core to over 90%; (2) enhancing the chemical stability of the QD, protecting it from erosion by oxygen, water, and electric fields. Ligands: Organic molecules also be used and adsorbed on the shell surface. Both oleic acid, dodecanethiol are widely used ligand materials. They prevent QD aggregation through steric hindrance effects, ensuring their

monodispersity in solution, and providing compatibility for subsequent device processing (such as inkjet printing). [5–7]

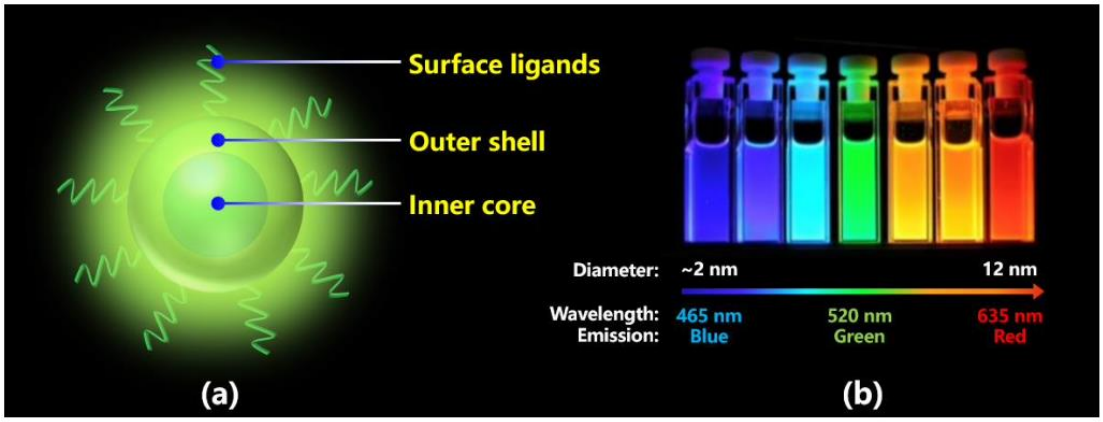

Figure 1.4 (a) Diagram of a single QD structure. (b) Photograph of some fluorescent QDs of varying sizes (provided by Fullnano Ltd.).

The unique optical and electronic properties of QDs, such as their wide absorption range, large absorption cross-section, and excellent charge transport properties, have led to their exploration in various optoelectronic applications, including photovoltaics, luminescent solar concentrators, and sensors with high sensitivity and low cost.[8–11] These same characteristics, along with their tunable emission and high photoluminescence quantum yield, also make QDs promising candidates for display technologies such as QLEDs.

The optical properties of QDs not only depend on the core material but are also significantly influenced by the band alignment of the core-shell structure. [12–17]

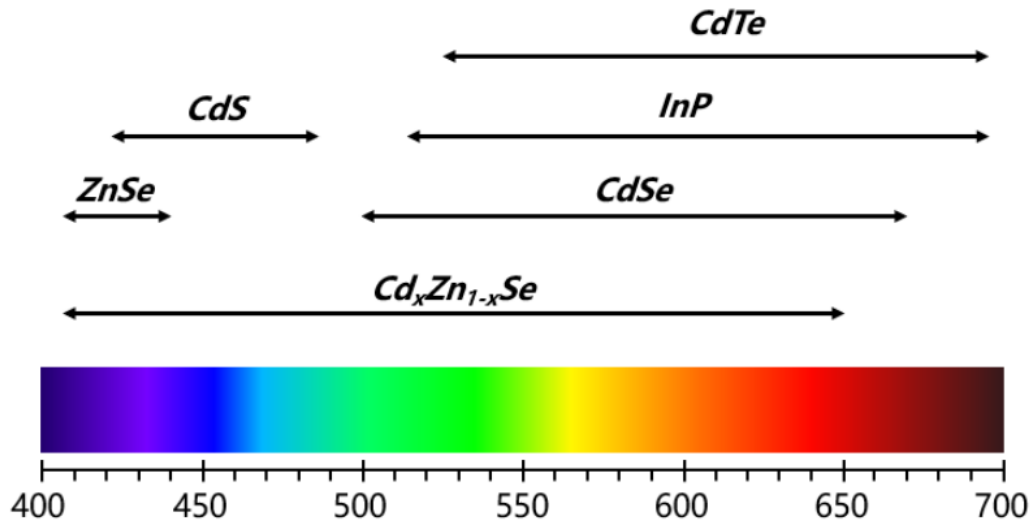

Figure 1.5 Emission wavelength range of QD cores composed of various semiconductor materials[18].

Based on the band matching relationship between the core and shell materials, QD heterojunctions can be classified into three types. [19]

Type I structure (such as CdSe/ZnS): In this configuration, the energy levels of the shell are arranged such that both electrons and holes are spatially confined within the central core region. This strong carrier confinement leads to high photoluminescence quantum yields (typically > 80%). However, due to the significant difference in lattice constants between the core and shell materials—for instance, a mismatch of approximately 12% between CdSe and ZnS—strain and interfacial defects can occur. To address this issue, a gradient or multi-shell architecture (such as CdSe/CdS/ZnS) is often employed to alleviate the lattice-induced stress and improve structural integrity.

Type II structure (such as CdSe/CdTe): The energy bands of the core and shell are staggered, leading to the localization of electrons in the core and holes in the shell, with

exciton recombination occurring at the interface. This structure can achieve a redshift in the emission wavelength (such as the emission of CdSe/CdTe QDs being red-shifted by about 50 nm compared to the CdSe core), but the separation of carriers reduces the radiative efficiency.

Quasi-Type II structure (such as CdSe/CdS): The conduction band offset is small (about 0.2 eV), with electrons partially delocalized to the shell while holes remain localized in the core. This partial carrier separation characteristic balances efficiency and wavelength tuning capability, making it suitable for optoelectronic devices requiring wide spectral tuning.

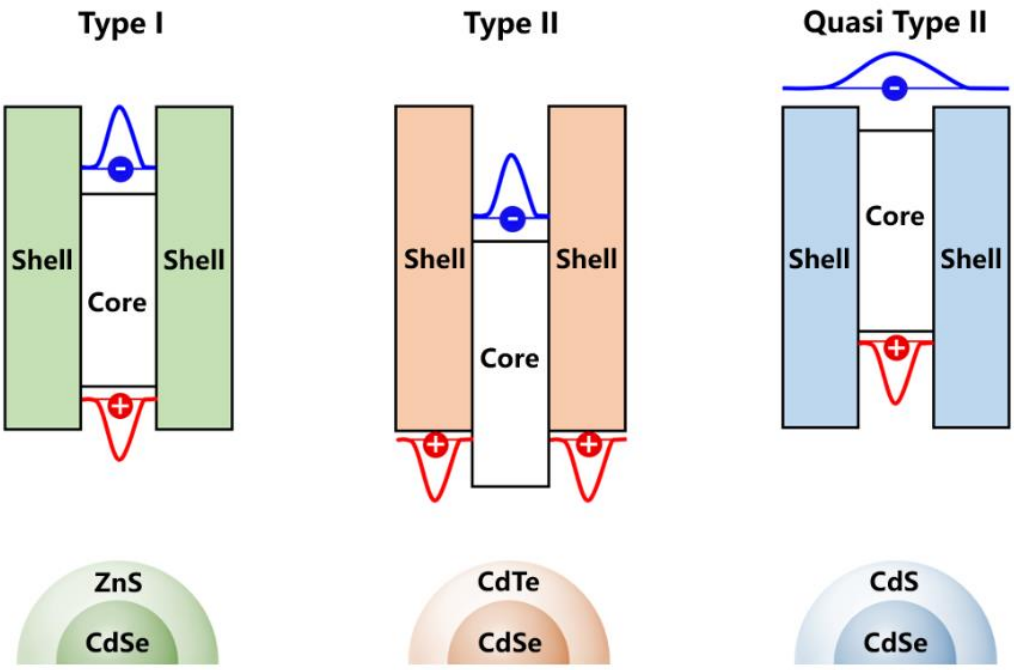

Figure 1.6 Energy level alignment of three heterostructures and typical core/shell QDs with a CdSe inner core.

In addition, the luminescent properties of QDs are also influenced by surface state density, ligand chemical environment, and external stimuli (such as temperature,

electric field). For example, unpassivated CdSe cores are prone to trap excitons due to surface dangling bonds, leading to a sharp decrease in PLQY; however, through shell encapsulation and ligand modification, surface defects can be significantly suppressed, enhancing device stability. Studies have shown that increasing the thickness of the ZnS shell to 3-5 monolayers can improve the photostability of CdSe/ZnS QDs by more than 10 times.

In summary, the structure and optical properties of QDs are closely related. By precisely controlling the core size, shell composition, and interface engineering, it is possible to achieve high efficiency, narrow FWHM (20–35 nm), and wide color gamut (>120% NTSC) luminescent performance, laying the foundation for their application in fields such as QLEDs.

1.2.2 Cadmium-free and lead-free environment-friendly QDs

Since the proposal of QDs by A. L. Efros, a Soviet scientist, and L. Brus, M. Bawendi, and other American scientists in the 1980s, various systems of QDs have become relatively complete after more than 30 years of development. For new display applications (visible light, narrow FWHM), mature research systems include the II-VI group, III-V group, and perovskite nanocrystal (NCs) materials. Taking the most representative II-VI QD material cadmium selenide (CdSe) as an example, when synthesizing CdSe QDs, zinc sulfide (ZnS), zinc selenide (ZnSe), cadmium sulfide (CdS) are usually introduced as shell layers to achieve core/shell or core/shell/shell structures. Inorganic semiconductor shells wrapping around the core can passivate

surface defects of the core and improve PLQY and stability of QDs. The outermost layer of organic ligands can further passivate surface defects of QDs to ensure uniform distribution in solution and thus improve the luminous efficiency and stability of QLEDs. By strictly controlling the morphology of QDs through these means, adjusting their size and chemical composition, and applying them to mature "sandwich" device structures with carrier injection and transport layers between the QD emissive layer (EML) and both electrodes, the external quantum efficiency (EQE) of QLEDs can reach over 20%[20–23]. Halide perovskite nanocrystals, such as $CsPbBr_3$ and $MAPbBr_3$, have experienced rapid development due to their narrow FWHM visible light emission, low cost, high color purity, and high PLQY. Additionally, the EQE of the device has also reached over 20%[24,25].

Significant progress has been made in QLED technology, but there are still limitations. With increasing attention being paid to environmental protection and human health, concerns have been raised over the use of certain QD materials that achieve excellent performance—such as high PLQY and elevated EQE in QLEDs—yet contain toxic heavy metals like cadmium (Cd) and lead (Pb). [26] In response to these concerns, the European Union amended the Restriction of Hazardous Substances (RoHS) directive in 2011, clearly restricting the incorporation of Cd and Pb in electronic devices.[27] As a further step, the European Commission enforced a regulation from October 2019 that prohibits the sale of cadmium-containing televisions and display panels within the EU market.[28] These elements are known to pose significant ecological risks and have been linked to serious health issues upon prolonged exposure.

Therefore, exploring cadmium-free, lead-free luminescent materials for QDs becomes an important consideration for the development of QLEDs.

Zinc selenide (ZnSe), its ternary tellurium alloy (ZnSeTe), and indium phosphide (InP) are commonly used cadmium-free and lead-free quantum dot materials, which excel at different emission wavelengths. Researchers usually adjust the synthesis method to obtain quantum dots of different sizes, corresponding to different wavelengths of luminescence, for display technology. They can achieve high photoluminescence quantum yield (PLQY) and narrow full width at half maximum (FWHM) while balancing environmental friendliness.

InP QD is very mature in obtaining vivid and narrow emission spectra in the green and red spectral regions[29], exhibiting nearly uniform PLQY and high color purity close to the Rec.2020 standard. And ZnSe QDs are introduced as a potential blue-emitting material, doped with tellurium to achieve ideal wavelengths and band difference reduction. The adjustment of Se/Te ratio effectively generated high emission and narrow emission blue and green ZnSeTe QDs.

1.3 Quantum dot light-emitting diodes (QLEDs)

1.3.1 Display applications

The application of QDs in display technology primarily relies on their unique photoluminescence (PL) and electroluminescence (EL) properties. These two types of luminescent mechanisms correspond to different device architectures and technical

routes, aiming to address the limitations of traditional display technologies while enhancing color performance and energy efficiency. [30]

Photoluminescent displays excite QDs to emit light using an external light source, with the core principle being to optimize display performance by utilizing the high color purity and narrow emission spectra of QDs. Currently, the mainstream technologies include Quantum Dot Enhancement Film (QDEF) and Quantum Dot Color Conversion (QDCC) approaches:

LCDs QDE technology QDEF technology involves embedding red and green QDs in a polymer film and integrating it with traditional liquid crystal displays (LCDs) to significantly enhance color performance (Figure 1.7). Specifically, when blue LED backlight passes through the QDEF, some of the blue light is absorbed by the QDs and converted into red and green light, while the remaining blue light is mixed with the converted light to form white light. This white light then passes through the liquid crystal layer and color filters to generate RGB pixels. Advantages: The narrow FWHM (20–35 nm) emission spectra of QDs can increase the color gamut from 72% NTSC in traditional LCDs to 110% NTSC. Compatible with existing LCD production processes, manufacturers such as Samsung and LG have achieved commercialization (e.g., QLED TVs), with a 30% reduction in power consumption compared to traditional LCDs. Limitations: Reliance on the backlight modulation of the liquid crystal layer leads to approximately 95% light loss (mainly from the polarizer and filter). Pixel-level light control is not achievable, resulting in a contrast ratio gap compared to OLEDs. [31]

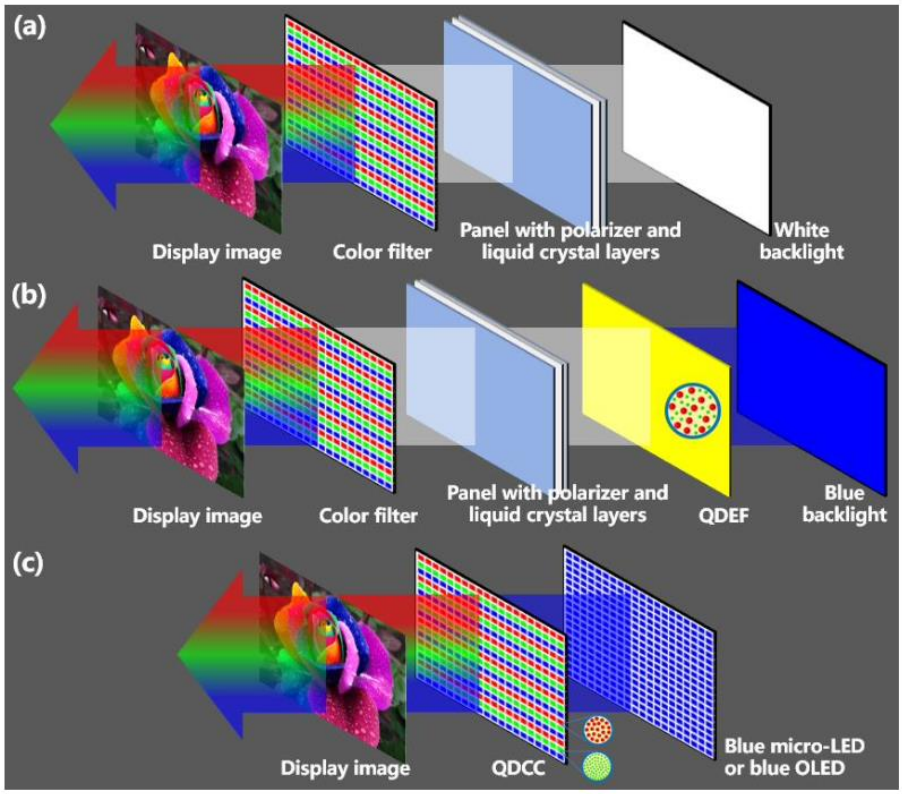

Figure 1.7 Diagrammatic representation of display structures: (a) a baseline LCD module, (b) a QDEF-assisted design utilizing quantum dot film for improved color rendering, and (c) a QDCC-based system employing direct color conversion by quantum dots.[30]

QDCC technology abandons traditional color filters and directly deposits QD pixels on blue micron-LED or OLED backlights. When the blue backlight is turned on, the QD pixels absorb blue light and emit specific colors (red, green), without the involvement of filters. Advantages: The structure is more simplified, and ultra-thin designs (reduced thickness by more than 50%) can be achieved after removing filters and liquid crystal layers. The self-luminescent nature supports pixel-level light control, with a contrast ratio approaching infinity (comparable to OLEDs), and further reduced power consumption. Stability of blue backlight are the challenges. Currently, the yield

of high-efficiency blue micron-LEDs is low, and brightness decay may occur during long-term operation. And patterned deposition of QD pixels: QDs need to be precisely deposited at high resolutions (such as 10 μm pixels for 4K displays), and existing inkjet printing technology is difficult to meet the requirements for uniformity and precision. About environmental stability: QDs exposed to high-brightness blue light may undergo photobleaching, requiring the development of more stable encapsulation processes[31].

Electroluminescence (EL) is a key feature of QLED displays, where QDs emit light directly when electrically excited, eliminating the need for a separate backlighting source. This direct conversion of electrical energy into light offers several advantages over traditional OLED technology. For instance, QLEDs can achieve up to 20% higher color saturation, providing more vivid and lifelike colors. Additionally, QLED displays are more energy-efficient, with power consumption as low as <1 W for a 6-inch panel, which is significantly lower than that of OLEDs.

While the performance of cadmium-free and lead-free QLEDs has improved over the past few years, especially through innovations in quantum dot synthesis and surface chemistry, there still remains a notable gap compared to Cd-based QLEDs. Many strategies have focused on optimizing the emitting materials themselves—for example, by refining the core–shell structure or conducting ligand exchange—but further enhancement of device-level performance is still essential.

In addition, optimizing the performance of the device is also very important. Current existing research including structural and interface engineering, as well as inspection of different device architectures, has identified key parameters responsible

for improving QLED performance. These efforts have improved the electroluminescence performance of QLED to a certain extent, but there is still room for further improvement. For example, many studies have achieved high EQE of over 10% or even 20% by improving the performance of quantum dot emitting materials through improved synthesis methods.

In addition to these technical advancements, the commercialization of QLED technology also requires overcoming economic and manufacturing challenges. The production of high-quality QDs and the development of cost-effective manufacturing processes are crucial for the widespread adoption of QLED displays. As these challenges are addressed, QLED technology has the potential to revolutionize the display industry, offering consumers brighter, more colorful, and energy-efficient displays for a wide range of applications, from smartphones and televisions to wearable devices and large-scale digital signage.[20,32–39]

1.3.2 Device architecture and operation

A standard QLED adopts a multilayered "sandwich" structure (Figure 1.8):

Anode: Indium tin oxide (ITO) provides transparency and hole injection.

Hole Transport Layer (HTL): Materials like poly(3,4-ethylenedioxythiophene):poly (styrenesulfonate) (PEDOT:PSS) or TFB ensure efficient hole mobility (10^{-4}–10^{-3} $cm^2/V \cdot s$) and energy alignment with the QD layer.

Emissive Layer (EML): A monolayer of QDs (e.g., CdSe/ZnS) with precise thickness control (20–30 nm) to maximize exciton recombination.

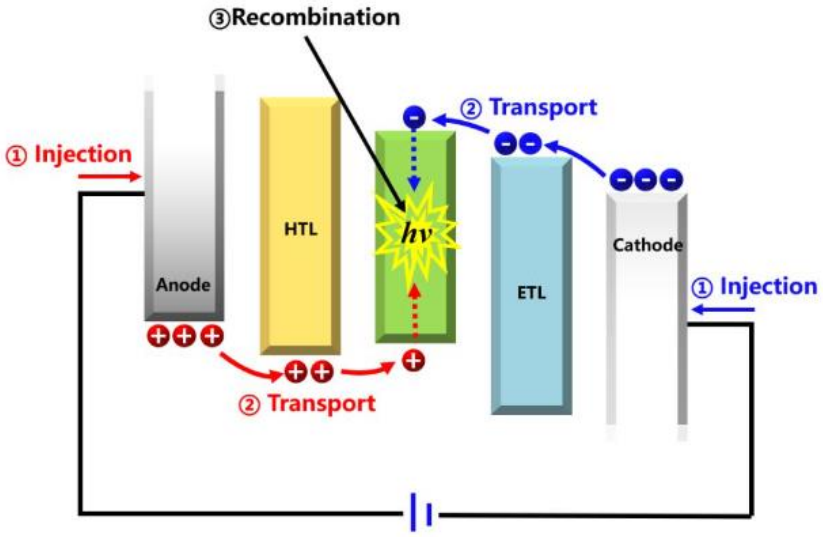

Figure 1.8 The fundamental structure and operating principle of QLEDs.

Electron Transport Layer (ETL): ZnO or TPBi facilitates electron injection, with ZnO's high mobility (0.01–0.1 $cm^2/V \cdot s$) favoring inverted device structures.

Cathode: Metals like Al or Ag complete the circuit.

Key challenges include interfacial energy barriers (e.g., ITO's work function ~4.7 eV vs. QDs' HOMO ~6.0 eV) and charge imbalance. Advanced designs employ interlayers like LiF or MoO_3 to lower injection barriers and hybrid HTL/ETL stacks to balance carrier fluxes.

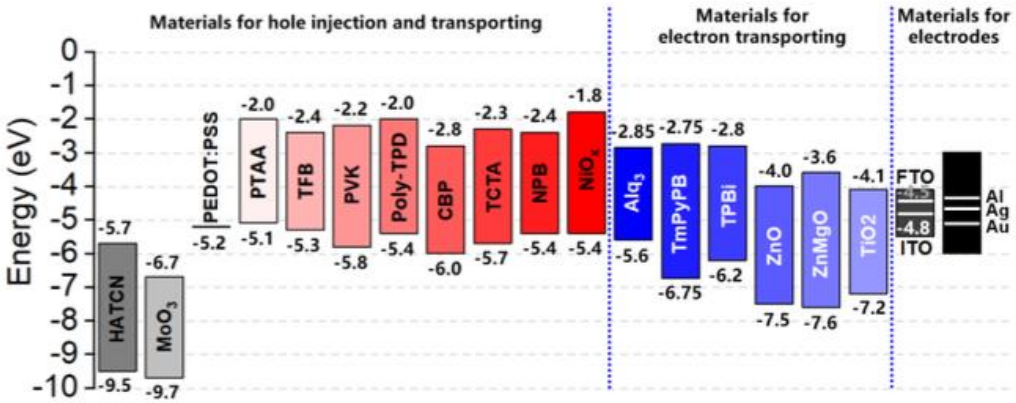

Figure 1.9 Energy level alignment of typical carrier transport layers (CTLs) and electrode materials employed in QLED architectures[40,41]

The configuration of QLED devices and the choice of carrier transport materials are primarily determined by factors such as charge carrier mobility, interfacial energy level alignment with QDs, and ease of fabrication. For instance, while PEDOT:PSS is frequently adopted as a hole transport layer due to its good conductivity and solution processability, its acidic nature can lead to device degradation over time. In contrast, employing inorganic materials like ZnO for the electron transport layer—owing to its high electron mobility—has been shown to significantly boost device efficiency and has facilitated the widespread use of inverted device structures.[42–44]

1.3.3 Challenges and innovations

One of the most important metrics used to evaluate device efficiency is the external quantum efficiency, or EQE. EQE represents the ratio of photons emitted externally to the number of charge carriers injected into the device. As such, it serves as a comprehensive indicator of how well light is extracted, how efficiently carriers are injected and transported, and how effectively excitons recombine.

Two major bottlenecks continue to limit EQE in Cadmium-free and Lead-free QLEDs. The first is low light extraction efficiency, or LEE. Although photons are efficiently generated within the QD layer, only a small portion is emitted by the device as visible light. This is due to total internal reflection and optical confinement inside

the high-refractive-index layers. Theoretically, less than 20% of internally generated light can be extracted without any optical structure. Specifically, waveguided modes account for ~37% of optical losses, substrate modes for ~20%, and coupling into surface plasmon polariton (SPP) modes causes further loss, particularly near metal contacts. These mods significantly constrain the EQE, regardless of the internal recombination efficiency.

The second bottleneck is the poor behavior of charge carriers. In QLED, electroluminescence relies on the recombination of electrons and holes within the quantum dot EML. However, if the energy levels on the interface are not aligned, or if one carrier is injected or transported more efficiently than others, an injection imbalance will occur, further affecting injection efficiency. In addition, non-radiative recombination and other behaviors may also jointly affect internal quantum efficiency (IQE).

In cadmium-free and lead-free QLEDs, carrier injection imbalance is most often due to a large hole injection barrier and low hole mobility in the HTL. As a result, excess electrons accumulate in the EML without sufficient holes to recombine with, leading to increased non-radiative recombination, Auger effects, and spatial shift of the recombination zone away from the optimal location. These effects reduce the IQE and indirectly limit EQE.

EQE directly decides on these three factors， LEE, carrier injection efficiency, and IQE. So, it is necessary to improve one or all of them together for enhancing the overall device efficiency.

1.3.4 Development of cadmium-free and lead-free environment-friendly QLEDs

Through the optimization of light-emitting materials, device structure and in-depth understanding of working mechanism, InP based QLEDs of red light and green light continue to develop, with EQE exceeding 21.4% and 13.6% respectively, and there are few reports of blue light InP QLEDs (As example below). In 2017, You and Deng applied the synthesized high-performance blue InP / ZnS QDs with small core and thick shell to the device, adopted the device structure of ITO / ZnMgO / QDs / CBP / MoO_3 / Al, and obtained the El peak at 488 nm, with FWHM of 45 nm (as shown in Figure 1.10)[45]. At a bias voltage of 10 V, a maximum brightness of 90 cd / m^2 was obtained.

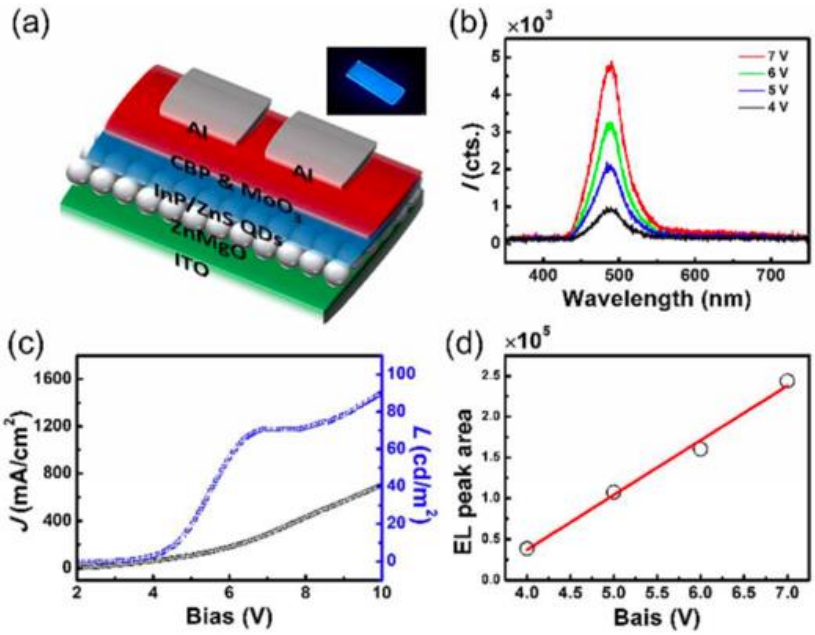

Figure 1.10 (a) Schematic of InP/ZnS QLED, and inset picture in (a) shows a blue emissive QLED device. (b) EL spectra of the blue LED under different bias voltage. (c) J-V-L curve of the QLED device. (d) A plot of EL peak area versus bias[45]

In 2020, Shen and Du et al. Synthesized InP/gap/ZnS//ZnS multi shell blue QDs[46]. The gap interlayer minimizes lattice mismatch and interface defects. The thicker ZnS shell increases the stability of QDs, inhibits the fluorescence resonance energy transfer between tightly packed QDs, and helps to improve the performance of blue light devices. They applied this QD to the QLED device with ITO / PEDOT: PSS / TFB / QDs / ZnO / Al structure, detected the EL peak at 488 nm and FWHM at 50 nm, obtained 0.40% EQE and 3120 cd/m^2 brightness, and made a breakthrough in blue InP QLEDs. They theoretically studied the change of density of states with shell thickness to explore the driving mechanism of the excellent performance of thick shell QLEDs. After further optimizing the shell thickness, EQE can be increased to 1.01% (as shown in Figure 1.11-1.12).

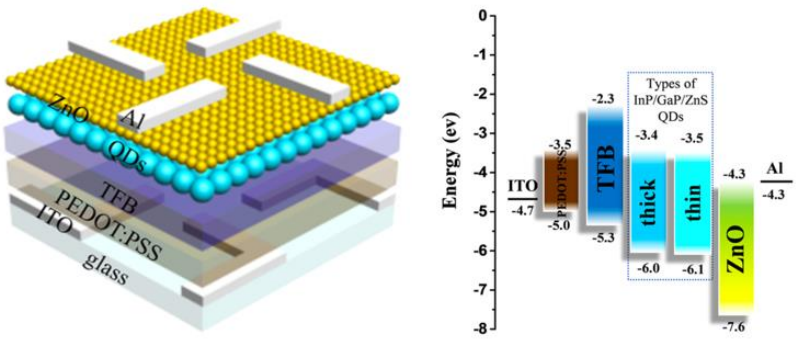

Figure 1.11 Schematic diagram of the InP/GaP/ZnS//ZnS QLED structure and energy level illustration of the QLED[46]

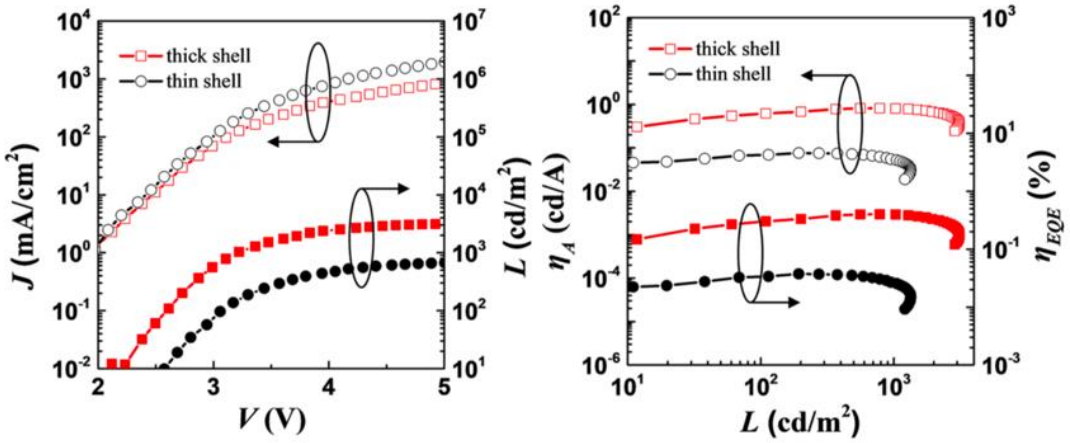

Figure 1.12 Left: Variations of current density and luminance as a function of the voltage. Right: Current efficiency and EQE as a function of the luminance. Two QLEDs based on InP/GaP/ZnS QDs with thin and thick ZnS shells are considered[46]

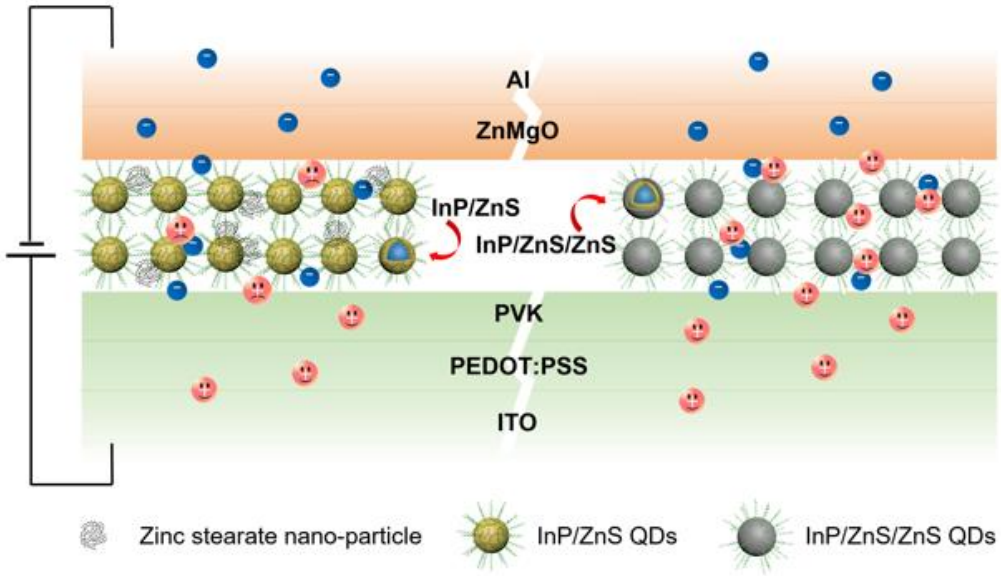

Figure 1.13 Schematic illustration for the comparison of InP/ZnS QLED and InP/ZnS/ZnS QLED carrier injection efficiency[47]

Wang and Sun found that the remaining zinc stearate after QD purification would hinder carrier injection in QLEDs devices. In order to solve this problem, increase the

shell thickness of InP QDs and reduce the energy transfer between QDs, they added s-top and Zn $(OA)_2$ to continue to coat the ZnS shell. Excess s-top will react and remove the remaining zinc stearate. After the reaction, the shell thickness increased by 2 nm, and the thick shell InP / ZnS / ZnS QDs were more stable than the thin shell InP / ZnS QDs. The hole injection of corresponding QLED devices (ITO) / PEDOT: PSS / poly(9-vinylcarbazole) (PVK) / QDs / $Zn_xMg_{1-x}O$ NPs / Al structure) has been significantly improved, and the maximum current efficiency, brightness and on voltage have been significantly improved. The EQE has increased from 0.6% of InP / ZnS qled to 1.7% of InP / ZnS / ZnS QLED (as shown in Figure 1.13) [47].

Kim et al. Selected the synthesized ternary InGaP / ZnSeS / ZnS blue QDs with 465 nm luminescence peak and 80% PLQY to prepare QLEDs devices. They obtained 469 nm El spectrum, 1038 cd/ m^2 brightness and 2.5% EQE, which is the best InP based blue QLEDs device at present (as shown in Figure 1.14)[48].

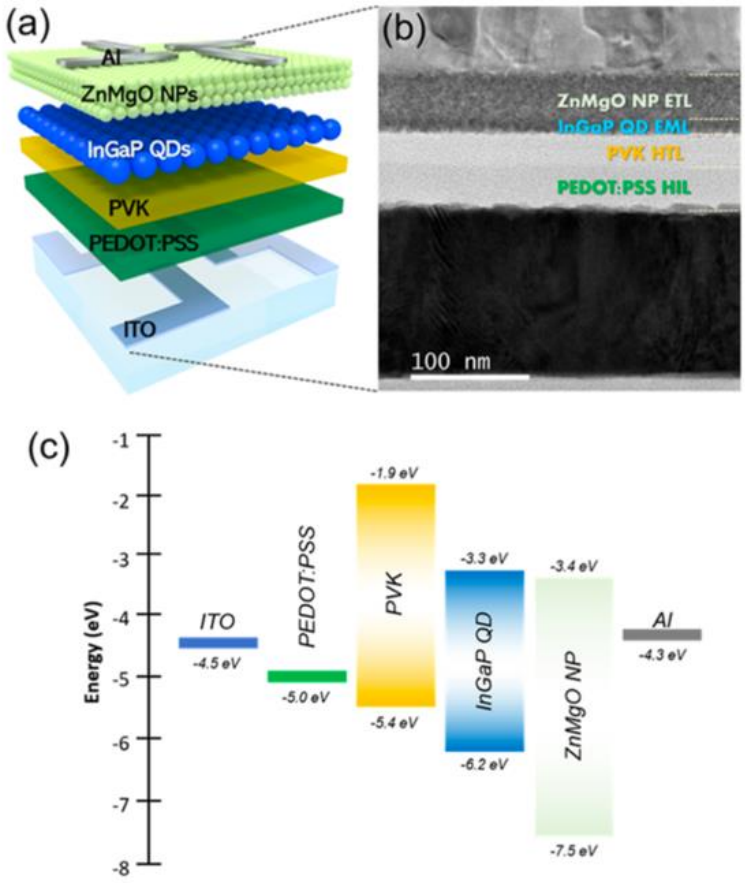

Figure 1.14 (a) InGaP/ZnSeS/ZnS QLED device architecture, (b) cross-sectional TEM image, and (c) energy band diagram of a multilayered blue-emissive InGaP QLED[48]

There are two main reasons for the low efficiency of blue light InP QLEDs. On the one hand, the surface defects of blue InP QDs are relatively more, and its PLQY is lower; On the other hand, the hole barrier from the highest occupied molecular orbital (HOMO) of the HTL to the top of the valence band of blue light QDs is large, carrier injection is difficult, and the transmission efficiency is low. It needs to be further improved by improving material properties and device structure optimization.

Table 1.1 Some advances of blue InP QDs and QLEDs

Year	QDs	PL peak (nm)	PLQY (%)	FWHM (nm)	QLEDs EQE (%)
2008	InP/ZnS	480	60	90	/
2012	InP/ZnS	475	5	39	/
2017	InP/ZnS	477	76.1	43.7	/
2019	InP/ZnS	425	25	72	/
2020	InP/GaP/ZnS// ZnS	488 (EL)	81	45	1.01
2020	InP/ZnS/ ZnS	468	45	47	1.7
2020	InGaP/ZnSeS/ ZnS	475- 465	80-82	45-47	2.5

In addition, the development of green light InP devices in recent years is summarized as follows.

Table 1.2 Recent advances of green InP QLEDs

Year	QDs	EL peak (nm)	Max luminance (cd m^{-2})	EQE (%)	Reference
2019	InP/GaP/ZnS	530	2938	6.3	Adv. Opt. Mater. 2019, 7, 1801602.
2019	InP/ZnMnS/ZnS	517	420	2.7	ACS Omega 2019, 4, 18961.
2020	InP/ZnSeS	545	1593	0.904	Adv. Opt. Mater. 2020, 8, 1901362.
2021	InP/ZnSeS/ZnS	525	1836	7	Adv. Funct. Mater. 2021, 31, 2008453.
2021	InP/ZnSe/ZnS	540	/	16.3	Commun. Mater. 2021, 2, 96.
2022	InP/ZnSe/ZnS	534	13445	9.3	ACS Energy Lett. 2022, 7, 2247.

2022	InP/ZnSe/ZnS	535	4955	7.8	J. Mater. Chem. C 2022, 10, 8192.
2023	InP/ZnSe/ZnS	535	18356	8.46	Nanoscale 2023, 15, 2837.

Before 2012, although there were some studies on the photoluminescence of ZnSe nanocrystals, there were no reports on blue/ultraviolet-emitting ZnSe/ZnS QLEDs. Xiang et al. first reported blue-violet QLEDs using ZnSe/ZnS core-shell QD solution treatment[49]. They used QDs with a PL emission peak at 420 nm, a PLQY of 40%, and an FWHM of 16 nm to prepare QLEDs. By adjusting the thickness of the HTL and the QD EML, they further improved the charge balance within the device, ultimately achieving an EQE of 0.65%, opening the door to research on ZnSe/ZnS blue-violet QLEDs.

In 2013, Ji et al. used an inverted device structure to prepare deep blue-emitting ZnSe/ZnS core/shell QD LEDs[50]. The QLED device had a turn-on voltage of 4.0 V, an FWHM of 15 nm, and a high-color-purity deep blue emission peak at 441 nm. Its maximum brightness and current efficiency reached 1170 cd/m^2 and 0.51 cd/A, respectively.

In 2015, Shen et al. applied high-performance (PLQY above 48%) ZnSe/ZnS core/shell QDs synthesized by the “low-temperature injection and high-temperature growth” method to blue-violet (PL peak ~425.6 nm) QLEDs, achieving an EL spectral FWHM of 21.6 nm, a brightness of 2632 cd/m^2, and an EQE of 7.83%.[51] In terms of device structure, the HTL chose PVK with a lower HOMO energy level (-5.8 eV)

instead of TFB (-5.3 eV); the ETL used ZnO, which also acted as a hole-blocking layer, better achieving energy level matching and carrier injection balance in the device.

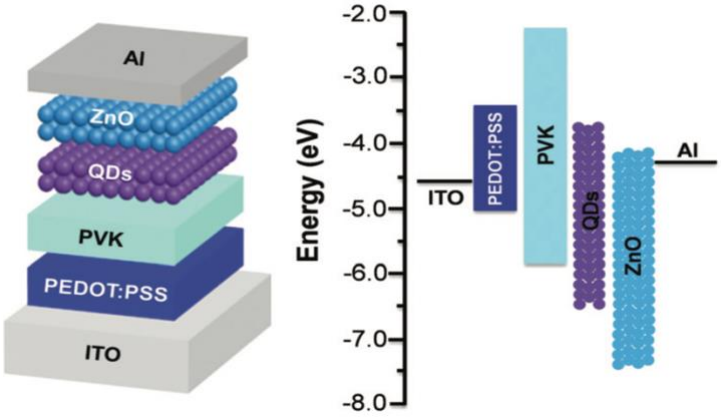

Figure 1.15 Schematic of a layered ZnSe/ZnS QLED device and the energy level diagram for the various layers[51]

With the development of ternary alloy ZnSeTe materials, blue light ZnSe QLEDs have also encountered new opportunities. In 2019, Jang et al. prepared blue light QLEDs using synthesized bilayer shell structure ZnSeTe/ZnSe/ZnS blue light QDs. They used a full solution process and a device structure of ITO / PEDOT:PSS / PVK / QDs / ZnMgO / Al. The relatively thick bilayer shell and the presence of the ZnSe inner shell effectively suppressed non-radiative processes such as Förster Resonance Energy Transfer (FRET) and Auger recombination, which were key factors in improving device efficiency. The double-shell QDs emitted blue light at 441 nm, with a high PLQY of 70% and a narrow FWHM of 32 nm. This QLED was also the first light-emitting diode device based on ternary ZnSeTe QDs, with a peak brightness of 1195 cd/m^2, a current efficiency of 2.4 cd/A, and an EQE of 4.2%, representing a breakthrough in cadmium-free blue light QLEDs at the time. However, due to the wide

bandgap of the material, hole injection was difficult, resulting in a relatively high turn-on voltage for ZnSeTe blue light QLEDs. Similarly, in 2020, Park et al. synthesized $ZnSe_{1-x}Te_x$/ZnSe/ZnS deep blue light QDs and applied them to a device with the structure of ITO / PEDOT:PSS / PVK / QDs / TmPyPB / LiF / Al to verify the electroluminescent characteristics. The QLEDs device was also affected by hole injection, resulting in a relatively high turn-on voltage of 5.13 V. The obtained maximum brightness was 3200 cd/m^2, the maximum current efficiency was 2.73 cd/A, and the maximum EQE was 4.06%. The electroluminescent chromaticity coordinates (0.151, 0.056) met the requirements of high-definition television, but for practical applications, the working life is also a key issue that requires more research.[52,53]

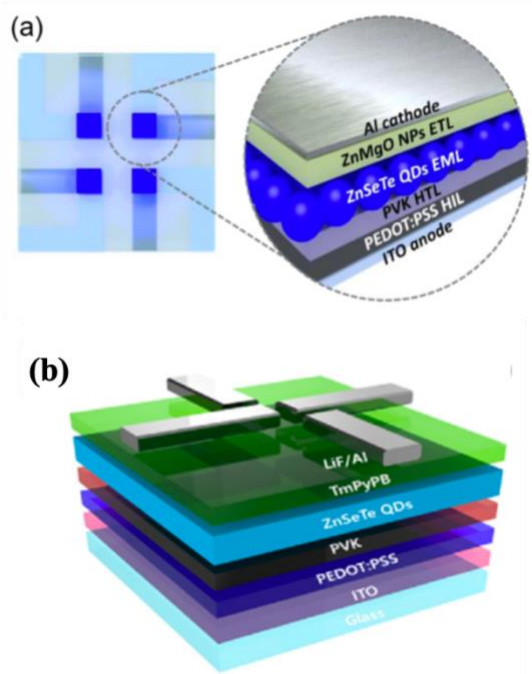

Figure 1.16 (a) ZnSeTe/ZnSe/ZnS QLED schematics (b) $ZnSe_{1-x}Te_x$/ZnSe/ZnS QLED Device structure.[52,53]

In October 2020, Kim et al. found that $ZnCl_2$ introduced during the QD synthesis process can passivate surface defects more effectively than the original ligand OA. To simultaneously improve charge injection, transport, and recombination, they constructed a dual EML with a gradient Cl^- content in the QLED. They used $ZnCl_2$ to perform a cleaning process on the original EML, achieving a greater degree of ligand exchange, removing residual OA, and preparing an EML with a smaller OA content to improve hole injection. After the cleaning process, the film's PL characteristics remained unchanged. The prepared dual EML QLED device increased the current density by about 200 times and reduced the turn-on voltage to 2.6V. The optimized EQE and brightness were significantly enhanced, reaching 20.2% and 88900 cd/m^2, respectively. The T_{50} extrapolated lifetime at 100 cd/m^2 brightness (acceleration factor 1.9) was 15850 hours, making it the best-performing blue light QLED reported to date.[54]

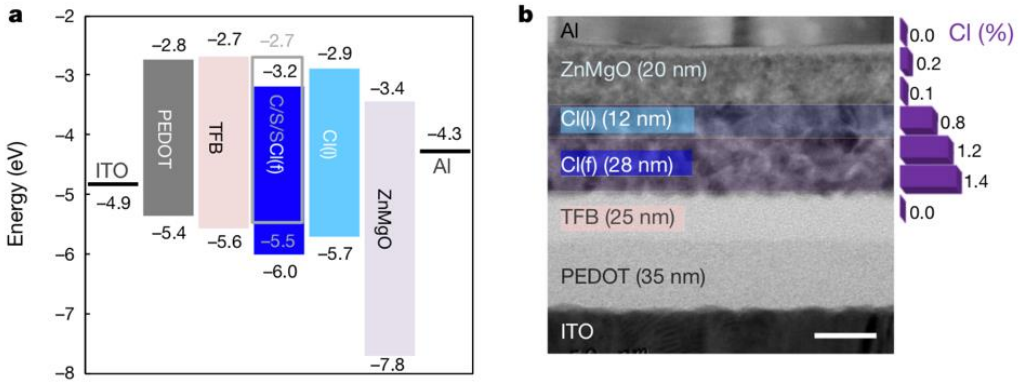

Figure 1.17 (a) Energy-band diagram of the QLEDs. (b) Cross-sectional TEM image (scale bar, 30 nm) of the QLED with double EML.[54]

Table 1.3 Recent advances of ZnSe (ZnSeTe) QLEDs

Year	QDs	EL peak (nm)	Max luminance (cd m^{-2})	EQE (%)	Ref.
2019	ZnSeTe/ZnSe/ZnS	445	359	4.2	ACS Appl. Mat. Interfaces 2019, 11, 46062.
2020	ZnSeTe/ZnSe/ZnS	/	88900	20.2	E. Jang, Nature 2020, 586, 385.
2020	ZnSeTe/ZnSe/ZnSeS/ ZnS	447	2904	9.5	ACS Energy Lett. 2020, 5, 1568.
2020	ZnSeTe/ZnSe/ZnS	450	3200	4.06	J Ind Eng Chem 2020, 88, 348.
2022	ZnSeTe/ZnSe/ZnS	455	4366	18.6	Chem. Eng. J. 2022, 429, 132464.
2023	ZnSeTe/ZnSe/ZnS	445	332	5.46	Adv. Mate. Interfaces 2023, 10, 2202241.
2023	ZnSe:xTe/ZnSe/ZnS	458	/	5.7	J. Phys. Chem. Lett. 2023, 14, 2526.
2023	ZnSeTe	460	/	18.16	Nano Res. 2023, 16, 5517.
2024	ZnSeTe/ZnSe/ZnS	463	13677	17.2	Chemical Engineering Journal 489 (2024): 151347.
2024	ZnSeTe/ZnSe/ZnS	446	710	2.25	ACS Applied Nano Materials 7.11 (2024): 13166-13172.
2025	ZnSeTeS/ZnSe/ZnS	460	36850	24.7	Nature (2025): 1-6.

1.4 Potential contributions

In Summary, the demand for higher resolution, lower power consumption, and environmentally friendly displays continues to grow globally.

However, current cadmium-free and lead-free QLEDs still fall short in terms of efficiency and commercial viability, the overall device performance is hindered by two fundamental limitations: low light extraction and poor carrier behavior.

These challenges directly impact the key components of EQE: LEE and carrier behavior, which are related to IQE and injection efficiency. The three parts of my work and the strategies I propose also correspond to them. To achieve high EQE, both IQE and LEE must be simultaneously optimized.

Therefore, the motivation for this work is to rooted in bridging the gap between material advances and device-level performance. While previous efforts have greatly improved QD synthesis and surface engineering, fewer studies have systematically addressed how device architecture and interfacial physics can further enhance EQE.

This thesis introduces three strategies:

Enhancing light extraction through the use optical tunneling structures in low-SPP devices that redirect trapped photons into outcoupled modes.

Improving hole injection by incorporating a molecular electric dipole layer at the HTL/EML interface to mitigate energy barriers and promote charge balance.

Suppressing electron leakage by tuning interfacial band alignments and preventing unwanted carrier overflow that leads to non-radiative loss.

This thesis explores cadmium-free and lead-free QLEDs with a focus on light extraction and carrier behavior. Based on an analysis of the working mechanisms, optimization strategies are proposed from both optical and electrical perspectives to achieve improved light extraction and carrier balance. The optimized cadmium-free and lead-free QLEDs exhibit higher EQE, making them more suitable for display applications. The mechanisms and solutions proposed in this thesis are expected to provide valuable insights for further advancements in the field.

1.5 Organization of the thesis

The thesis is divided into six chapters.

Chapter 1 introduces the research background, literature review, and research goals.

Chapter 2 presents the simulation principles, experimental techniques, and characterization methods.

In Chapter 3, the light extraction is investigated in QLEDs, analyzing the transmission of light in various modes within the device and devising a comprehensive strategy to enhance device efficiency. The experimental results further confirmed the effectiveness of the design by validating the simulation results.

Chapter 4 presents the development of efficient cadmium-free and lead-free QLEDs based on 2,2'-(perfluoronaphthalene-2,6-diylidene)dimalononitrile (F6-TCNNQ) through interface engineering. A dipole layer was designed at the HTL/EML interface to enhance hole injection, reduce energy barriers, and achieve improved carrier balance.

Chapter 5 investigates the issue of electron leakage from green InP/ZnS QDs by conducting comparative experiments on PL performance and observing electron leakage phenomenon. Additionally, a simulation was performed to understand the mechanism of electron leakage, which led to the proposal of introducing a LiF layer to modify the ITO anode as a potential strategy.

In Chapter 6, we summarized the key findings and suggested possible directions for future studies.

Chapter 2 Simulation and experimental methodology

Firstly, cadmium-free and lead-free QLEDs were analyzed through theoretical knowledge, and then simulation experiments were used to gain a deeper understanding of the device and provide a basic design for optimization strategies. Especially in determining the relevant process parameters. Finally, I will manufacture actual devices and conduct optoelectronic performance tests to verify the effectiveness of the strategy and the actual improvement effect of EQE.

Theoretical analysis combines optical physics, semiconductor physics, and materials science. By understanding the interaction between quantum dots and device materials, I can model key processes like carrier dynamics and light extraction. This helps identify the fundamental challenges in improving LEE and balancing carrier injection.

For simulations, I mainly used Setfos, a software tool for optical and electronic modeling for QLEDs. The software can provide a basic design for optimization strategies. Based on the drift diffusion model, simulate charge transfer and carrier recombination within QLEDs. In addition, device structures are designed with optical modes analysis to enhance light extraction.

In the design and simulation experiments, I also incorporate thin-film testing within the device to make the optimization strategy more effective.

After determining the optimization strategy through simulation experiments, I will fabricate the actual device and perform optoelectronic performance testing to verify the effectiveness of the strategy and the improvement effect of EQE. I also conduct multiple rounds of experiments to optimize the actual process.

The detailed experimental methods used or guided are as follows.

2.1 Multiscale simulation and theoretical analysis

The design and optimization of QLED devices require a comprehensive consideration of various physical phenomena, including optics, electronics, thermodynamics, and more. Computational simulations and theoretical analyses provide important tools for understanding device operation principles, predicting device performance, and guiding device design. The optical extraction and carrier behavior studied in this paper primarily involve optical and electrical physical phenomena. The main computational simulation methods used are multi-scale simulations for optical mode optimization and multi-physics field modeling for carrier dynamics.

2.1.1 Optical mode optimization and multi-scale simulation

The light extraction efficiency of QLED devices is one of the key factors affecting device performance. To improve light extraction efficiency, it is necessary to optimize the optical modes of the device. Multi-scale simulation methods can effectively analyze the interactions between photons, excitons, and carriers within the device, and study the relationship between microcavity effects and light extraction efficiency.

COMSOL Multiphysics is a multi-physics simulation software that can be used to simulate physical phenomena such as electromagnetic fields, fluids, structures, and chemistry. By coupling electromagnetic field (Maxwell's equations) with carrier transport models, COMSOL can simulate the interactions between photons, excitons, and carriers in QLEDs, and analyze the impact of microcavity effects on light extraction efficiency. For example, it can study the influence of QD layer thickness, QD spacing, dielectric layer refractive index, and other factors on light extraction efficiency.

In COMSOL Multiphysics, optical mode optimization is performed. First, a device structure model needs to be established, defining material parameters, boundary conditions, etc. Then, appropriate physical field interfaces are selected, such as electromagnetic field interfaces, carrier transport interfaces, etc. Next, a solver is set up, such as a steady-state solver, a transient solver, etc. After running the solver, the optical characteristics of the device can be calculated, such as light field distribution, light extraction efficiency, etc. Finally, post-processing is performed to analyze the simulation results and optimize the device structure parameters.[55,56]

The finite-difference time-domain (FDTD) method numerically solves Maxwell's equations in three-dimensional space, enabling precise modeling of light propagation, scattering, and resonance effects in QLEDs. By discretizing the device structure into a spatial grid, this approach captures the interaction between light and nanostructured QD layers, particularly for optimizing microcavity effects and photon extraction efficiency. Material dispersion models are incorporated to account for wavelength-dependent refractive indices, ensuring accurate predictions of optical modes across visible to near-infrared spectra.

Additionally, machine learning techniques can be used to accelerate the optimization process of device structure parameters. For example, genetic algorithms or Bayesian optimization methods can be employed, based on initial data from Setfos and FDTD, to automatically screen for the optimal device structure parameters, such as layer thickness, refractive index gradients, etc. This approach can significantly shorten the design cycle and improve device performance.

In machine learning-assisted optimization, it is first necessary to collect simulation data from Setfos and FDTD, including device structure parameters and light extraction efficiency, etc. Then, appropriate machine learning models are selected, such as genetic algorithms, Bayesian optimization, etc. After training the machine learning model with simulation data, the trained model can be used to automatically screen for the optimal device structure parameters. Finally, the optimization results are validated using new simulation data, and adjustments are made as needed.

2.1.2 Multi-physics field modeling of carrier dynamics

The carrier dynamics of QLED devices are important factors affecting device efficiency and stability. Through multi-physics field modeling, the behavior of carriers in the device can be studied, and factors influencing carrier dynamics can be analyzed.

Setfos Software is a specialized tool for simulating semiconductor devices, capable of modeling carrier dynamics, optical properties, thermal characteristics, and more. Setfos' greatest advantage lies in its extensive library of physical models and user-friendly interface, making it convenient for users to perform device simulations and analyses.

The development history of Setfos dates back to 1998, when it was developed by the Fraunhofer Institute for Silicon Technology (ISiT) in Germany. Over time, Setfos has been continuously updated and improved, with the addition of many new features and models, including optical models, thermal models, new material models, and user interface enhancements. In this paper, the focus is on the optical models. Initially, Setfos primarily concentrated on carrier dynamics simulations, but it gradually incorporated optical models, such as ray-tracing-based models and FDTD models, for analyzing device optical properties.[57]

The Drift-diffusion-Poisson model in Setfos can simulate carrier transport processes in devices, including drift, diffusion, and recombination. This model considers the electric field effect, concentration gradient effect, and recombination

effect of carriers, accurately simulating the carrier dynamics characteristics of devices. Setfos can also simulate optical properties of devices, such as light absorption, emission, and extraction. It offers various optical models, including ray-tracing-based models and FDTD models, for analyzing device optical properties. Additionally, Setfos can simulate thermal properties of devices, such as heat conduction and radiation. It provides various thermal models for analyzing device thermal properties and studying thermal stability. Setfos can also be coupled with other simulation software, such as COMSOL Multiphysics and FDTD Solutions, enabling multi-physics coupled simulations for a more comprehensive analysis of device performance.

The process for simulating carrier dynamics in Setfos is as follows: First, a device structure model needs to be established, defining material parameters, boundary conditions, etc. Then, appropriate physical field interfaces are selected, such as drift-diffusion-Poisson interfaces, optical interfaces, and thermal interfaces. Next, a solver is set up, such as a steady-state solver or a transient solver. After running the solver, the carrier dynamics characteristics, optical properties, and thermal properties of the device can be calculated. Finally, post-processing is performed to analyze simulation results, such as carrier concentration distribution, current density distribution, light field distribution, and temperature distribution.

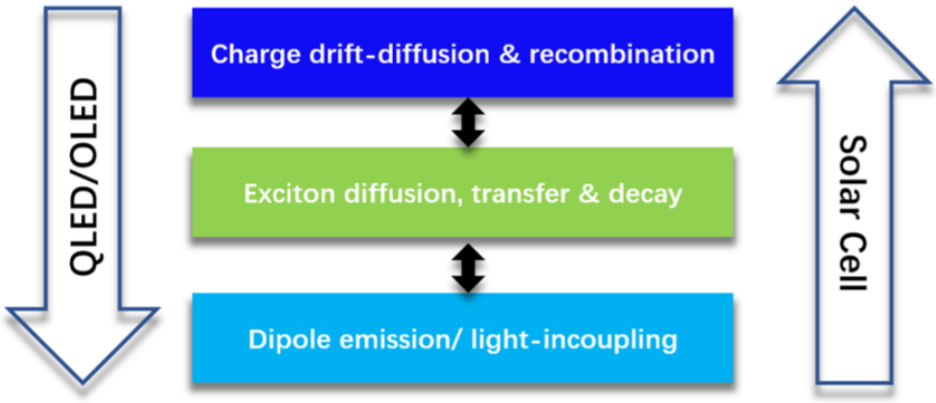

Figure 2.1 Workflow simulation for QLED/OLED or other devices using Setfos.

The Monte Carlo particle tracking method can be used to simulate the scattering paths of carriers within the QD layer. Combined with the distribution of defect states, the Monte Carlo method can predict the proportion of non-radiative recombination and analyze the impact of defect states on device performance. For example, it can study the influence of QD size, shape, surface roughness, and other factors on carrier dynamics.[58]

In Monte Carlo simulations, a QD layer structure model must first be established, defining the size, shape, surface roughness, and other parameters of the QDs. Then, the density and energy levels of defect states are defined. Next, the scattering paths of carriers within the QD layer are simulated, including elastic scattering and inelastic scattering. Finally, the probability of non-radiative recombination between carriers and defect states is calculated, and the characteristics of carrier dynamics, such as carrier concentration distribution and non-radiative recombination ratio, are analyzed.

Computational simulations and theoretical analyses are important tools for the research and development of QLED devices. Through multi-scale simulations for optical mode optimization and multi-physics field modeling for carrier dynamics, it is possible to effectively understand the operating principles of devices, predict device performance, and guide device design, thereby enhancing the performance and stability of QLEDs.

2.2 Materials and interface characterization techniques

2.2.1 Structural and morphological analysis

The structure and morphology of each functional layer are crucial to their performance in QLED devices. To gain a deep understanding of the properties of these films, structural and morphological analyses are necessary. Besides atomic force microscopy (AFM) and transmission electron microscopy (TEM), Scanning Electron Microscopy (SEM) is more commonly used in this thesis.

SEM is a surface morphology analysis technique used to observe the surface morphology and cross-sectional structure of QD films and devices. The imaging principle of SEM involves scanning the sample surface with a focused electron beam. As electrons interact with atoms in the sample, secondary electrons (SE) and backscattered electrons (BSE) are produced. SE images can be used to observe the

surface morphology of the sample, such as the size, shape, and surface roughness of particles. BSE images can be used to observe the composition of the sample, such as the interfaces between different materials and defects within the material.

The resolution of SEM can reach the nanometer level, allowing for the observation of fine structures on the sample surface. SEM can also be used for elemental analysis, such as analyzing the elemental composition and distribution within the sample. In my work, the main SEM instrument used is the Zeiss GeminiSEM 300, which has basic parameters including high resolution (up to 1.0 nanometers), an acceleration voltage range of 30 kV to 3 kV, and a high-sensitivity electron beam detector, providing excellent surface morphology and compositional analysis capabilities.[59,60]

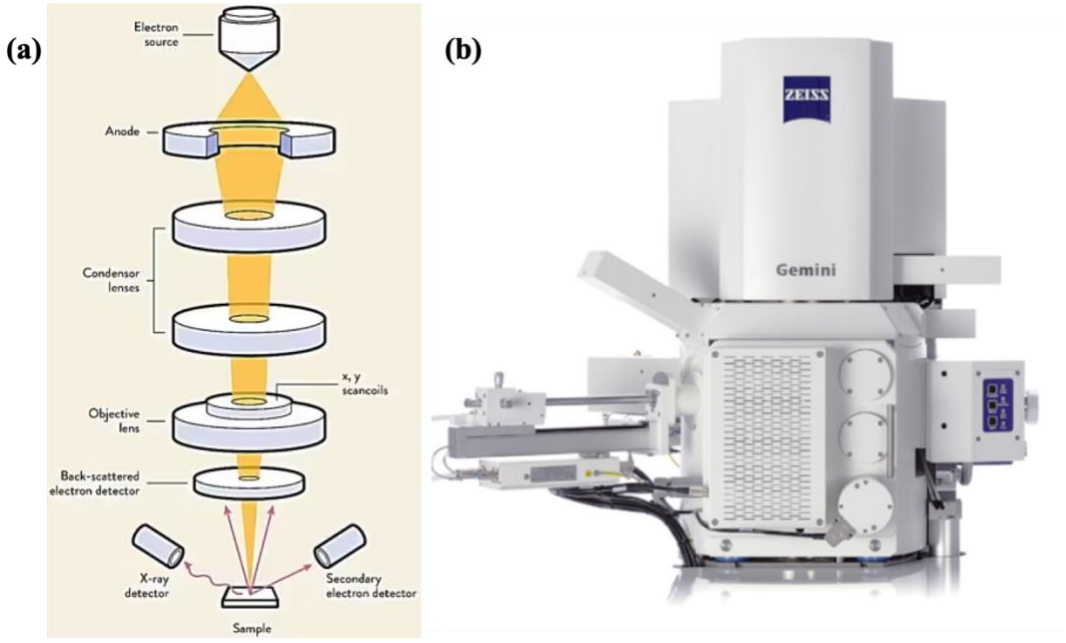

Figure 2.2 (a) The working principle diagram and (b) equipment diagram of SEM.

2.2.2 Optical and electronic property characterization

In the research and optimization of QLED devices, accurate characterization of the optical and electronic properties of QD films is crucial. To deeply understand the photoelectric conversion mechanism of the devices and improve their performance, we have adopted various characterization techniques, including UV-VIS-NIR spectroscopy, PLQY measurement, and ultraviolet photoelectron spectroscopy (UPS) analysis.

UV-VIS-NIR spectroscopy is a non-destructive analytical method that provides detailed information about the band gap and optical density of QD films by measuring their absorption and transmission spectra. These data are essential for evaluating the luminescent properties of QD materials and their potential applications in QLED devices. Additionally, this technique is used to assess the transparency of electrode materials (such as ITO) and the efficiency of light output structures. Specifically, by analyzing the light absorption in certain wavelength ranges, we can infer the band structure of the QD films, which guides the design and optimization of the device structure.[61,62]

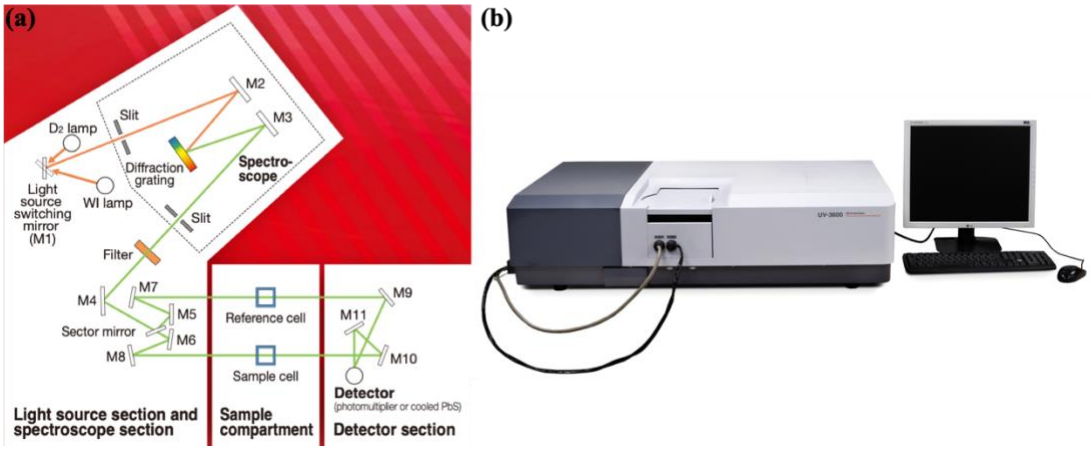

Figure 2.3 (a) The working principle diagram and (b) equipment diagram of UV-VIS-NIR spectroscopy.

The fluorescence test system is built by the laboratory, which is composed of laser, spectrometer, integrating sphere and optical fiber. The light emitted by the laser enters the integrating sphere through the optical fiber. After multiple diffuse reflections, the interior of the integrating sphere is evenly irradiated on the sample. The fluorescence emitted by the sample is detected by the spectrometer through the optical fiber after multiple diffuse reflections, so as to obtain the fluorescence spectrum.

The measurement of photoluminescence quantum yield (PLQY) quantifies the radiative recombination efficiency of QD materials. PLQY is determined by comparing the number of emitted photons to the number of absorbed photons, and this metric is decisive for evaluating the quality of QD materials and their potential application value in high-efficiency QLEDs. During the experiments, we used a precise optical system to collect the luminescent signals of the QD films under excitation light and calculated the

PLQY values through calibrated detectors. High PLQY values typically indicate lower non-radiative recombination pathways, which are crucial for achieving efficient photoelectric conversion. In my work, HAMAMATSU spectrometer is used for absolute PLQY measurement.[63,64]

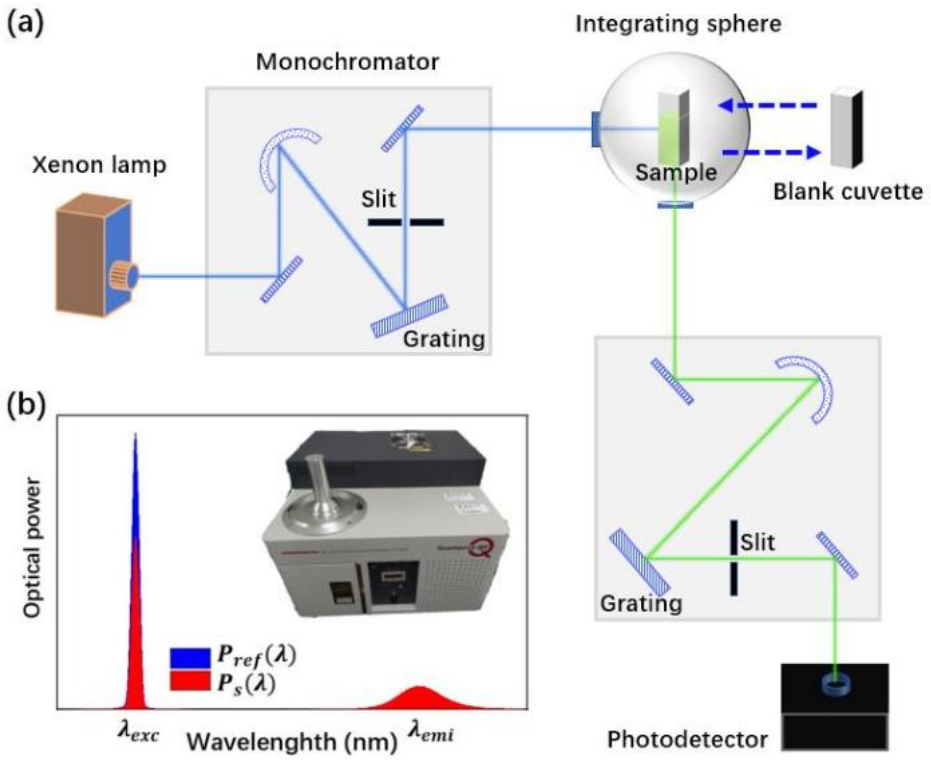

Figure 2.4 (a) The working principle diagram and (b) equipment diagram for PLQY measurement.

Ultraviolet Photon Spectroscopy (UPS) is a spectroscopic technique utilized for the investigation of the electronic structure of materials, particularly focusing on the band structure and electron density of material surfaces. This method predominantly

employs ultraviolet photons to stimulate electrons within the sample and measure their kinetic energy in order to acquire insights into the material's electronic structure. In UPS, ultraviolet photons (typically with energies ranging from 10-100 eV) are directed onto the surface of the sample, possessing sufficient energy to excite valence band or shallow electrons in the material, leading them to surpass the material's work function and emerge from its surface as photoelectrons. These stimulated photoelectrons are gathered by an energy analyzer which scrutinizes their distribution of kinetic energy. The kinetic energy of photoelectrons is correlated with their initial energy and the work function of the material.

The relationship between the kinetic energy of photoelectrons (E_k) and the energy of incident photons($h\nu$) can be expressed as:

$$E_k = h\nu - (E_B + \Phi),$$

where E_k represents the kinetic energy of photoelectrons, $h\nu$ denotes the energy of incident photons, E_B signifies the binding energy of electrons, and Φ indicates the work function of the material.

By measuring the kinetic energy of photoelectrons, it is feasible to calculate the binding energy of electrons in a material, which reflects their original state energy within that material. The distribution of binding energies offers valuable insights into the electronic density of states, band structure, and Fermi level in materials.

UPS is widely utilized in the fields of materials science, surface science, and semiconductor research. UPS is commonly employed for analyzing the surface

electronic states of metals, semiconductors, and insulators to provide information on surface state density, energy positions, and differences from bulk states. Secondly, UPS can accurately measure the work function of materials, which is a key parameter for understanding material surface chemical properties, electron emission capabilities, and contact potential differences. Thirdly, when studying thin films and interfaces, UPS aids in understanding changes in electronic structure at interfaces such as band alignment and interface state formation. In addition, UPS can be employed to investigate the adsorption behavior of gases or molecules on material surfaces and comprehend how adsorbates impact the electronic structure of surfaces. Moreover, in semiconductor device development, UPS is used to examine band bending at semiconductor surfaces, surface states, and barrier formation when in contact with metals. Overall, ultraviolet photoelectron spectroscopy offers detailed insights into the electronic state density, band structures, and work functions of material surface/interfaces through analysis of emitted photoelectrons' kinetic energy distribution from material surfaces. This information is essential for understanding the physical and chemical properties of materials.[65,66]

In my work, the Thermo Scientific Nexsa X-ray Photoelectron Spectroscopy (XPS) is primarily used for UPS testing of films, known for its high resolution and precise energy calibration. During the testing process, a 150 W argon plasma source is used for sample surface cleaning, and monochromatized Al Kα radiation (1486.6 eV) is used as the excitation source to obtain electron energy spectrum information from the valence

band edge to about 20 eV above, thereby providing a detailed analysis of the film's electronic structure and work function.

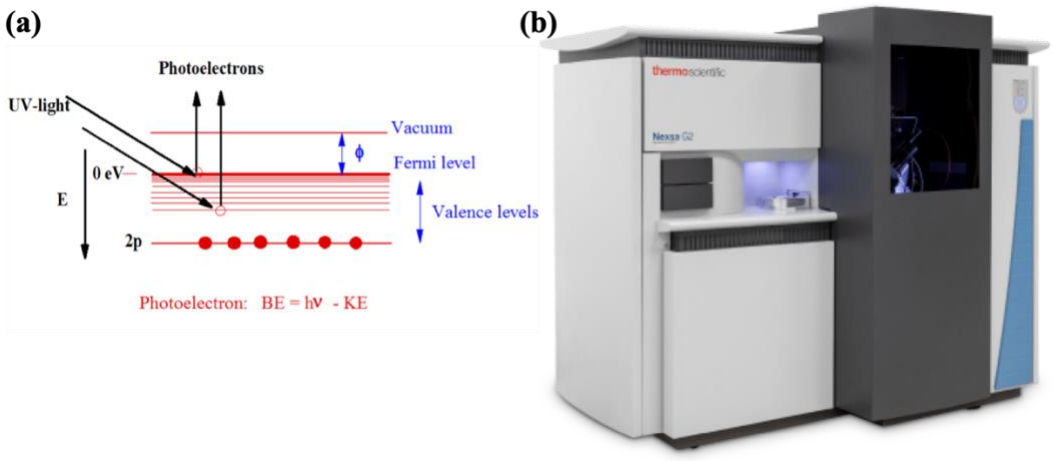

Figure 2.5 (a) The working principle for UPS measurement and (b) equipment diagram for XPS.

In summary, by comprehensively employing UV-VIS-NIR spectroscopy, PLQY measurement, and UPS analysis, we are able to fully characterize the optical and electronic properties of QD films, providing a solid experimental foundation and theoretical guidance for the design and performance optimization of QLED devices.

2.2.3 Dynamic and *in situ* characterization

In the research of QLED devices, dynamic and in-situ characterization techniques provide key information for understanding the behavior of the devices under operating conditions. These techniques can monitor the performance changes of the devices in

real-time, reveal the carrier dynamics process, and evaluate the interface quality, thus providing direct experimental evidence for device optimization.

Time-resolved photoluminescence (TRPL) is a technique used to measure the decay dynamics of excitons in QDs, distinguishing between radiative and non-radiative recombination pathways. Through TRPL, we can identify defect states and quantify their impact on device performance. Specifically, when the excitation light source illuminates the QD film, excitons form and subsequently decay within a short time frame. TRPL technology records the time-resolved signals of this process, helping us understand the lifetime and recombination mechanisms of excitons, which is crucial for improving the efficiency and stability of QLED devices.

In-situ ellipsometry provides a method for real-time monitoring of film thickness and optical properties, especially during the film deposition process. The application of this technique ensures precise control over layer uniformity and interface quality. Through in-situ ellipsometry, we can obtain changes in optical constants at each stage of film growth, allowing for real-time adjustments to deposition parameters to achieve optimal layer structure and performance. More importantly, we use it to obtain the optical characteristic parameters of the thin film to support simulation experiments.

In addition, we have also utilized two methods in the research from QD to thin films, and finally to devices. Although the final results did not demonstrate or support the conclusions in this paper, they played a significant role in identifying problems, proposing ideas, and designing strategies. In terms of nanoscale electrical mapping,

Conductive Atomic Force Microscopy (C-AFM) and Kelvin Probe Force Microscopy (KPFM) are two powerful tools. C-AFM maps local current paths by scanning the device surface under bias conditions, identifying "dead zones" where carrier traps are located. These "dead zones" may be caused by interface inhomogeneities between the ETL and the QD layer. C-AFM technology can accurately locate these areas, providing guidance for improving interface characteristics.

KPFM quantifies the band bending at heterojunctions by measuring the surface potential under illumination, providing direct evidence of charge transfer efficiency. Band bending is a key factor in charge injection and transport. The measurement results of KPFM help us understand the behavior of charges at interfaces and how to improve charge injection efficiency by adjusting interface characteristics.

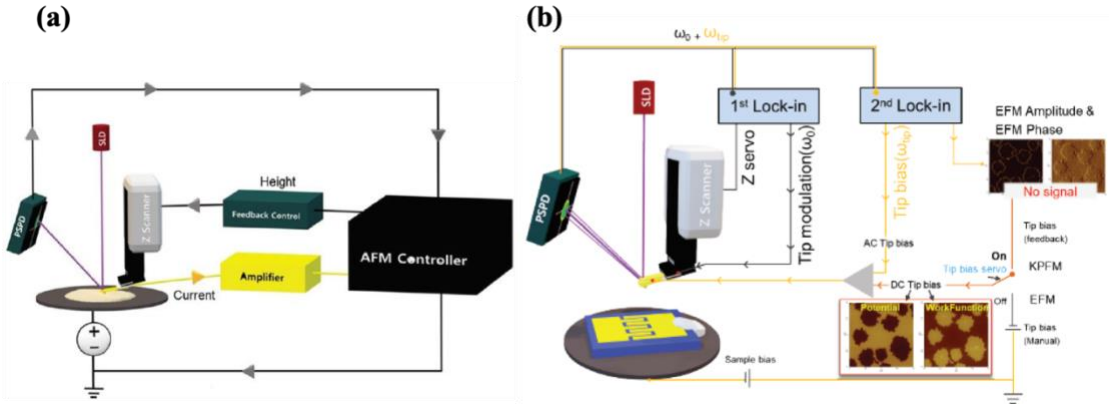

Figure 2.6 The working principle diagram of (a) C-AFM and (b) KPFM.

In summary, the combined use of dynamic and in-situ characterization techniques not only provides detailed information about the operation of QLED devices but also

reveals the underlying mechanisms affecting device performance, pointing the way for further optimization.

2.3 Thin-film deposition techniques

2.3.1 Spin-coating

Spin-coating is a commonly employed technique for the preparation of thin films, involving high-speed rotation of the substrate to achieve uniform coating of liquid materials and formation of a consistent thin film. Due to its simplicity, cost-effectiveness, and ability to control film thickness, spin-coating finds widespread application in microelectronics, optical devices, coatings, and organic electronic devices.

The working principle of spin coating involves a series of essential steps. Initially, the liquid coating material is dispensed onto the center of a smooth solid substrate, such as a silicon wafer or glass. As the substrate rapidly rotates, the coating material spreads outward due to centrifugal force, covering the entire surface. The speed and duration of rotation are critical in determining the thickness of the resulting thin film. Excess coating material is expelled during spinning, resulting in a uniform thin film on the substrate. Subsequently, solvents gradually evaporate during or after spin coating, leaving behind a solid-state thin film. By controlling environmental conditions such as temperature and humidity, it is possible to optimize solvent evaporation rate and ensure

film uniformity. In some cases, additional heat treatment may be necessary to cure the film and improve its physical and chemical properties. Overall, this process enables precise control over thin film deposition on various substrates for applications in fields such as microelectronics and optics.

The thickness of the film is primarily influenced by several key factors. Firstly, the rotation speed significantly impacts film thickness, with higher speeds resulting in thinner films due to increased centrifugal force dispersing more coating material onto the substrate surface. Additionally, viscosity of the coating liquid also affects film thickness, with higher viscosity leading to thicker coatings. Viscosity can be adjusted by altering solution concentration or using different solvents. Furthermore, extended rotation time typically further reduces film thickness as more solvent has sufficient time to evaporate. Lastly, the volatility of the solvent also plays a role, as solvents with higher volatility evaporate more rapidly and potentially result in thinner coatings.

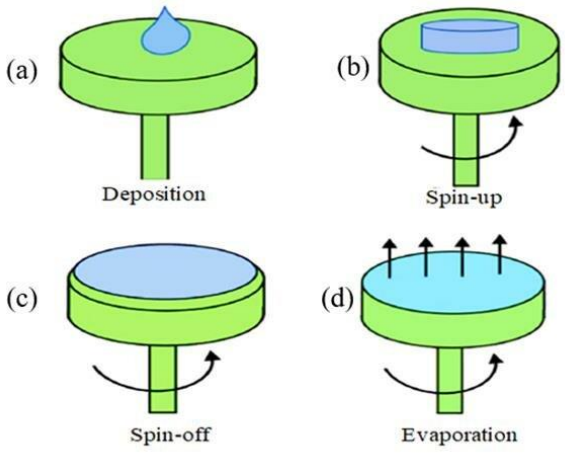

Figure 2.7 Spin-coating method for depositing thin films[67].

2.3.2 Thermal evaporation

Thermal evaporation is a well-established physical vapor deposition (PVD) technique widely employed for thin-film deposition on various substrates. This method involves heating a solid material, often a metal or organic compound, to its evaporation temperature, resulting in the material's transition to a gaseous state. The vaporized material then condenses on the substrate surface, forming a thin film. Due to its operational simplicity, cost-effectiveness, and versatility in handling a broad range of materials, thermal evaporation is extensively used in the fabrication of microelectronics, optical devices, and thin-film solar cells.

In the thermal evaporation process, the solid material, referred to as the target, is placed in a vacuum chamber equipped with an evaporation source, such as a resistive heating boat, electron beam heater, or arc heater. As the target material is heated, it reaches its evaporation temperature, causing it to transition from a solid or liquid state to a gaseous phase composed of atoms or molecules. Once the vapor pressure of the material is sufficient, these particles escape from the target surface and enter the vacuum chamber's gas phase, where they travel freely due to the low density of gas molecules in the vacuum environment. The evaporated particles eventually reach the substrate surface, where they condense and form a uniform thin film. The film's thickness can be controlled by adjusting the evaporation time, target temperature, and

substrate distance. To promote the uniform growth of the film, the substrate is often kept at a lower temperature during the process.

The vacuum environment, typically maintained between 10^-6 and 10^-9 Torr, plays a crucial role in the thermal evaporation process. It minimizes the likelihood of collisions between the evaporated material and air molecules, ensuring that the particles directly reach the substrate. Moreover, the vacuum prevents oxidation or other undesirable chemical reactions that could degrade the film's quality.

Thermal evaporation has a wide range of applications. In microelectronics, it is used to fabricate metal interconnect layers, electrode materials, and protective coatings for integrated circuits. In optics, it is employed to deposit thin films for mirrors, filters, and anti-reflective coatings on lenses. By carefully layering these films, specific optical properties, such as high reflectivity or selective wavelength transmission, can be achieved. In the realm of solar cells, thermal evaporation is used to deposit light-absorbing layers and transparent conductive oxides, such as indium tin oxide (ITO), which enhance photovoltaic conversion efficiency. Additionally, thermal evaporation is integral to the production of organic electronic devices. Furthermore, this technique is utilized for surface modification, where a protective thin film is deposited to enhance the wear resistance, corrosion resistance, or other surface properties of materials. In my works, the anode Al of the QLEDs and the functional layers in the optimization scheme are often deposited by evaporation coating.

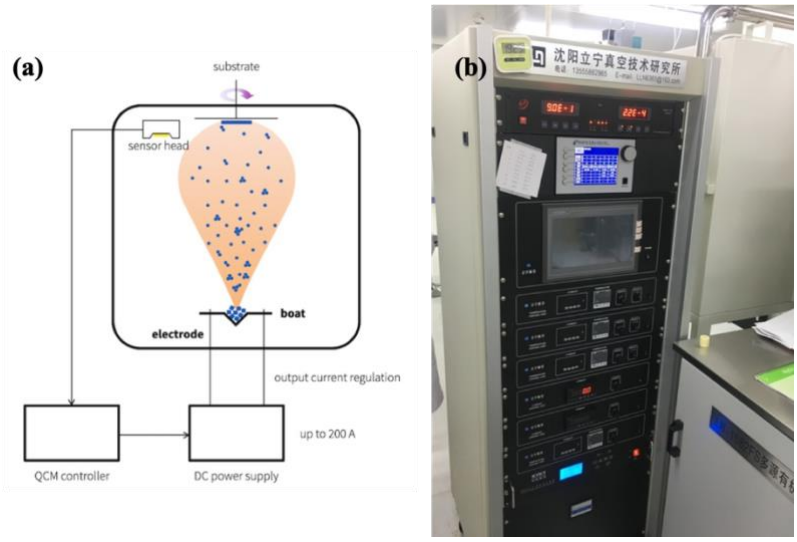

Figure 2.8 (a) The working principle and the (b) equipment for thermal evaporation.

Despite its numerous advantages, such as ease of operation, the ability to produce high-purity films, and broad material compatibility, thermal evaporation has certain limitations. The uniformity of the film thickness can be challenging to maintain, especially on large substrates, due to the linear deposition path of the evaporated material. Additionally, the technique may not be suitable for materials with very high evaporation temperatures, such as refractory metals or certain compounds. The process also requires considerable energy, particularly when high-temperature evaporation sources are employed.

In summary, thermal evaporation remains a versatile and widely used thin-film deposition technique. By precisely controlling the evaporation conditions, it is possible to achieve uniform and pure thin films on various substrates, meeting the demands of diverse fields.[68,69]

2.3.3 Magnetron sputtering

Magnetron sputtering is a sophisticated technique used in thin-film deposition, operating under the principles of PVD to create films on substrate surfaces. In the magnetron sputtering process, ions bombard a target material, causing atoms or molecules from the target to be ejected and subsequently deposited onto the substrate. Magnetron sputtering control involves real-time monitoring and regulation of this process to ensure the quality and characteristics of the deposited film meet the desired specifications.

The magnetron sputtering process begins within a vacuum chamber, where a high-voltage electric field ionizes an inert gas, typically argon (Ar), into plasma. The ionized argon atoms are accelerated by the electric field and directed towards the target material. When these high-energy argon ions collide with the target, they dislodge atoms or molecules from the target's surface. These ejected particles, now possessing significant kinetic energy, travel through the chamber and deposit onto the substrate, which could be a silicon wafer, glass, or other materials, forming a thin film.

Magnetron sputtering control technology plays a critical role in this process. It involves the continuous monitoring of various parameters during deposition, such as target temperature, plasma characteristics, deposition rate, and film thickness. By closely observing these factors, the state of film growth can be accurately assessed in real-time. This monitoring allows for feedback-based adjustments to the magnetron

sputtering conditions, such as modifying the pressure of the working gas, adjusting the sputtering voltage or current, to stabilize the deposition process and achieve the desired film properties.

The ability to control film characteristics through precise magnetron sputtering parameter adjustments is essential for tailoring the thin film to specific application requirements. These characteristics include film thickness, grain structure, surface morphology, stress state, and chemical composition. Such control is vital for ensuring that the film exhibits the necessary properties for its intended use, whether it be optical performance, electrical conductivity, hardness, or other critical attributes.[68,70]

In my work, the Kurt J. Lesker magnetron sputtering system, which I primarily use, features precise pressure control and sputtering rate adjustment capabilities. Its parameters include a maximum sputtering power of up to 300 watts, a base vacuum level in the sputtering chamber of up to 10^-8 torr, and multiple target positions for the growth of multilayer films. In this system, we deposit ITO (indium tin oxide) films through the magnetron sputtering process. This process involves high-energy argon ions impacting the target, sputtering indium and tin atoms from the target surface, which then deposit on the substrate to form a uniform and transparent conductive layer. This is crucial for enhancing the transparency and conductivity of the electrodes in QLEDs.

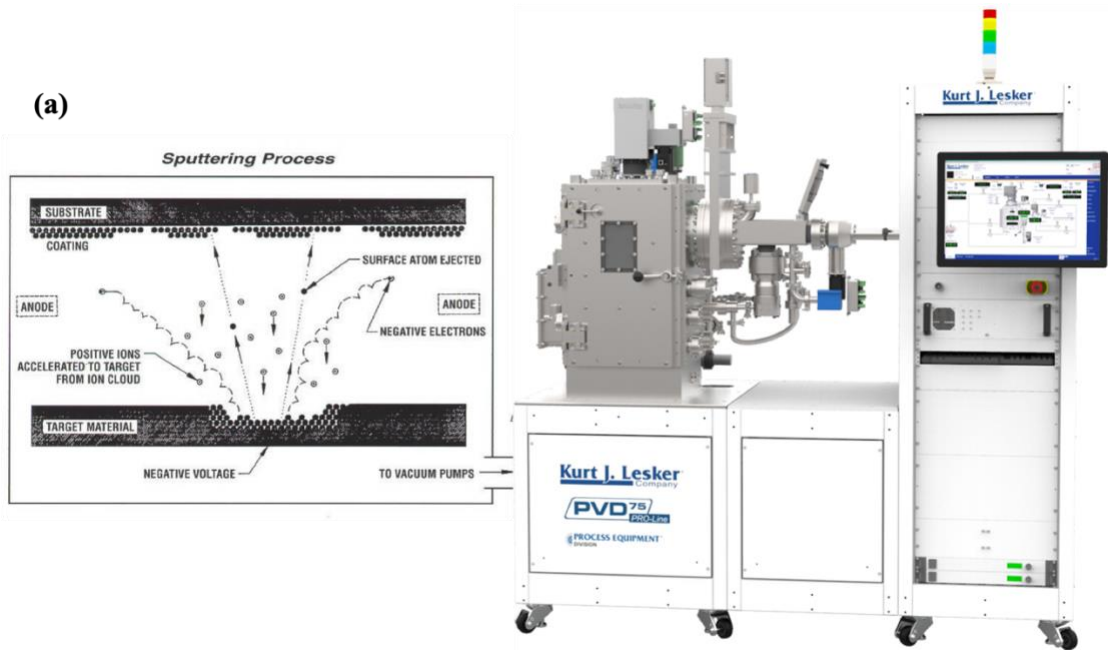

Figure 2.9 (a) The working principle and the (b) equipment for magnetron sputtering.

2.4 Device fabrication and characterization

2.4.1 Multilayer device fabrication and characterization

The fabrication of QLEDs typically involves the construction of a multi-layer structure, where each layer serves a specific function, working together to achieve efficient photoelectric conversion. The design of this multi-layer structure is key to the QLED device's ability to emit bright and stable light. The following is a detailed description of the functions of each layer and their preparation processes in QLEDs.

Firstly, the anode layer forms the foundation of the QLEDs, typically made of a transparent conductive oxide such as ITO (indium tin oxide). The transparency and

conductivity of the ITO layer ensure good hole injection efficiency, providing the necessary charge carriers for the entire device. The deposition of the ITO layer is usually achieved through magnetron sputtering, a method that can form uniform and strongly adherent films on the substrate.

Next is the HTL, commonly made from materials like PEDOT:PSS and PVK. These materials are responsible for effectively transporting holes injected from the anode while blocking electron penetration, thus improving the device's efficiency. The preparation of the HTL layer is typically done using spin-coating, a simple and cost-effective method that quickly forms uniform films.

Above the HTL layer is the QD EML, the core part of the QLED device. The EML consists of QDs, which emit light when electrons and holes recombine. The deposition of the QD layer is also typically done using spin-coating, but requires precise control of thickness and uniformity to ensure good luminescent performance.

Following the EML layer is the ETL, commonly made from materials like ZnMgO. It not only effectively transports electrons but also forms a good energy level match with the QD layer, promoting efficient recombination of electrons and holes in the QD layer. The deposition of the ETL layer is typically done using vacuum evaporation or sputtering, techniques that provide high purity and quality films.

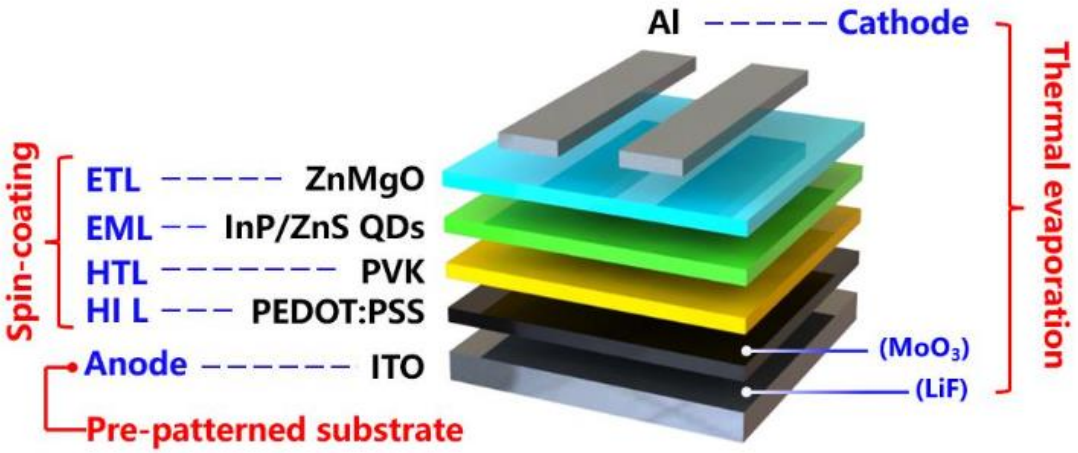

Figure 2.10 QLED multilayer structure.

Finally, the cathode layer is composed of metal electrodes such as aluminum (Al) or silver (Ag), used for electron injection. The deposition of the metal cathode is also done using vacuum evaporation, a technique that can precisely control the thickness of the film, thus optimizing electron injection efficiency.

After the deposition of each layer, annealing is typically performed to improve the quality of the films and the interfacial contact between layers. The annealing process can eliminate stress in the films and promote intermolecular interactions, thus improving the performance of the entire device.

In summary, the multi-layer preparation of QLED devices is a precise and complex process involving various deposition and post-treatment steps. Through careful design and preparation of each layer, we can construct high-performance QLED devices that achieve efficient and stable light emission.[71,72]

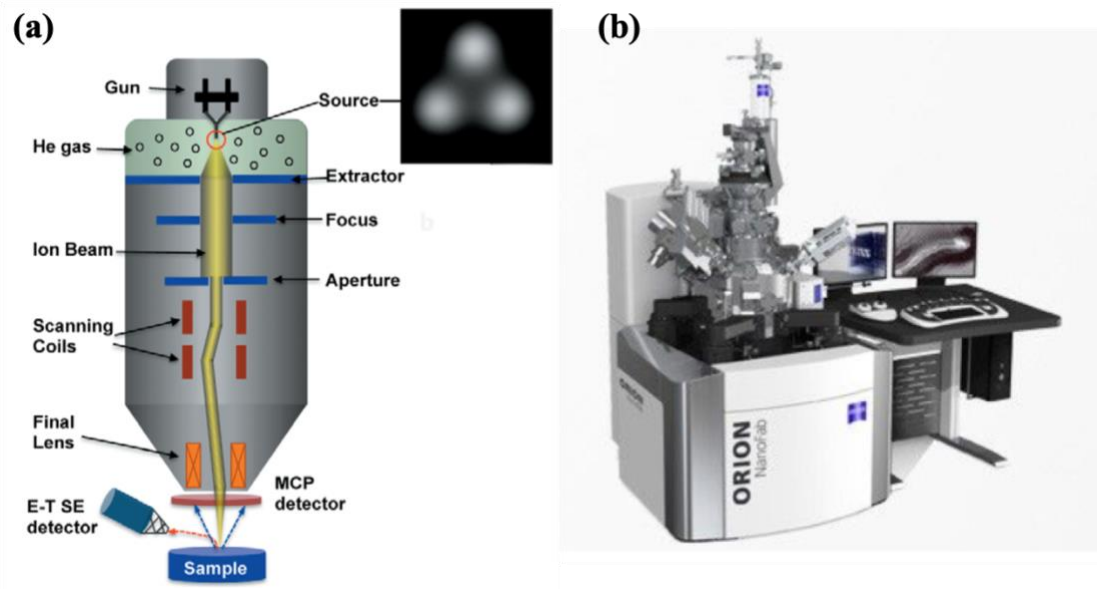

Figure 2.11 (a) The working principle diagram and (b) equipment diagram of HIM.

Helium Ion Microscopy (HIM) is a revolutionary imaging technology. This equipment uses a high-speed helium ion beam instead of the traditional electron beam, and because its wavelength is shorter than that of an electron beam, it can provide higher spatial resolution, reaching the sub-nanometer level. The Zeiss Orion NanoFab not only has high-resolution imaging capabilities but also integrates nanofabrication functions, allowing a series of operations from imaging to fine processing to be completed on the same device. Its working principle is based on the secondary electron signals produced by the interaction between helium ions and the sample, which are captured by a highly sensitive detector and converted into high-contrast images, thus enabling detailed analysis of the sample surface and cross-section.

In my work, the advanced technology of the Zeiss Orion NanoFab has been applied to the cross-sectional imaging of QLEDs. Using its unique helium ion beam, we are able to obtain ultra-high-resolution images of the internal structure of QLED devices, which clearly show each layer from the anode to the cathode, including the transparent conductive oxide layer, HTL, QD EML, ETL, and metal electrodes. Through this imaging technology, we can not only observe the microscopic structure of the device but also accurately measure the approximate thickness of each layer and evaluate the quality of the interfaces between layers. Additionally, the nanofabrication capabilities of HIM allow us to make fine modifications to the sample when necessary, optimizing device performance. Combined with these characterization data, we can gain a deeper understanding of the working mechanism of QLED devices and provide key guidance for their design and fabrication.

2.4.2 Device performance characterization

In the research and development of QLEDs, precise characterization of device performance is crucial. It not only helps us evaluate the actual performance of the device but also reveals the internal working mechanisms, providing guidance for performance optimization.

The device efficiency testing system for EQE consists of an Ocean Optics spectrometer, a Keithley digital source meter, optical fibers, a NEWPORT 1936-R optical power meter, and a NEWPORT 918D-IG optical probe. The digital source meter

provides the driving voltage, the spectrometer obtains the electroluminescence spectrum, and then the optical power meter and optical probe collect real-time light power.

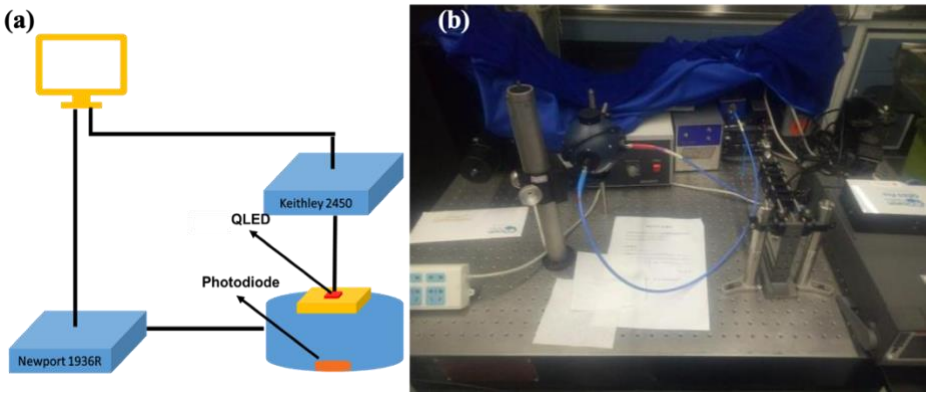

Figure 2.12 Device photoelectric characteristics testing system.

For QLEDs, we need to test radiation brightness, external quantum efficiency, and current-voltage curves. The current-voltage curve can be obtained directly from the Keithley source meter. Meanwhile, radiation brightness and EQEneed to be calculated from the optical power and current. EQEis defined as the ratio of the number of emitted photons to the injected electrons in a unit time, i.e., $I(V)/|e|$. Here, $I(V)$ refers to the current through the QLED under applied bias voltage V. We can express it as equation:

$$EQE(V)[\%] = \frac{N_{phot}(V)|e|}{I(V)} \cdot g \cdot 100$$

In the formula, $N_{phot}(V)$ represents the actual number of emitted photons collected by a photodiode in unit time; g represents the ratio of the actual number of emitted photons from a near-infrared QLED to the actual number of collected photons.

The actual number of photons collected in unit time can be obtained by dividing the power by the energy of a single photon:

$$N_{phot}(V) = \frac{P}{hc/\lambda}$$

In the formula, P represents the real-time power (W) collected by the optical power meter; h stands for Planck's constant ($4.16 \times 10^{-15}\ eV \cdot S$); c represents the speed of light in vacuum ($3 \times 10^{8}\ m/s$); and λ denotes the position (nm) of the electroluminescent peak collected by the spectrometer.

Assuming the near-infrared QLED behaves as a Lambertian source (i.e., with uniform radiance in all directions and a divergence angle of π), the geometric factor g is given by equation:

$$g = \frac{a^2 + L^2}{a^2}$$

In the formula, a represents the radius (in mm) of the active region of the photodiode; L represents the distance (in mm) between the emission area of the QLED and the active region of the photodiode.

Radiance (Le) is defined as the radiant flux per unit area and unit solid angle in that direction:

$$Le = \frac{Pg}{\pi S}$$

In the equation, S represents the area of the emission region of a QLED (m^2).

The Current-Voltage (I-V) characteristic curves are obtained through source meter measurements, providing important information for evaluating the electrical behavior of QLED devices. During the measurement process, the source meter applies different voltages to the device while measuring the current through it. The resulting I-V curves reveal key parameters such as the turn-on voltage, series resistance, and leakage current of the device. The turn-on voltage is the voltage at which the device begins to conduct, reflecting the threshold for electron injection into the device. Series resistance is related to the internal resistance of the device and affects its power efficiency. Leakage current is the current that flows through the device when it is off, usually associated with device defects and interface states.

Capacitance-Voltage (C-V) analysis is a technique used to study carrier distribution and interface states in QLED devices. Through C-V measurements, we can obtain information about the internal electric field distribution and charge accumulation in the device, which is crucial for understanding the charge transport mechanism. In C-V measurements, different voltages are applied to the device, and its capacitance response is measured. Changes in capacitance reflect the accumulation and depletion of carriers in the device, helping us identify bottlenecks in charge transport. For example, if the capacitance curve shows abnormal shifts or peaks, this may indicate the presence of interface defects or charge traps, both of which can affect device performance.

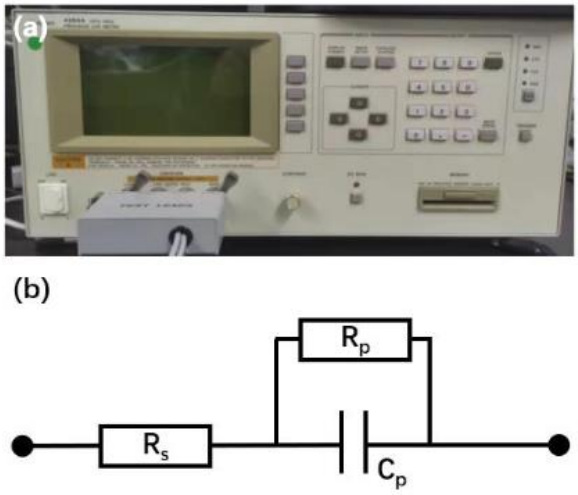

Figure 2.13 C-V measurement system

In summary, through comprehensive characterization of cross section, EQE, I-V characteristics, and C-V analysis, we can gain a comprehensive understanding of the performance of QLED devices, identify potential issues, and provide scientific basis for device design and fabrication. The application of these characterization techniques is of great significance for advancing the commercialization of QLED technology.

2.4.3 Stability and reliability testing

In the commercialization process of QLED technology, ensuring the stability and reliability of devices is crucial. To simulate and predict the long-term performance of QLED devices in practical applications, we have implemented various stability and reliability tests, including accelerated aging tests and bias-stress testing.

Accelerated aging tests are a standard method for evaluating the performance changes of QLED devices under extreme environmental conditions. In this test, devices

are placed in high-temperature and high-humidity environments, which accelerate the aging process of materials, simulating the performance changes that devices might experience over several months or years under normal operating conditions. Specifically, we monitor changes in the device's luminance, efficiency, and leakage current over time. A decrease in luminance may indicate a decline in the optical performance of the luminescent material, a decrease in efficiency reflects a weakening of the device's overall photoelectric conversion capability, and an increase in leakage current may be due to more defects or damage within the device. These parameter changes provide direct evidence of the device's stability and help us identify key factors that may lead to device failure.

Subsequently, bias-stress testing involves continuous operation of the device under high driving currents to reveal performance degradation mechanisms under long-term high-load operation. This test simulates high-intensity usage scenarios that devices might encounter in practical applications by applying currents higher than normal operating conditions. Continuous high-current driving can lead to phenomena such as charge trapping, material degradation, or interface degradation within the device, which are potential causes of efficiency decline. For example, charge traps can lead to increased carrier recombination, thereby reducing the device's luminescence efficiency. By monitoring the efficiency decline, we can infer the device's stability under high currents and optimize the device structure or material selection to improve its long-term reliability.

During these tests, we adhere to strict standard operating procedures to ensure the accuracy and reproducibility of the test results. We record detailed experimental data and conduct in-depth analysis. By comparing data under different test conditions, we can identify the main factors affecting device stability and provide scientific basis for device improvement. Additionally, we use statistical methods and machine learning algorithms to analyze the data, aiming to discover hidden patterns and trends behind the data, thereby more accurately predicting the long-term performance of the device.

In summary, through accelerated aging tests and bias-stress testing, we can comprehensively evaluate the stability and reliability of QLED devices. These tests not only help us understand the behavior of devices under extreme conditions but also provide valuable feedback for the optimization design of devices. Through these comprehensive tests and analyses, we are committed to enhancing the performance of QLED devices, laying a solid foundation for their widespread application in the market.

Chapter 3

Light extraction: Optical tunneling strategy in low-SPP devices

3.1 Introduction and optical fundamentals

3.1.1 Light extraction efficiency

The performance of QLEDs is mainly evaluated from two aspects: optical performance and electrical performance. Luminescent properties include luminescent spectrum, brightness, chroma, lifetime and luminescent efficiency. Luminescence spectrum refers to the relative intensity of various wavelength components in the emitted light, or the relative intensity distribution of fluorescence with the wavelength. The unit of luminous intensity is $cd \cdot m^{-2}$, which represents the luminous intensity per square meter. Chromaticity reflects the hue and saturation of the light color. Life is defined as the time required to reduce the initial brightness to half. In addition, some electrical properties are also the main aspects of the device. Including current density, current efficiency (CE), the relationship between brightness and voltage, etc.

Luminescence efficiency can be defined as quantum efficiency, lumen efficiency and power efficiency. Quantum efficiency is composed of internal quantum efficiency (IQE) and external quantum efficiency (EQE).

EQE is defined as the ratio of the number of photons emitted from the light emitting device in a certain direction to the number of electrons injected, or defined as the ratio of the number of photons emitted from the device in the whole space to the number of electrons injected. The EQEcharacterizes the ability of the device to convert electrical energy into external visible light energy. The higher the external quantum efficiency, the higher the luminescence efficiency.

Injection efficiency (η_{Inj}) refers to the ratio of the number of electron hole pairs produced by the EML to the number of electrons injected into the device.

Internal quantum efficiency (IQE) refers to the ratio of the number of photons emitted by the EML (including the photons absorbed by the device itself, scattered and reflected by the surface of the device) to the number of electron hole pairs. Internal quantum efficiency reflects the efficiency of exciton formation and recombination emitting of carriers in the device and describes the internal physical mechanism of the device. IQE also provides characterization for the ability of EML to convert the injected electric energy into light energy.

Light extraction efficiency (LEE) is defined as the ratio of the number of photons emitted into space per unit time to the number of photons emitted from the EML. The

ability of the device to emit the light generated by the EML is characterized. The relationship between it and internal and EQEis shown in formula (1), (2), and (3).

$$IQE = \frac{Number\ of\ photons\ emitted\ by\ the\ emitting\ \ layer\ per\ unit\ time}{Number\ of\ electron\ hole\ pairs\ in\ the\ emitting\ layer\ per\ unit\ time} \quad (1)$$

$$LEE = \frac{Number\ of\ photons\ emitted\ into\ space\ per\ unit\ time}{Number\ of\ photons\ emitted\ by\ the\ emitting\ layer\ per\ unit\ time} \quad (2)$$

$$EQE = \frac{Number\ of\ photons\ emitted\ into\ space\ per\ unit\ time}{Number\ of\ electrons\ injected\ into\ the\ device\ per\ unit\ time} = \eta_{Inj} \times IQE \times LEE \quad (3)$$

Despite the effective elimination of nonradiative recombination pathways in QDs, EQE in conventional QLEDs remains severely limited by low light extraction efficiency[73]. Thus, it is very meaningful to improve the efficiency of light extraction.

3.1.2 Optical modes and mechanisms of light loss

QLEDs as a novel display technology, see their performance largely determined by the Light Extraction Efficiency (LEE). LEE is one of the key parameters in assessing the performance of QLED devices, impacting their overall light-emitting efficiency. The LEE specifically quantifies the proportion of photons emitted from the active region into free space. LEE represents the proportion of photons emitted from the active region into free space. For planar QLEDs, the approximate formula is:

$$LEE = 1 - \left(1 - \frac{1}{n_{EML}^2}\right)^{1/2}$$

where n_{EML} is the refractive index of the EML.

In planar QLED structures, an approximate formula reveals the relationship between LEE and the device's structural parameters. The value of LEE directly affects

the device's luminous performance. There exists a negative correlation between the refractive index and light confinement, meaning that a higher refractive index material tends to exhibit a more pronounced light waveguide effect. Figure 3.1 is based on ray-optics neglecting interference effects, showing how the larger EML index leads to smaller LEE. For instance, ZnSe/ZnS QD films, with a refractive index of about 1.75, lead to a strong waveguide effect. In such cases, the theoretical LEE is only 18%, significantly lower than the 20% of traditional OLEDs.

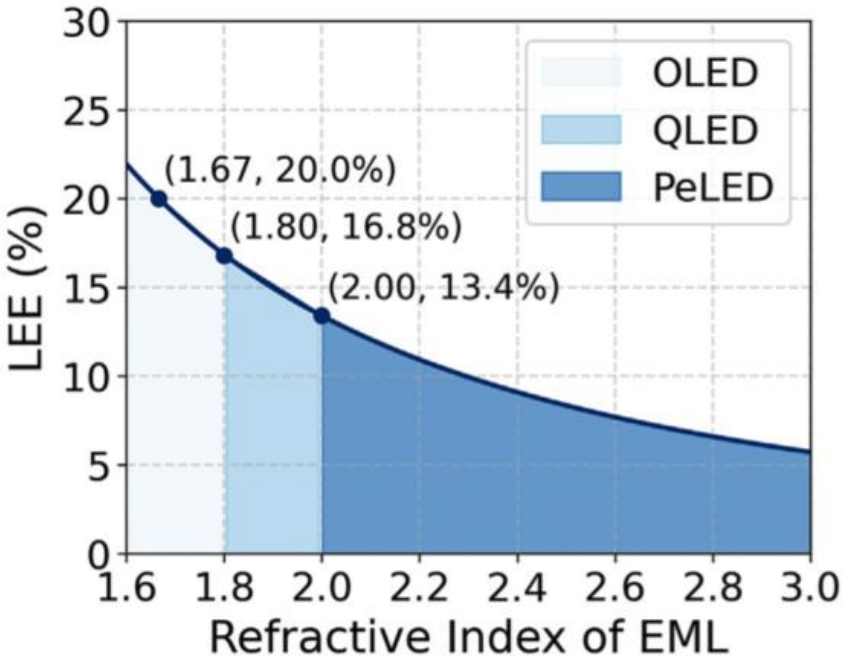

Figure 3.1 The LEE under different refractive indexs of the EMLs.

Moreover, if we adopt materials with even higher refractive indices, the challenge in achieving efficient light extraction in QLEDs becomes even more severe. While high refractive index materials can enhance the device's light-emitting efficiency to some extent, they also intensify the light waveguide effect, causing more photons to undergo

total internal reflection within the device and preventing their effective extraction into free space. Consequently, improving the LEE of QLEDs with high refractive index materials has become a pressing issue for researchers.

Like organic light-emitting diodes (OLEDs), QLEDs are multi-layer thin film stacked structures. The composition and thickness of each layer are the main factors affecting the transmission of electromagnetic radiation at the interface. Optical model can be used to study the optical transmission performance and field intensity distribution of the devices. The traditional device dipole model method can be extended to the study of organic light-emitting diodes and QLEDs. The theoretical basis of dipole model method was first proposed by Sommerfeld, which mainly studied the propagation of electromagnetic wave radiation at various interfaces. Figure 3.2 shows the energy ratio in the coupling modes of OLED devices with different thickness of ETL. Thus, various coupling modes in organic light emitting diodes can also be seen.

In QLED technology, light loss is an important factor affecting device performance. To better understand and optimize QLED devices, we can categorize light loss into the following five modes:

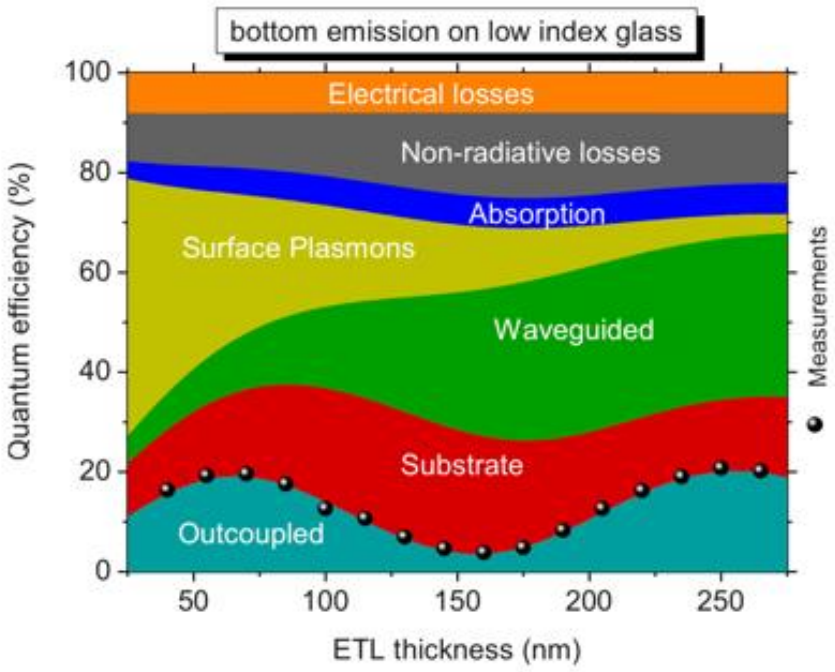

Figure 3.2 The influence of ETL thickness on the energy ratio of each coupling mode of the device[74]

We should try our best to let the light out to the outside and increase the emission to air of light to improve the efficiency of light extraction.

Air Mode: This portion of light loss refers to the light that radiates directly from the active region to free space. Ideally, this light is the most desirable to be extracted as it directly constitutes the device's luminous output. However, in actual QLED devices, the proportion of light in the air mode is only about 15%, meaning that most photons do not escape directly from the device.

Substrate Mode: This light loss occurs due to total internal reflection (TIR) at the interface between the substrate and air. When light travels from a high refractive index substrate to a low refractive index air, if the angle of incidence is greater than the critical

angle, TIR will occur, trapping this light within the device and preventing effective extraction. The light loss in the substrate mode accounts for about 20%, making it a significant source of loss in QLED devices.

Absorption Mode: This light loss is caused by the absorption of light by the electrode or functional layer materials. In QLED devices, the electrodes and certain functional layer materials may absorb a portion of the photons, converting them into heat, thereby reducing the overall luminous efficiency of the device. This loss is typically related to the material's absorption coefficient and thickness.

Waveguide Mode: The light loss in the waveguide mode is due to the confinement of light propagating in high refractive index functional layers (such as the EML, HTL, and ETL). The waveguide effect in these layers causes photons to undergo multiple reflections and refractions within the device, making it difficult for them to escape to the external space. The light loss in the waveguide mode accounts for about 37%, making it one of the largest sources of loss in QLED devices.

Surface Plasmon Polariton (SPP) Mode: This light loss is caused by non-radiative losses resulting from the coupling of evanescent waves at the interface between the metal electrode and the dielectric. When light waves propagate along the surface of the metal electrode, they can excite surface plasmon polaritons, which then propagate along the metal surface and eventually dissipate as heat, leading to light loss. This loss mode is particularly significant in QLED devices that include metal electrodes.

To improve the efficiency and performance of QLED devices, researchers need to take appropriate optimization measures for the different light loss modes mentioned above. For example, designing more effective light extraction structures to reduce light loss in the air and substrate modes, selecting materials with low absorption coefficients to decrease light loss in the absorption mode, and using methods such as photonic crystals to reduce light loss in the waveguide and SPP modes. By these methods, the luminous efficiency and stability of QLED devices can be significantly enhanced.

3.2 Improvement of light extraction efficiency

The methods to improve the light extraction efficiency can be roughly divided into external light extraction (ELE) technology and internal light extraction (ILE) technology by modifying the position of the interface. External light extraction technology mainly extracts the light of the substrate mode. Internal light extraction technology mainly extracts light from waveguide mode and surface plasmon polaritons mode.

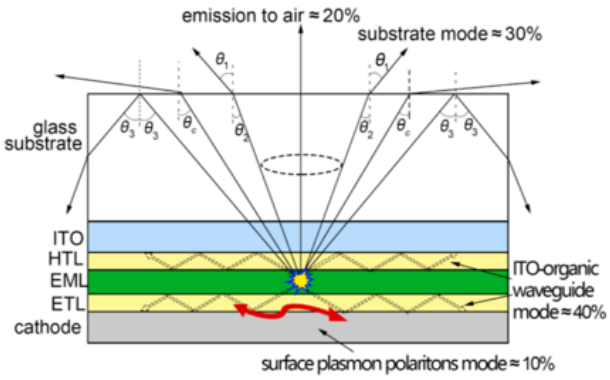

Figure 3.3 Optical radiation modes in traditional devices[75]

3.2.1 External light extraction

External light extraction techniques are primarily aimed at addressing the substrate mode by altering the interface between the substrate and air to reduce internal total reflection. This allows more light to be coupled outwards, thereby enhancing the light extraction efficiency. This section will explore several common external light extraction methods in detail, including surface roughening, microlens arrays, surface-patterned films, and layers with surface scattering properties.

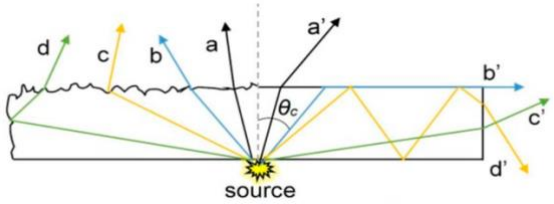

Figure 3.4 Ray propagation after roughening substrate[75]

Surface roughening is a straightforward and effective approach to boost light extraction efficiency. By increasing the roughness of the glass substrate in a random fashion, it enhances the scattering of light at the interface. This not only increases the surface area available for light emission but also helps in coupling out light that would otherwise be trapped in the substrate mode. Various methods are employed for roughening, such as direct grinding, sandblasting, and solution etching.[76–78]

Direct Grinding: By using hard particles to directly grind the glass substrate, an irregular roughness can be achieved, thereby improving the light extraction efficiency. Sandblasting: Utilizing high-speed air flow to spray fine sand particles onto the glass

substrate surface, it is possible to create a uniform roughness, thus enhancing the light extraction efficiency. Solution Etching: By using a chemical solution to etch the glass substrate surface, specific roughness can be formed, thereby improving the light extraction efficiency.

Research has shown that surface roughening can increase the current efficiency and quantum efficiency of QLEDs without altering their emission spectrum and Lambertian emission characteristics.

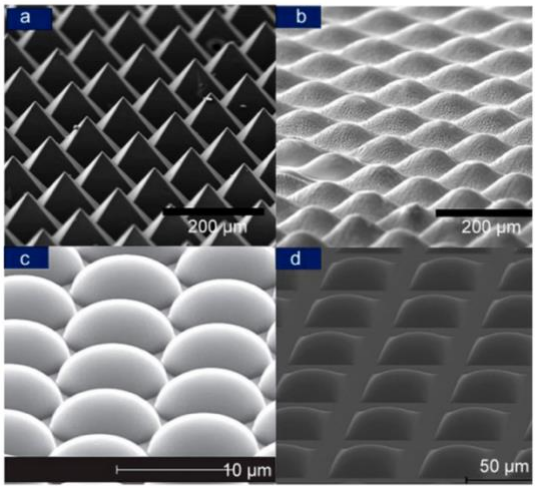

Figure 3.5 Microlens array films of various shapes photographed by SEM[79,80]

Micro-lens arrays are optical elements that can converge and diverge light radiation. In PeLEDs, micro-lens arrays can amplify the emission area of light and focus it into the air, thereby improving light extraction efficiency. Additionally, micro-lens arrays can also serve as a buffer layer with a matched refractive index, further suppressing internal total reflection. Research has shown that micro-lens arrays can enhance the EQEQLEDs, and their shape and size can be optimized to further improve

light extraction efficiency. Surface patterned films utilize patterns to scatter light multiple times before finally emitting it into the air. Common patterning methods include transfer printing.

External light extraction techniques are effective methods for enhancing the light extraction efficiency of QLEDs. Technologies such as surface roughening, micro-lens arrays, surface patterned films, and surface scattering media layers can all effectively improve the light extraction efficiency of QLEDs, each with its own advantages and limitations. In the future, with the continuous development of material preparation and processing technologies, external light extraction techniques will be further optimized, providing important technical support for the development and application of QLEDs.

3.2.2 Internal light extraction

Internal light extraction methods primarily focus on addressing the waveguide mode and Surface Plasmon Resonance (SPR) mode issues in optoelectronic devices. These methods involve modifying the internal structure of the device to suppress the formation of these modes, thereby increasing the light extraction efficiency. This section will explore several widely used internal light extraction methods, such as layer insertion, patterning of transparent electrodes, the use of photonic crystals, and nanoparticle insertion.

The layer insertion method enhances light extraction efficiency by altering the way light propagates within the device. This is achieved by inserting layers made of scattering materials or materials with a low refractive index, such as PEDOT:PSS (a conductive polymer blend) and Random Scattering Layers (RSL), which help to reduce the waveguide effect.

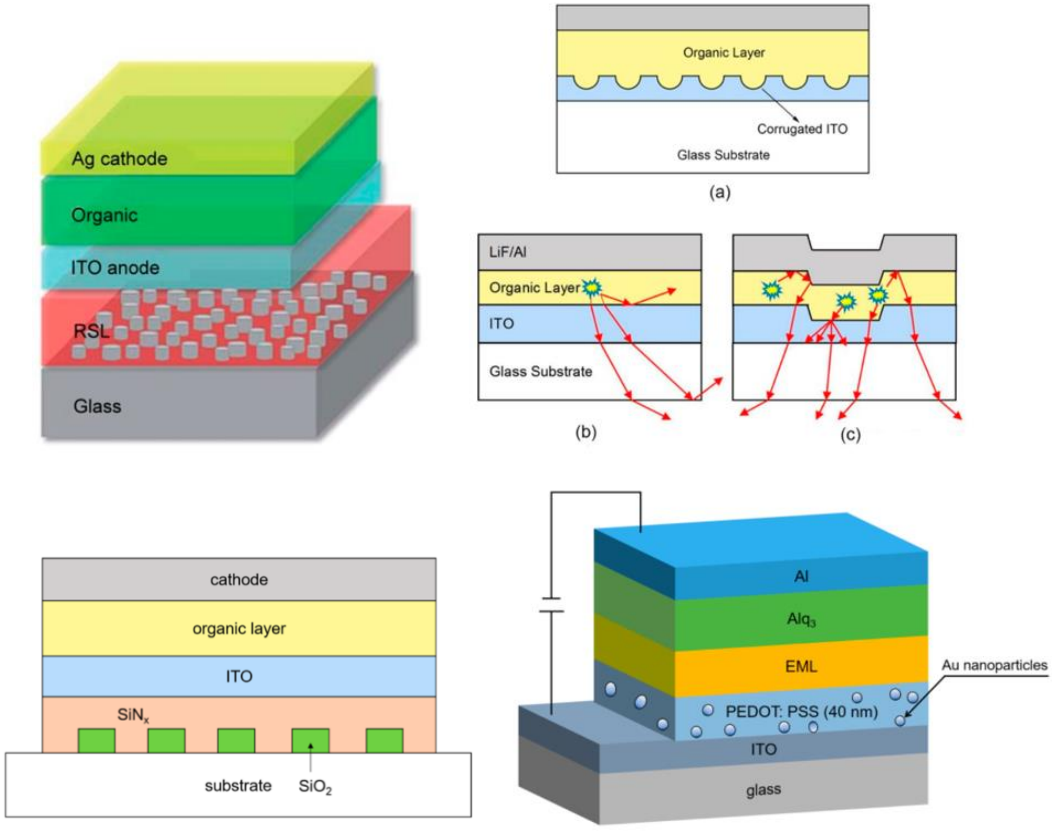

Figure 3.6 Some device structures for internal light extraction methods[81–84]

The technique of patterning transparent electrodes, such as indium tin oxide (ITO), involves creating a structured surface rather than a flat film, which increases the surface area for light emission and enhances scattering, thereby improving light extraction efficiency. Photonic crystals, which are artificial microstructures made of dielectric

materials with varying refractive indices arranged in a periodic pattern, can control the transmission of light by preventing specific wavelengths from passing through, thus enhancing light extraction efficiency. The nanoparticle insertion method involves adding metal nanoparticles within the device to suppress surface plasmon resonance (SPR) modes at the metal-dielectric interface and to enhance the radiative efficiency of fluorescent molecules through SPR, leading to improved light extraction efficiency.[81–84]

Internal light extraction techniques are also key to enhancing the light extraction efficiency of QLEDs. These techniques each have unique strengths and limitations. Looking forward, as material synthesis and processing technologies advance, internal light extraction methods will be further refined to minimize any adverse effects on the electrical properties of QLEDs, thereby broadening their range of practical applications.

3.3 From theory to combination scheme design

3.3.1 Geometric optics and the principles governing Snell's law

In QLED devices, when light propagates from a high refractive index of EML ($n_{EML} \approx 1.8–2.0$) to a low refractive index of HTL, ($n_{HTL} \approx 1.52$), according to Snell's law ($n_{EML} \sin\theta_i = n_{HTL} \sin\theta_t$), light will undergo total internal reflection (TIR) when the incident angle exceeds the critical angle ($\theta_c = \arcsin(n_{HTL} / n_{EML})$), resulting in a

waveguide mode accounting for up to 37% of the light. This reflection is an inevitable consequence of traditional geometric optics but also represents a major bottleneck for theLEE of QLEDs.

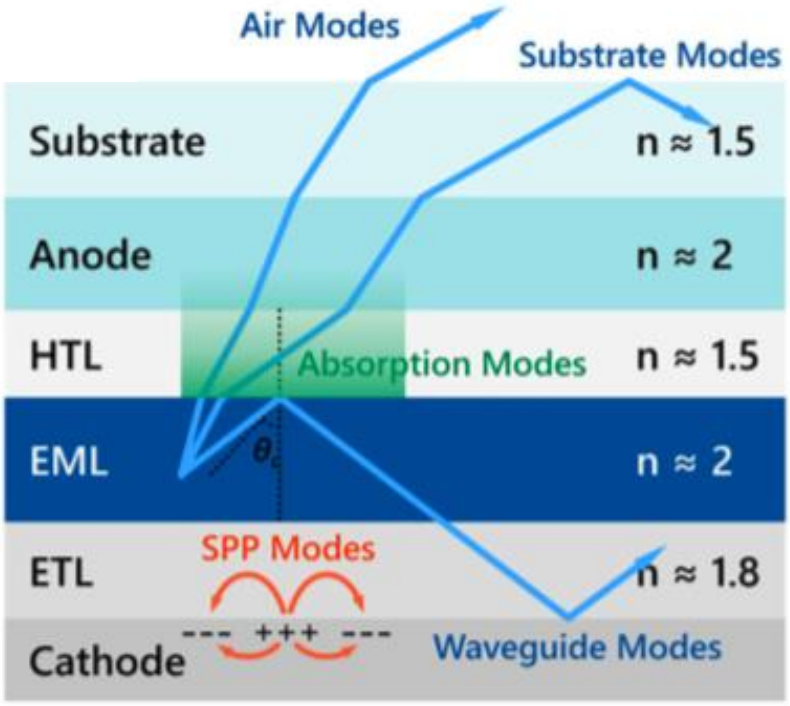

Figure 3.7 Optical channels in QLEDs

For ZnSe/ZnS QD EMLs (n = 1.75), the critical angle is approximately 60°, and light beyond this angle is completely confined within the EML, with only about 18% of the light escaping through the air mode. In contrast, OLEDs have a lower EML refractive index (n = 1.6 − 1.7), resulting in a larger critical angle and slightly higher LEE (approximately 20%). Therefore, it is necessary to increase the LEE in cadmium-free and lead-free QLEDs.

3.3.2 Optical tunneling and frustrated total internal reflection

Although geometric optics predicts that TIR will completely block light propagation, wave optics reveals the possibility of optical tunneling. When the thickness of the HTL is less than the wavelength of light (e.g., <100 nm), evanescent waves can penetrate the low refractive index layer and enter the high refractive index anode (such as ITO, n ≈ 2.0), a phenomenon known as Frustrated Total Internal Reflection (FTIR). The physical mechanism behind this is the exponential decay characteristic of evanescent waves:

$$E(z)=E_0 e^{-kz},$$

$$k = \frac{2\pi}{\lambda}\sqrt{n_{EML}^2 sin^2\theta_i - n_{HTL}^2}$$

and z is the penetration depth. By thinning the HTL (Figure 3.8), the light penetration capability can be significantly enhanced, allowing some of the waveguide mode to be converted into extractable light.

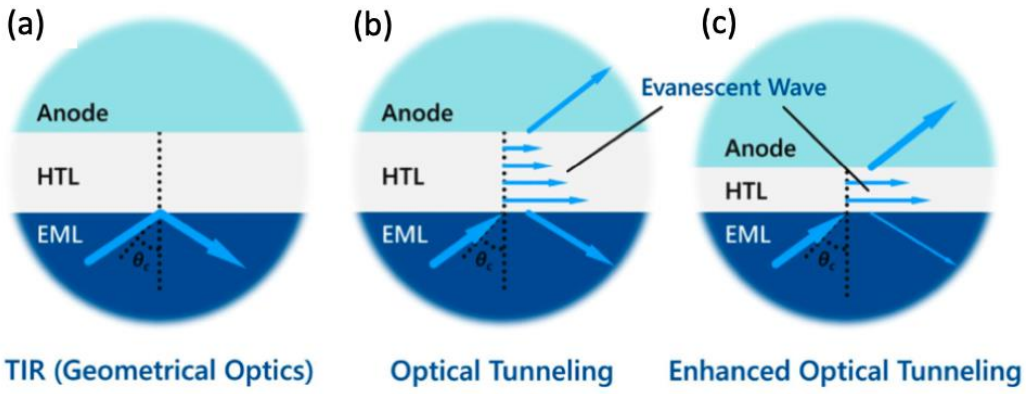

Figure 3.8 (a) Geometrical optics is used to determine the TIR at the boundary between EML and HTL. (b) The propagation of light from EML to the anode is made possible by FTIR or optical tunneling. (c) Enhanced optical tunneling is achieved with a thinner HTL layer.

Studies have shown that when the HTL thickness is reduced from 150 nm to 50 nm, the LEE of QLEDs increases from 15% to 22%, verifying the effectiveness of optical tunneling. Derived from the exponential attenuation of the evanescent wave field, the thin HTL facilitates stronger optical tunneling. HTL is thin enough in our device to achieve enhanced optical tunneling.

3.3.3 High refractive index substrates and mode conversion techniques

Optical tunneling allows the high-index substrate to convert waveguide modes into substrate modes. As shown in Figs. 3.10 (a) and 3.10 (b), once the light propagates

to the anode–substrate interface through optical tunneling, a high-index substrate can sequentially transfer it to substrate modes.

In this case, the external extraction structure (EES) aiming to extract substrate modes can also extract original waveguide modes [Fig. 3.10 (c)]. Then, the EES rather than the internal extraction structure is used to extract the original waveguide modes and substrate modes. At the same time, complex fabrication processes and influences on internal carrier injection can be avoided.

So, a high-index substrate converts waveguide modes to substrate modes. Surface roughening converts substrate modes to air modes.

3.4 Combination scheme design and simulation

In response to the significant waveguide mode loss and surface plasmon polariton (SPP) coupling issues in blue ZnSe QLEDs, this study proposes a comprehensive light extraction strategy based on optical tunneling and microcavity control. The core idea is to optimize the device structure under low SPP microcavities to recouple the SPP mode energy to the waveguide mode and to utilize high refractive index substrates and surface roughening techniques for multistage photon extraction.

3.4.1 Decoupling of SPP and enhancement of waveguide mode

In traditional QLED structures, the QD EML is close to the metal cathode (Al), leading to significant near-field SPP coupling. To suppress this loss, an ITO Spacer layer is introduced to increase the distance between the EML and the metal cathode (Figure 3.9). According to microcavity theory, the addition of the ITO layer (refractive index ~1.95) can adjust the resonance order of the microcavity, placing the QD layer at the second anti-node position. In this case, the overlap between the radiation field of the emission dipole and the evanescent field of the SPP is reduced, significantly decreasing the SPP coupling efficiency. Numerical simulations reveal that when the ITO Spacer thickness is 120 nm, the proportion of the SPP mode decreases from the initial 32% to less than 5% (Figure 3.9c), while the waveguide mode increases to 43%, providing ample free photons for subsequent light extraction.

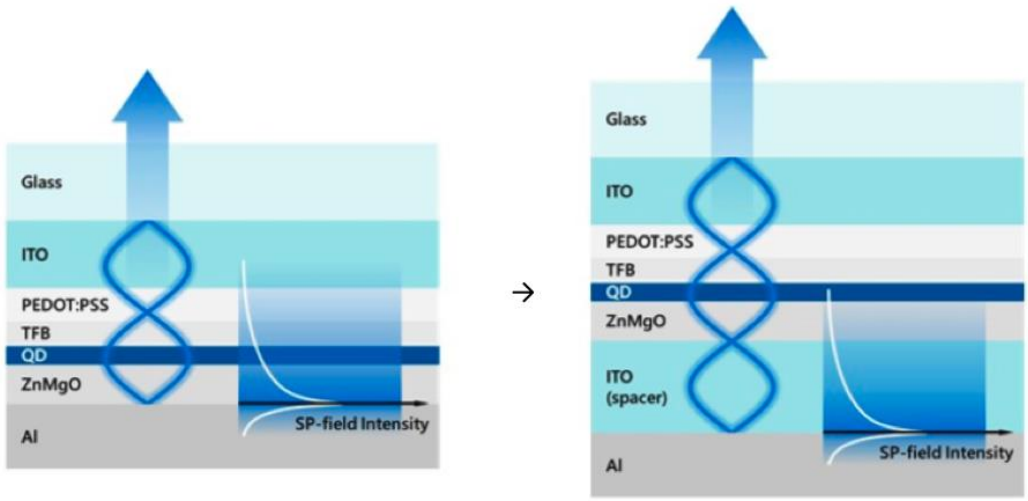

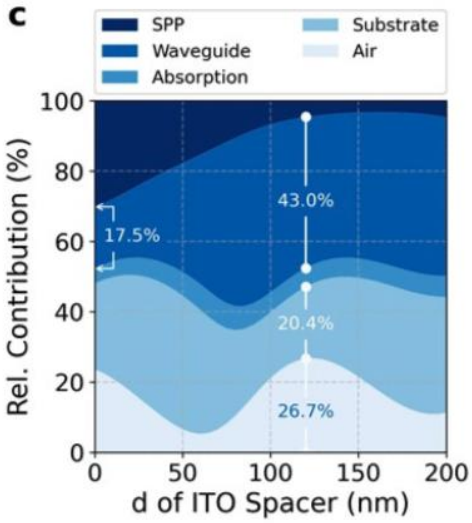

Figure 3.9 The design adds ITO Spacer to construct a second order microcavity to release the energy in SPP mode

3.4.2 Optical tunneling and substrate mode conversion

Photons in the waveguide mode need to penetrate the low refractive index HTL, such as PEDOT:PSS (n=1.52) to reach the anode/substrate interface. According to wave optics theory, when the HTL thickness is smaller than the light wave penetration depth, photons can tunnel through the HTL into the high refractive index substrate (n=1.7-1.9) via optical tunneling. In this case, the interface between the substrate and air forms total internal reflection due to refractive index mismatch ($n_{substrate} > n_{air}$), trapping photons as the substrate mode. Simulations show that when the substrate refractive index increases from 1.5 to 1.9, the proportion of the substrate mode increases

from 21s.4% to 60.2% (Figure 3.10d), verifying the effective conversion of the waveguide mode by the high refractive index substrate.

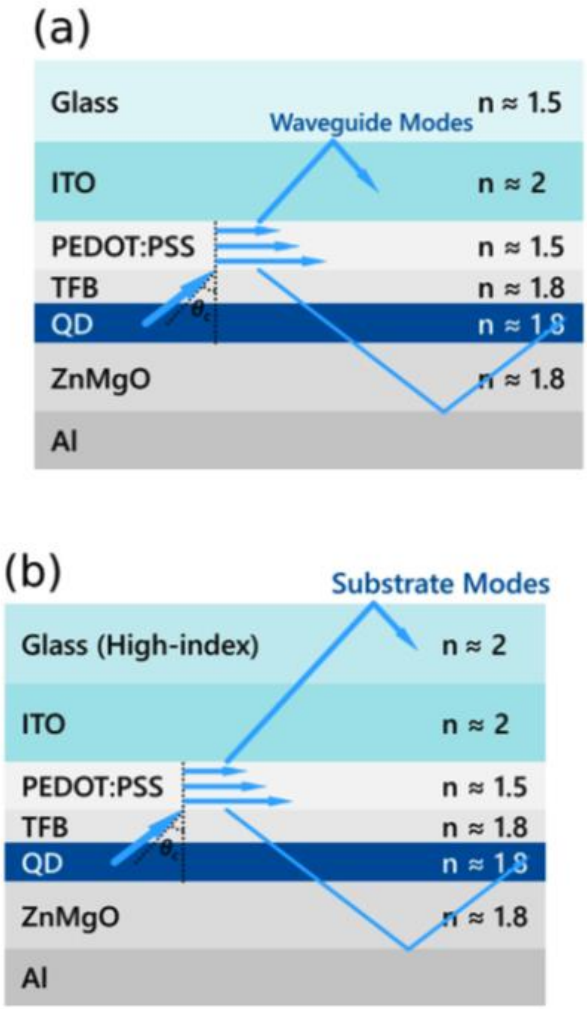

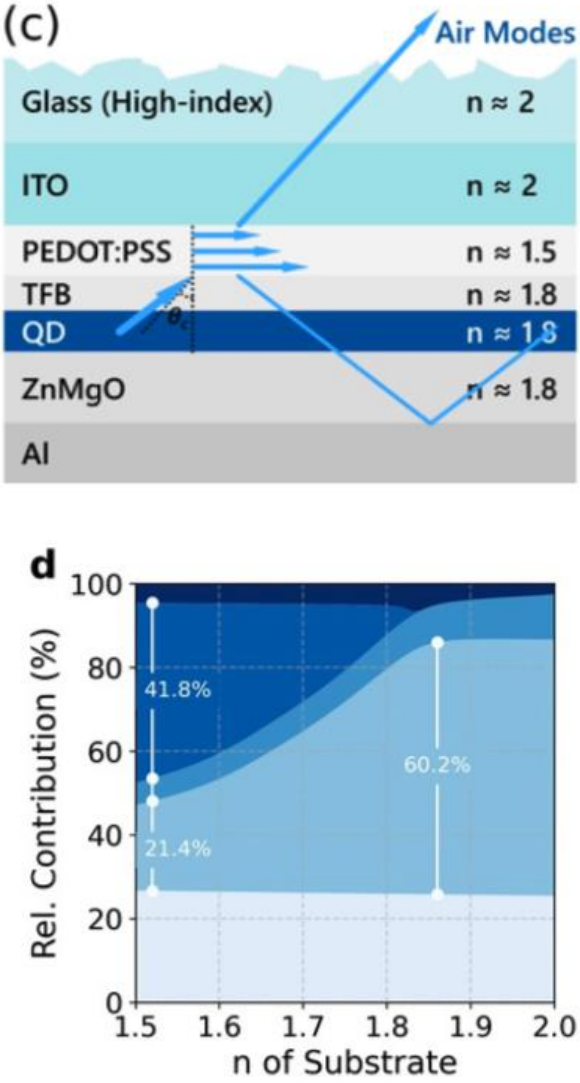

Figure 3.10 The procedure for extracting light using optical tunneling. (a) The presence of a thin HTL enhances optical tunneling, leading to the transfer of reflection to the anode-substrate interface. (b) A substrate with a high refractive index transforms waveguide modes into substrate modes. (c) The conversion of substrate modes to air modes is facilitated by the roughening of the surface. (d) Simulation for different n of substrate.

3.4.3 Surface roughening and air mode extraction

Photons in the substrate mode need to escape into the air by breaking the condition of total internal reflection. A random rough surface is prepared using sandpaper grinding (Figure 3.10c). In the surface roughening, we use different sizes of sandpaper for irregular grinding. Different sandpapers will produce different sizes of roughness. For example, 5000 mesh is the specification of the sandpaper we mainly use; it polishes the particle size to about 2-3 microns.

The performance of the device before and after roughness optimization has also been verified by experimental data, which can also be seen in the comparison of group A and group C below (Table 3.1), and the overall EQE of the device with only surface coarsening is about 10%. Its micro-nanostructures introduce light scattering effects, randomizing the propagation direction of the substrate mode, allowing some photons to escape when their incident angle is less than the critical angle. Experiments show that surface roughening can enhance the extraction efficiency of the substrate mode by 5%-20%.

3.5 Simulation modeling and parameter optimization

Based on the Finite-Difference Time-Domain (FDTD) method, a multi-physics coupling model of QLEDs (Figure 3.11) is established, covering material dispersion, microcavity resonance, and light field distribution. Key simulation parameters include:

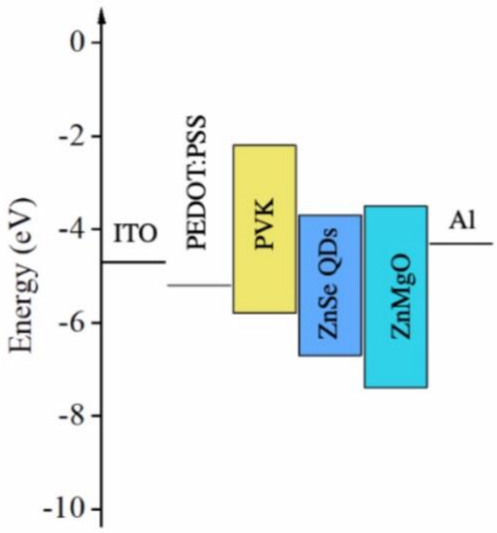

Figure 3.11 Device structure and energy band diagram

Refractive indices: Measured by ellipsometry for the QD layer (n=1.83@488 nm) and the ZnMgO ETL (n=1.80); Structural parameters: HTL thickness (10-60 nm), ITO Spacer thickness (0-200 nm), substrate refractive index (1.5-2.0); Light source model: Using the photoluminescence spectrum of ZnSe QDs as a dipole radiation source, considering anisotropic emission characteristics.

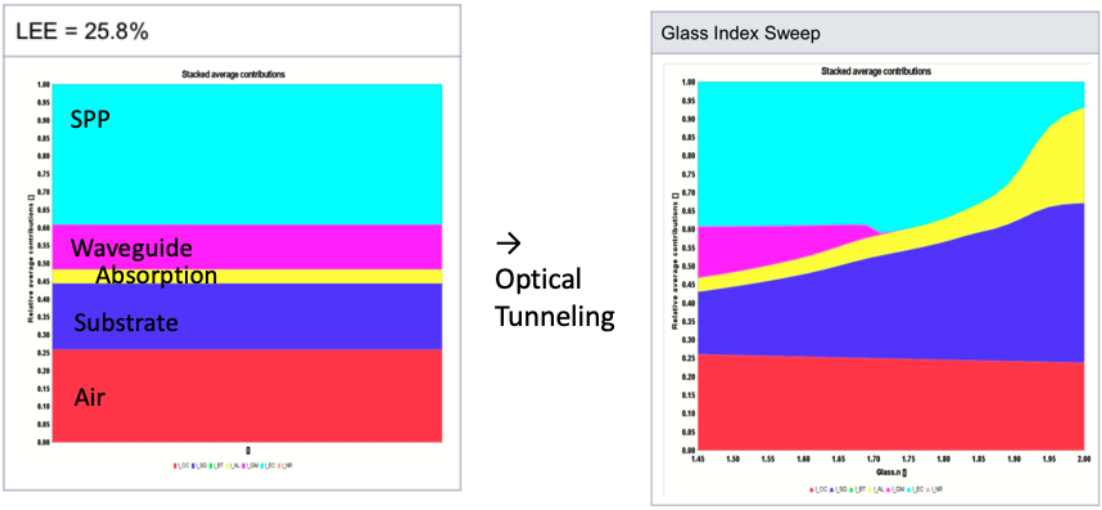

Figure 3.12 After the application of the optical tunneling scheme, the optical extraction mode changes

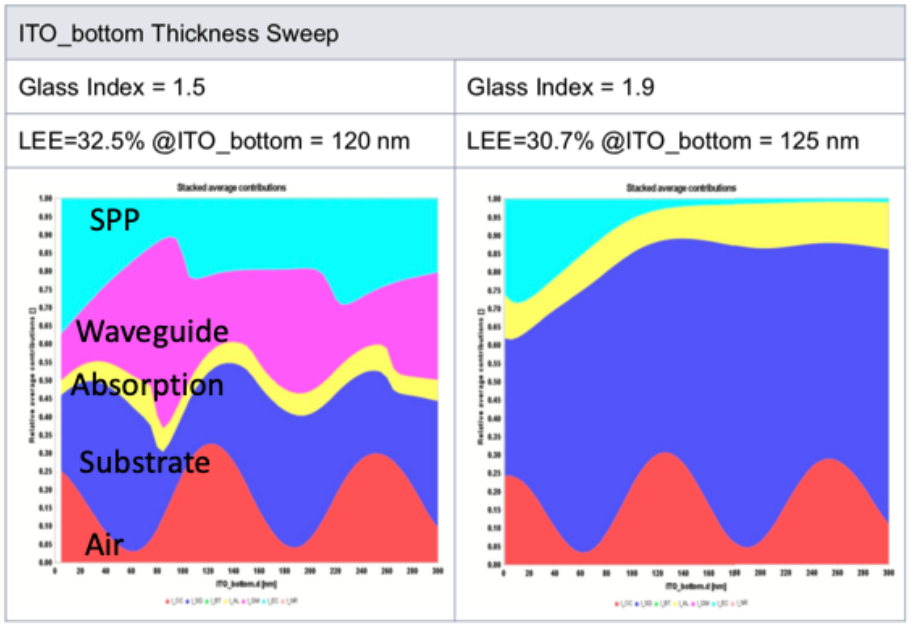

Figure 3.13 Changes in light extraction patterns under the integrated scheme

Optimization of ITO Spacer thickness: When the thickness is 120 nm, the air mode reaches 26.7%, while the waveguide mode maximizes (43%), forming an SPP-

waveguide-substrate energy transfer chain. Influence of substrate refractive index: A high refractive index substrate (n=1.9) increases the proportion of the substrate mode to 60%, providing ample extraction space for surface roughening. Trade-off of HTL thickness: An overly thick HTL (>60 nm) suppresses optical tunneling, leading to a decrease in the proportion of the substrate mode; while an overly thin HTL (<30 nm) may affect hole injection uniformity.

Our current approach involves the incorporation of ITO Spacer to enhance light radiation extraction in SPP modes, utilization of a high refractive index substrate for waveguide mode extraction, and ultimately the release of substrate mode through an external extraction structure such as surface roughing. The entire strategy is based on microcavity design rather than internal extraction methods, effectively addressing issues such as high cost and leakage current.

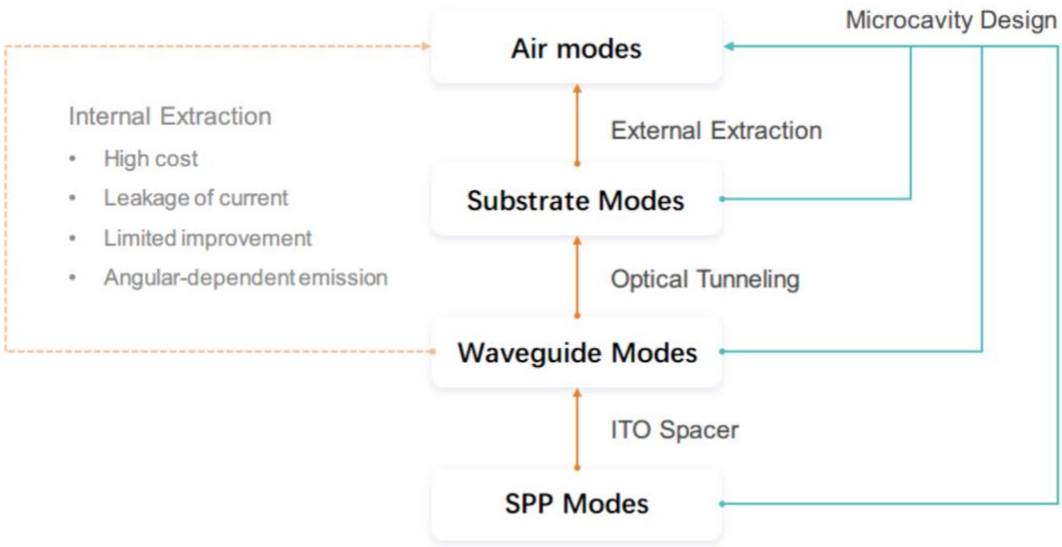

Figure 3.14 A comprehensive light extraction scheme route

3.6 Experimental verification

3.6.1 Device fabrication and structural design

To verify the effectiveness of the comprehensive strategy, five groups of blue ZnSe QLED devices were fabricated (structural parameters and experiment results are listed in Table 3.1), with the core variables including substrate refractive index, surface roughening treatment, and ITO Spacer thickness. The control group (Group A) employed a traditional structure: glass / ITO / PEDOT:PSS / PVK / ZnSe QDs / ZnMgO / Al; the experimental group (Group E) introduced a 120 nm ITO Spacer, a substrate with a refractive index of 1.9, and surface roughening.

Several groups of experiments were conducted to validate the effectiveness of the strategy. Group A is the Control group, which is fabricated using traditional device structures. On the basis of traditional device structures, Group B applied a high refractive index glass substrate, Group C applied an external light extraction method with substrate surface roughening, and Group D applied both high refractive index and surface roughened substrates. The E group applied a comprehensive light extraction strategy, including the addition of 120nm ITO Spacer and the use of high refractive index and surface roughening substrates.

After optimizing the combined light extraction strategy, the EQE was significantly improved, resulting in an increase in the EQE of blue ZnSe QLED from 6.64% to

18.50%. Approximately three times the EQE improvement provides a more universal optical optimization solution for cadmium-free and lead-free QLEDs.

Another set of experiments also proved that the ITO Spacer layer thickness obtained from simulation experiments is a better choice.

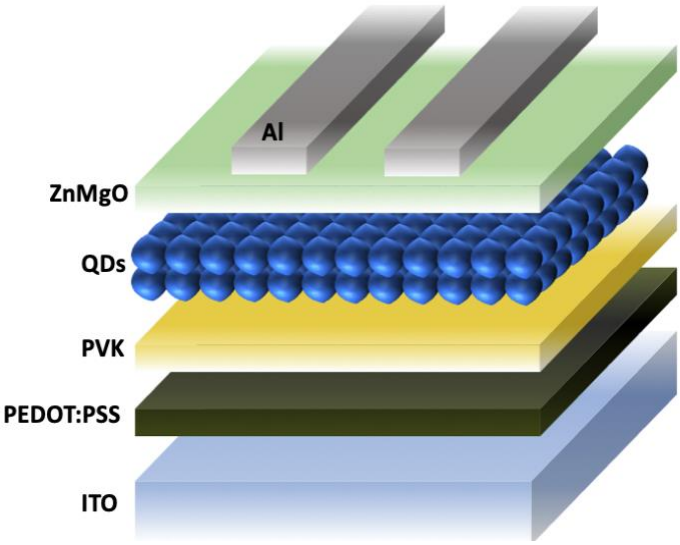

Figure 3.15 Schematic diagram of the device structure

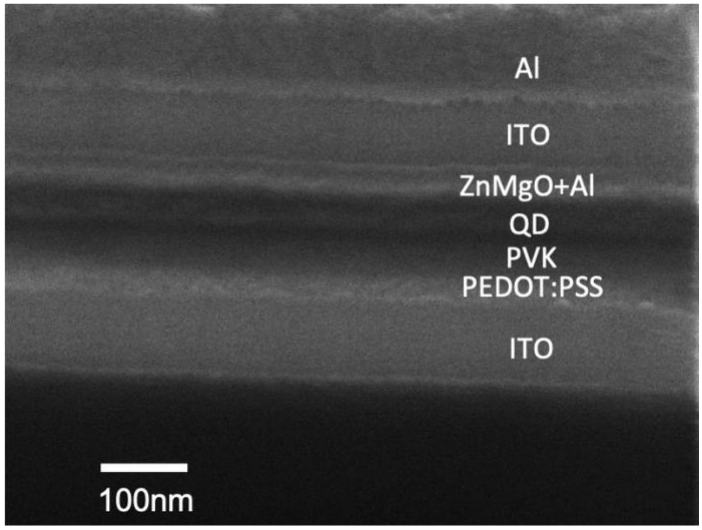

Figure 3.16 Cross-sectional view of the device after the optimization of the synthesis strategy

Table 3.1 Five groups of the QLEDs with their variables and EQE data.

Sample Group	Refractive index of the glass substrate	Substrate surface-roughening (Y/N)	Spacer thickness (nm)	Maximum EQE (%)	Average EQE (%)	Relative average EQE (%)
A (Control)	1.5	N	/	6.64	6.11	100
B	1.9	N	/	6.95	6.57	108
C	1.5	Y	/	7.65	7.46	122
D	1.9	Y	/	9.13	8.97	147
E	1.9	Y	120	18.50	17.00	278

3.6.2 Device performance testing

EQE Improvement: The maximum EQE of Group E reached 18.5%, a 278% increase compared to Group A (6.64%) (Figure 3.10c). This result is consistent with the simulation prediction (86.7% extractable photons), with discrepancies arising from interface defects and material non-uniformity in actual processes.

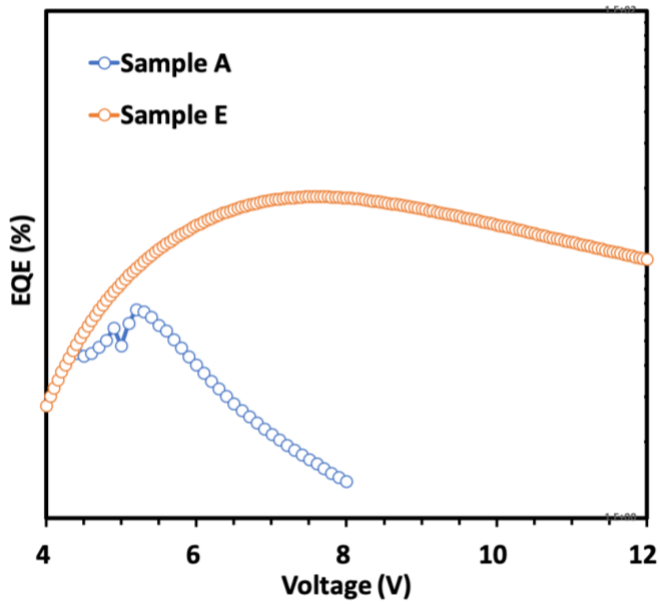

Figure 3.17 Comparison of the EQE of the two devices before and after optimization

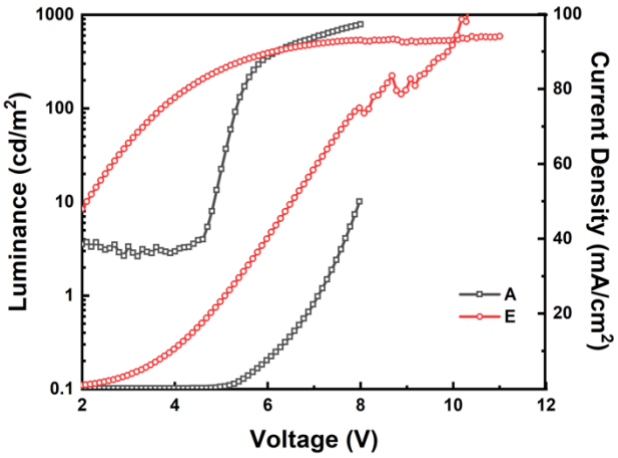

Figure 3.18 J-V-L of the two devices before and after optimization

Electrical Characteristics: The introduction of the ITO Spacer has almost no significant impact on the carrier injection balance, and there is little difference in

various parameters, indicating that the comprehensive strategy not only improves light extraction efficiency but also maintains the stability of electrical performance.

3.6.3 Limitations discussion

Although the EQE of Group E was significantly improved, there is still room for optimization in the following areas:

Limit of Substrate Refractive Index: Commercial high-refractive-index glass (n=1.9) has not yet reached the theoretical optimal value (n=2.0), resulting in some waveguide modes not being completely converted.

Surface Roughening Uniformity: SEM images show micrometer-scale undulations on the rough surface (Figure 3.19), which may cause local differences in light scattering efficiency.

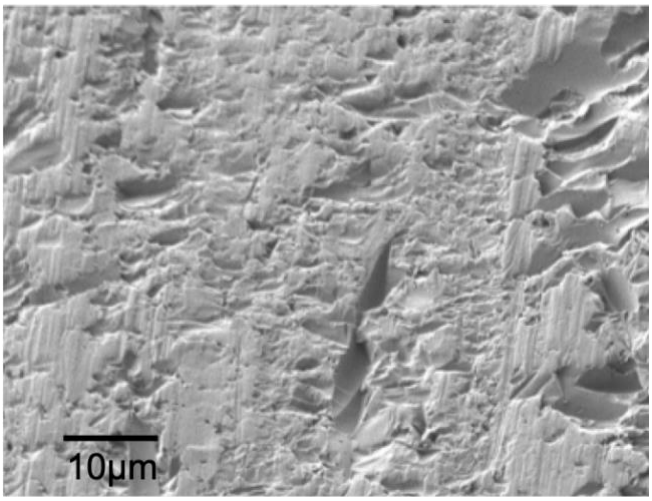

Figure 3.19 SEM image of the device substrate after surface roughening

Material Compatibility: The introduction of the ITO Spacer needs to align with the energy band of the QD layer to avoid introducing additional barriers.

3.7 Summary

Here, we propose a universal scheme that can be adapted to various core-shell ZnSe QD materials. (The light of the SPP mode, waveguide mode, and substrate mode in the device is gradually extracted into the air mode through the combination scheme, which includes ITO Spacer layers, optical tunneling, and external extraction methods.) Consequently, the devices based on the combination scheme show an impressive improvement EQE of nearly triple, from 6.64% to 18.5% at the wavelength of 470nm. Moreover, there is almost no loss in device current before and after using the scheme. This scheme can be applied to improve the device structure of ZnSe QDs with different core-shell structure, which can significantly bolster the development of cadmium-free and lead-free eco-friendly blue light QLEDs.

Chapter 4 Interface optimization: Enhanced hole injection by electric dipole layer

4.1 Introduction

Due to the significant insufficiency of hole injection in cadmium-free and lead-free QLEDs, particularly in the green and blue EMLs, it is necessary to further improve hole injection. In this chapter, the blue ZnSeTe QLEDs was used as the research example.

4.1.1 Research status of blue ZnSe QLEDs

The efficiency of ZnSe-based QLEDs is significantly influenced by the properties of the emitting material, specifically the QDs, as well as the structure of the QLED device itself. Binary ZnSe QDs possess a larger bandgap width of 2.7 eV, which endows them with the advantageous capability of emitting light in the ultraviolet and blue-violet regions[85]. This characteristic makes them particularly suitable for applications requiring these specific wavelengths.

However, achieving the desired blue light emission wavelength necessitates modifying the synthesis method to increase the size of the ZnSe core[52]. It is important to note that larger cores present a greater challenge in terms of effective surface passivation[86]. Incomplete passivation can lead to surface defects, which act as non-radiative recombination centers, thereby reducing the overall efficiency of the QLED device.

To address this challenge, researchers have explored the use of ZnTe, which has a smaller bandgap of 2.25 eV, to create ZnSeTe ternary QDs through alloying4. This approach allows for the fine-tuning of the QD properties, including the emission wavelength, and when combined with core-shell structures and surface ligand optimization, it results in highly efficient ZnSe QDs. These optimized QDs exhibit a higher PLQY and the desired blue light wavelength, which is crucial for the suppression of non-radiative recombination processes such as fluorescence resonance energy transfer and Auger recombination in QLEDs[52–54,87].

In conclusion, the efficiency of ZnSe QLEDs can be significantly enhanced by carefully controlling the synthesis process, including the size of the ZnSe core, the incorporation of ZnTe to form ternary ZnSeTe QDs, and the optimization of surface ligands. These strategies collectively contribute to the development of highly efficient QLEDs with improved color purity and brightness, paving the way for their broader application in display and lighting technologies.

4.1.2 Carrier behavior in blue ZnSeTe QLEDs

In the study of ZnSeTe QLEDs, a prominent issue lies in the imbalance of charge injection within the EML, which severely restricts the efficiency of QLEDs. In typical device structures, we observed that the commonly used HTL PVK presents a higher barrier between its HOMO energy level (-5.8 eV) and the valence band maximum (VBM) of ZnSeTe QDs, compared to the barrier between the ETL composed of ZnMgO nanoparticles (NPs) and the EML. This characteristic results in electrons being more easily injected into the EML than holes, leading to an imbalance in charge injection.

In the QD EML, the excess of electrons not only disrupts the charge balance but also significantly enhances non-radiative recombination processes, directly affecting the optoelectronic efficiency of the device. Additionally, defects present on the surface of ZnO or ZnMgO nanoparticles are an important factor contributing to the quenching of excitons at the interface between the EML and ETL[88–90]. These surface defects provide pathways for non-radiative recombination of excitons, further reducing the efficiency of QLEDs.

In summary, the issues of carrier transport in ZnSeTe QLEDs, particularly the imbalance of charge injection and exciton quenching, are key factors limiting their efficiency improvement. To overcome these obstacles, researchers need to explore new material systems and device structures to achieve more balanced charge injection and

reduce exciton quenching, thereby enhancing the overall performance of ZnSeTe QLEDs.

4.1.3 Development of interface optimizations

Three interfaces with energy barriers require optimization to improve hole injection: (1) the interface between ITO and HIL (PEDOT:PSS); (2) the interface between HIL and HTL (PVK); and (3) the interface between HTL and EML (QDs).

In ZnSeTe QLEDs, modifying the ETL to reduce surface defects and suppress electron transport is a method to balance carriers in the EML. Han et al. performed additional magnesium (Mg) treatment on conventional ZnMgO nanoparticles (NPs), resulting in the formation of a $Mg(OH)_2$ coating on the surface of the modified ZnMgO NPs (m-ZnMgO NPs). This coating improved the charge injection balance of the entire device by reducing the electron mobility of the ETL and suppressing luminescence quenching at the EML/ETL interface, playing a key role in enhancing device performance.[87]

Shen et al.[51] and Bao et al.[91] compared two commonly used HTLs, PVK and TFB, in their device structures. Their goal was to achieve higher hole injection and subsequently improve energy level alignment and injection balance within the device.

These studies emphasize the importance of material engineering and interface engineering in optimizing carrier balance and improving efficiency in QLEDs. By carefully designing and modifying the ETL and HTL, researchers can effectively

control charge injection and transport characteristics, thereby enhancing device performance.

In this study, we carried out a series of innovative improvements targeting the performance enhancement of ZnSeTe QLEDs. In particular, we introduced an electric dipole layer (EDL) with strong electron affinity, namely an ultra-thin F6-TCNNQ layer, which is crucial in the construction of QLEDs. The introduction of the F6-TCNNQ layer aims to create an internal electric field within the device through its strong electron affinity, which can effectively promote hole injection from the HTL to the EML.

Additionally, p-type material doping technology was also achieved through the EDL. This technology not only increases the interface carrier concentration between the HTL and EML but also effectively reduces the interface barrier. Through this method, the hole transport performance was significantly improved, leading to a more balanced carrier injection within the EML. This improvement is vital for enhancing the overall efficiency of QLEDs.

4.2 Interface engineering and energy level control mechanism

In the study of blue ZnSeTe QLEDs, enhancing the hole injection efficiency is vital for improving the overall device performance. However, in traditional QLEDs, the hole injection efficiency is often limited by the high energy barrier (Δ=0.9 eV) between

the polymer HTL PVK and the EML QDs, which hinders effective hole injection and, consequently, affects the device's luminous efficiency. Addressing this issue, this study proposes a new mechanism involving interface engineering and energy level manipulation, by introducing a strong electron acceptor, F6-TCNNQ, as an interface modification layer (as shown in Figure 1a), to optimize the hole injection process.

4.2.1 EDL design

Integrating an electric dipole layer (EDL) has emerged as an effective interface engineering technique to optimize charge injection in QLED devices, as schematically depicted in Figure.4.1. Such layers are generally composed of materials exhibiting strong electron affinity and a notably lower lowest unoccupied molecular orbital (LUMO) energy level, making them suitable for accepting electrons from neighboring hole transport materials. When interfaced with an HTL like PVK, the disparity in Fermi levels between the two materials initiates spontaneous electron movement from the HTL into the EDL. This results in the build-up of negative charge at the EDL side adjacent to the quantum dot EML, while corresponding positive charges accumulate at the HTL side of the interface. These oppositely charged carriers become confined across the interface, giving rise to localized dipoles. Importantly, the entire charge redistribution process occurs in the absence of an applied voltage. The resulting internal electric field, pointing from the HTL toward the EML, effectively assists the externally applied forward bias, enhancing hole transport. At the same time, the electron

extraction from the HTL increases hole population, which further boosts hole injection efficiency. Through this mechanism, the EDL significantly improves charge balance and facilitates more efficient radiative recombination in the EML.

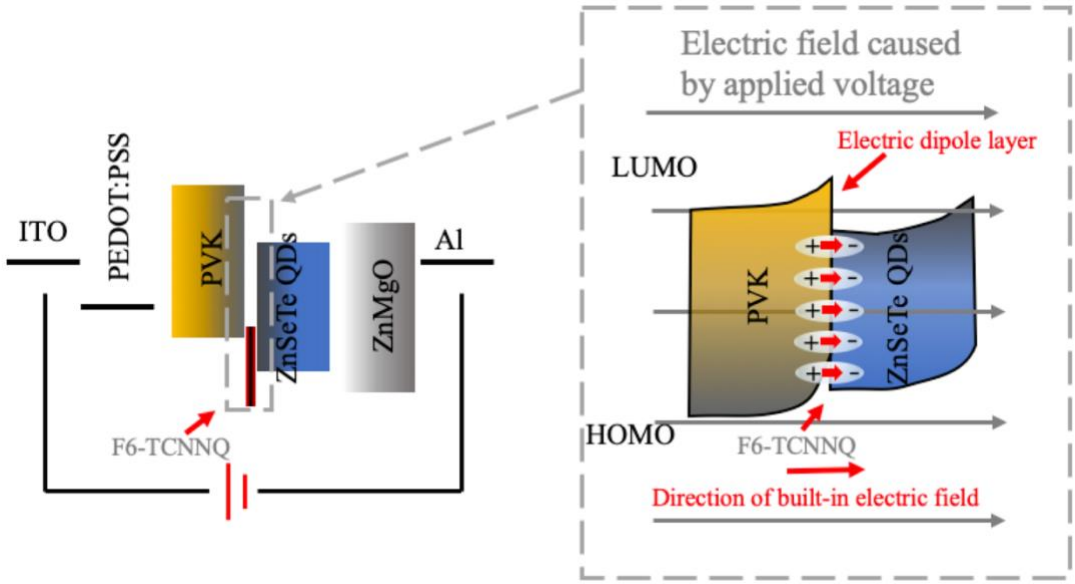

Figure 4.1 Schematic diagram of the interface modification of the EDL

F6-TCNNQ, a p-type material commonly utilized for interface modification in the perovskite field, features six highly electronegative fluorine atoms (as depicted in Figure 4.2). With a high electron affinity of approximately 5.60 eV, F6-TCNNQ functions as a potent electron acceptor molecule, surpassing other p-type materials, it is selected as the interface layer between HTL and EML to bolster hole injection.

The six fluorine atoms in the F6-TCNNQ molecule endow it with an ultra-high electron affinity (EA=5.6 eV) and a deep HOMO energy level (-7.5 eV). This

characteristic enables F6-TCNNQ to play key roles in interface modification. When brought into contact with HTLs such as PVK (with a Fermi level of −4.18 eV), the significant energy level mismatch ($\Delta E_F \approx 1.45$ eV) between the two materials enables spontaneous electron migration from PVK to F6-TCNNQ. This interfacial charge transfer leads to the development of an EDL at the interface. Thanks to its ability to accept electrons efficiently and to modulate interfacial energetics, F6-TCNNQ serves as a highly effective material for tuning the charge transport dynamics at the HTL/EML interface.

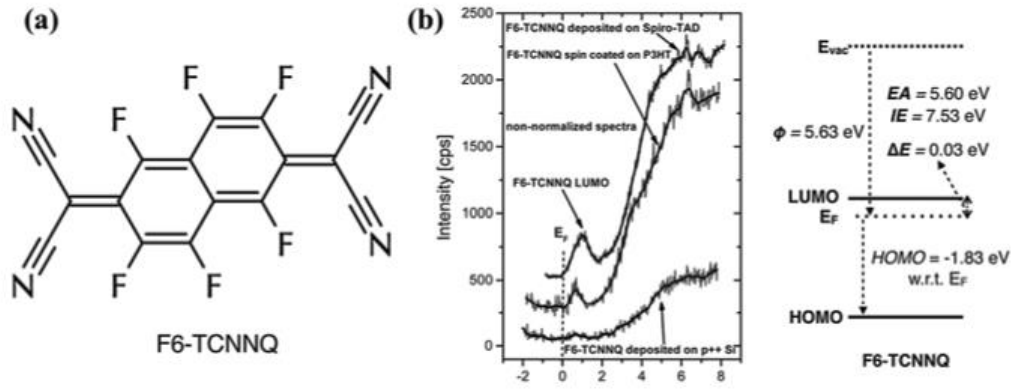

Figure 4.2 (a) Molecular structures and (b) energy level of F6-TCNNQ[92]

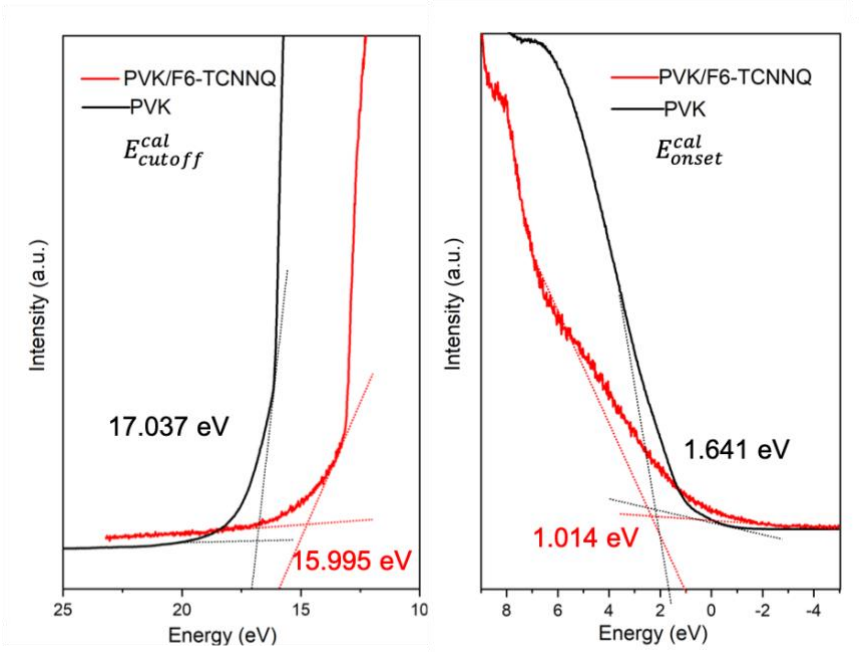

Figure 4.3 The UPS results for energy level of PVK with/without F6-TCNNQ

4.2.2 Adjust energy level

F6-TCNNQ can act as a p-type dopant for PVK/QD EML interface. It extracts electrons from the HOMO (-5.8 eV) of PVK, thereby effectively increasing the hole concentration. Ultraviolet photoelectron spectroscopy (UPS) data show that the HOMO energy level of PVK shifts downward by 0.4 eV to -6.2 eV after the introduction of F6-TCNNQ (as shown in Figure 4.3), indicating that F6-TCNNQ effectively enhances the hole injection efficiency at the interface.

Also note that UPS is commonly employed to determine the HOMO level or the valence band maximum (VBM) of thin-film materials. However, since UPS cannot directly access the LUMO level or the conduction band minimum (CBM), the optical

bandgap (Eg) is often used in combination with the HOMO level to estimate the LUMO position.

UPS measurements were systematically conducted to resolve the energy band characteristics of PVK HTL and PVK HTL with F6-TCNNQ introduction. Thin-film samples fabricated on Pt-coated SiO_2/Si substrates by spin coating underwent UPS analysis using a He Iα radiation source ($h\nu$ = 21.22 eV). Prior to measurements, *in situ* Fermi level calibration was performed using bare Pt/SiO_2/Si reference substrates, with Au standard verification establishing the binding energy baseline (E_F^{Au} = 0 eV).

All measurements were conducted at room temperature with ≤50 meV energy resolution, applying a -3 V sample bias during secondary electron cutoff (SEC) acquisition to enhance spectral contrast. As depicted in representative UPS spectra (Figure. 4.3), two critical spectral features were analyzed:

(1) HOMO onset energy E_{onset}^{cal}: Determined via linear extrapolation of the valence band leading edge;

(2) Secondary electron cutoff (SEC) E_{cutoff}^{cal}: Identified through low-kinetic-energy edge extrapolation.

Data processing:

① Fermi level calibration:

Measured Fermi edge offset relative to Au standard:

$$\Delta E_F = E_F^{sample} - E_F^{Au}$$

Calibrate all binding energy data by global translation:

$$E^{cal} = E^{raw} - \Delta E_F$$

Where E^{raw} is the original binding energy reading, E^{cal} is the calibration value (After calibration, the sample Fermi level is aligned with the instrument Fermi level $E_F^{sample} = 0$).

② Feature energy location extraction

Read critical locations from UPS spectra, as shown in Figure. 4.3,

SEC E_{cutoff}^{cal} and HOMO onset E_{onset}^{cal}.

③Calculation of energy level

The position of the vacuum energy level is determined by the cut-off edge:

$$E_{vac} = h\nu - E_{cutoff}^{cal} = 21.22 - E_{cutoff}^{cal};$$

The work function is defined as the difference between the vacuum level and the Fermi level:

$$\Phi = E_{vac} - E_F = E_{vac} \ (E_F = 0)$$

HOMO level (relative Fermi level):

$$E_{HOMO} = -E_{onset}^{cal}$$

④ Vacuum-level reference conversion ($E_{vac} = 0$)

In order to unify the interface energy level analysis, the vacuum energy level is taken as zero point.

Fermi level:

$$E_F^{(vac=0)} = 0 - \Phi = -E_{vac}$$

HOMO level:

$$E_{HOMO}^{(vac=0)} = -E_{onset}^{cal} - \Phi = -E_{onset}^{cal} - E_{vac}$$

Ionization energy verification:

$$IE = E_{vac} - E_{HOMO} = \Phi + |E_{HOMO}|$$

Table. 4.1 lists all raw and calibrated data along with the computed work functions and HOMO levels.

Table 4.1 UPS fitting results (Unit: eV)

PVK	ΔE_F	E_{onset}^{raw}	E_{cutoff}^{raw}	E_{onset}^{cal}	E_{cutoff}^{cal}
	−7	−5. 359	10. 037	1. 641	17. 037
	E_{vac}/Φ	$E_F^{(vac=0)}$	$E_{HOMO}^{(vac=0)}$	IE	
	4. 18	−4. 18	−5. 82	5. 82	
PVK with F6-TCNNQ	ΔE_F	E_{onset}^{raw}	E_{cutoff}^{raw}	E_{onset}^{cal}	E_{cutoff}^{cal}
	−2	−0. 986	13. 995	1. 014	15. 995
	E_{vac}/Φ	$E_F^{(vac=0)}$	$E_{HOMO}^{(vac=0)}$	IE	
	5. 23	−5. 23	−6. 24	6. 24	

Compared to the unmodified PVK film, the HOMO level exhibits a shift from –5.82 eV to –6.24 eV relative to the vacuum level (Evac), accompanied by an increase in work function from 4.18 eV to 5.23 eV. This movement of the Fermi level closer to

the HOMO edge reflects a strengthened p-type character of the HTL, arising from electron transfer to the F6-TCNNQ layer. Such interfacial tuning lowers the energetic barrier for hole injection and promotes more efficient hole transport into the EML.

This built-in electric field effectively reduces the hole injection barrier between PVK and the QDs, decreasing from the original 0.9 eV to 0.5 eV (Figure 4.4). This optimization of energy level alignment not only reduces the obstacles to hole injection but also helps achieve a more balanced carrier injection, enhancing the charge transport efficiency and luminous performance of the device.

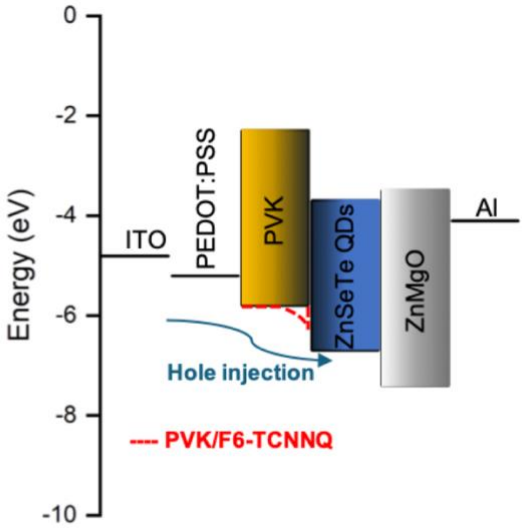

Figure 4.4 The change for energy level of PVK with/without F6-TCNNQ

Through the above mechanisms, the spin-coating process used in this study successfully formed an ultra-thin F6-TCNNQ layer (1.5 nm), showed in Figure 4.5, effectively reconstructing the interface between PVK and QDs, and significantly

improving the hole injection efficiency and overall performance of blue ZnSeTe QLEDs. This interface engineering and energy level control mechanism not only provides new ideas for optimizing the performance of QLEDs but also offers important theoretical basis and technical support for the application of cadmium-free and lead-free QD materials.

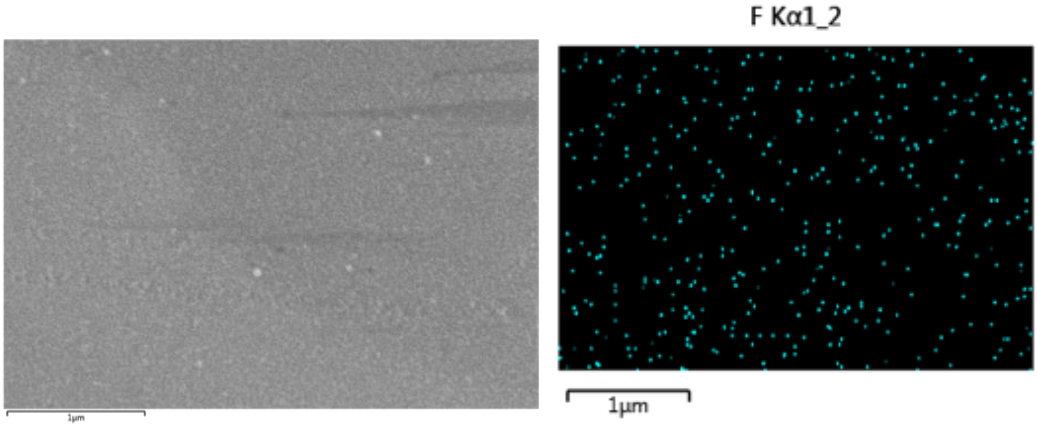

Figure 4.5 The SEM and EDS for F on PVK film to to demonstrate uniform surface doping of F6-TCNNQ

4.3 Carrier dynamics simulation verification

To thoroughly analyze the impact of F6-TCNNQ interface optimization on carrier dynamics, this study employed a combination of the drift-diffusion model and the Miller-Abrahams hopping theory to conduct a detailed simulation analysis of the electric field distribution, carrier transport dynamics, and recombination processes in QLEDs.

The drift-diffusion model is a continuous medium model that assumes the transport of carriers (electrons and holes) in semiconductors is primarily governed by a combination of drift motion caused by electric fields and diffusion motion caused by concentration gradients. This model calculates the electric field distribution and carrier concentrations by solving the Poisson equation and continuity equations, thereby simulating the current-voltage characteristics of devices. However, when dealing with low-dimensional structures such as QDs, the drift-diffusion model may not accurately describe the quantum effects and interface effects of carriers.[93,94]

The Miller-Abrahams hopping theory, on the other hand, is a model based on molecular orbitals that considers the quantum tunneling process of carriers as they hop between molecules. This theory describes the transport dynamics of carriers in amorphous or organic semiconductors by calculating the probabilities of carrier transport between different energy levels, as well as the associated activation energies and transport distances. The Miller-Abrahams hopping theory particularly provides a more precise description when dealing with transport phenomena related to interfaces and defect states.[95,96]

In the Miller-Abrahams hopping theory, the hole transport frequency (ν) is a key parameter describing the transport behavior of carriers between interfaces, and it is expressed as follows:

$$\nu = \nu_0 exp(-\frac{E_a}{k_B T})$$

where ν_0 is the attempt frequency, E_a is the activation energy, k_B is the Boltzmann constant, and T is the absolute temperature. The simulation results show that due to the introduction of the F6-TCNNQ interface modification layer, the activation energy for holes is reduced from 0.9 eV to 0.5 eV, leading to a significant increase in the hole transport frequency and thereby enhancing the hole injection efficiency.

4.3.1 Built-in electric field enhancement

The electric fields of QLEDs in the simulation experiments are as follows. In the F6-TCNNQ interface region, the transfer of electrons from PVK to F6-TCNNQ induces a strong built-in electric field of up to 2.5×10^3 V/cm (Figure 4.6), directed towards PVK→QDs. This enhancement of the built-in electric field effectively promotes the tunneling effect of holes. According to the Miller-Abrahams hopping transport model, the activation energy of holes is reduced from 0.9 eV at the original interface to 0.5 eV, significantly improving the mobility of holes and their injection efficiency at the interface.

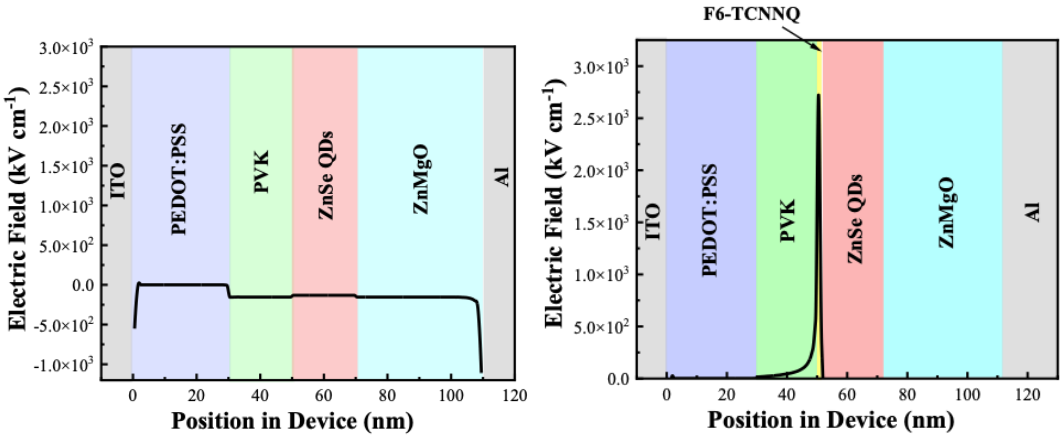

Figure 4.6 Electric field of simulation QLEDs without/with F6-TCNN

4.3.2 Hole injection improvement

Simulation data indicate that the hole current density in EML significantly increases from 12 mA/cm² (unmodified interface) to 10^{10} mA/cm² (Figure 4.7), and the carrier balance factor also increases from 0.3 to 0.8, indicating a more balanced injection of holes and electrons, approaching the ideal bipolar injection state. This improvement in injection efficiency is attributed to the regulation of the energy level structure by the interface modification layer, thereby reducing the hole injection barrier and enhancing the hole injection capability.

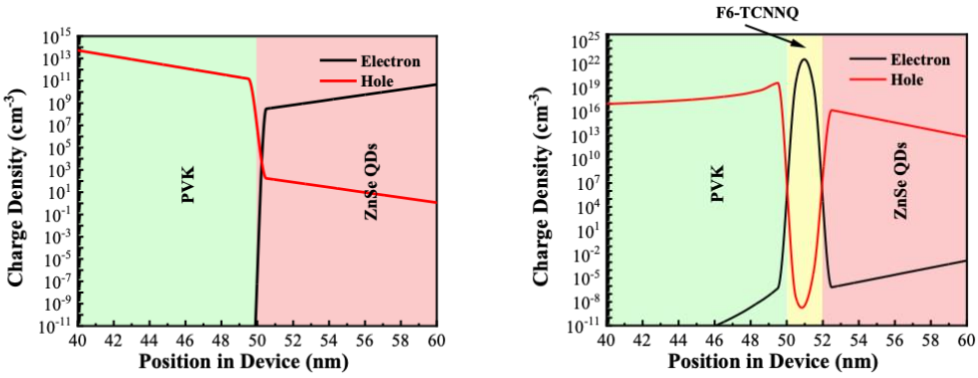

Figure 4.7 Charge density of simulation QLEDs without/with F6-TCNNQ

4.3.3 Recombination efficiency optimization

The improved radiative recombination efficiency manifests clearly in both the spatial pattern and intensity of recombination events, as depicted in Figure 4.8. Upon introduction of F6-TCNNQ, the distribution of recombination within the QD EML undergoes notable changes. In the reference device lacking this interfacial modifier, recombination is concentrated near the PVK/QDs interface, with a peak rate of approximately 5.5×10^{20} cm^{-3} s^{-1}, suggesting an imbalance in carrier injection—specifically, insufficient hole supply. In contrast, the device incorporating F6-TCNNQ displays two pronounced recombination zones, situated near both the PVK/QDs and QDs/ZnMgO interfaces. The peak recombination rate increases significantly to 1.62×10^{21} cm^{-3} s^{-1}, indicating nearly a threefold enhancement. This bilaterally distributed recombination pattern reflects a marked improvement in charge balance throughout the emissive region. The observed shift in recombination zone along with

the intensified recombination rate affirms the role of F6-TCNNQ in facilitating more efficient radiative processes, thereby contributing to the overall advancement in device performance

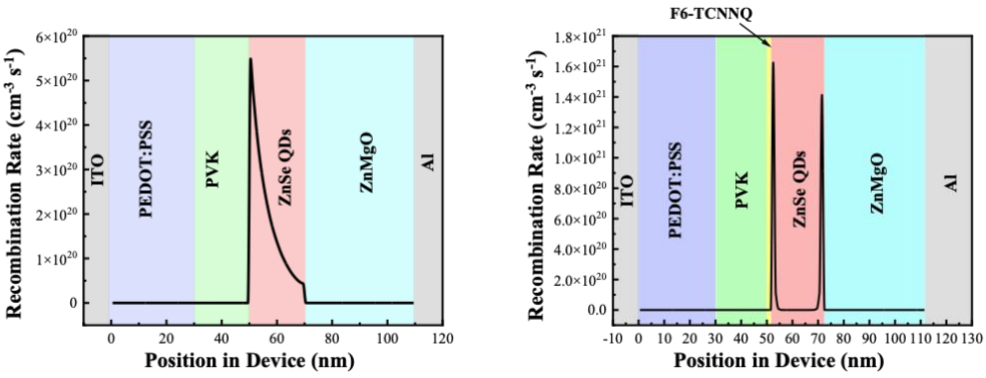

Figure 4.8 Recombination rate of simulation QLEDs without/with F6-TCNNQ

4.4 Experimental performance and mechanism

4.4.1 Optical properties of the devices

The devices in the simulation experiments were fabricated and tested to verify the efficiency improvement after adding F6-TCNNQ doping. The structure of devices is ITO / PEDOT:PSS / PVK (with/without F6-TCNNQ) / ZnSeTe QDs / ZnMgO NPs / Al. To further analyze the structural characteristics of the device, we utilized HIM to obtain detailed cross-sectional images of the device. The HIM can boast a high spatial resolution capable of clearly revealing the layered structure and interface features within the device.

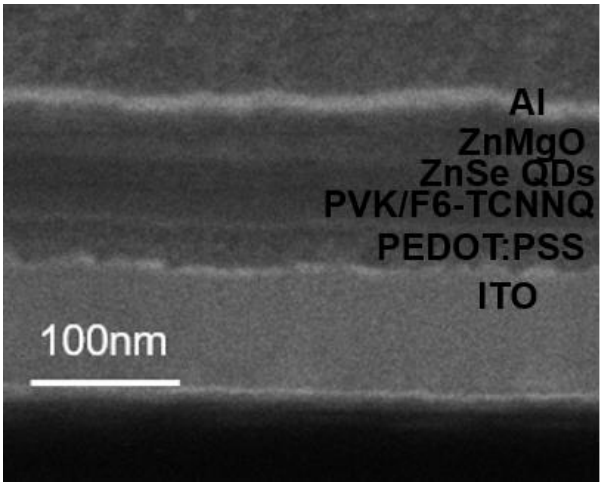

Figure 4.9 Cross-section image of the QLEDs

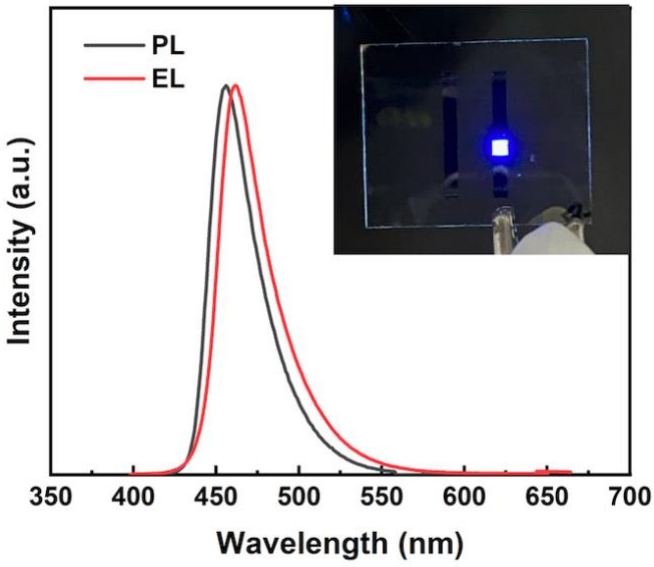

Figure 4.10 PL and EL spectra of the QLEDs. The inset shows an emitting QLED.

4.4.2 Electrical performance of the devices

To evaluate the influence of F6-TCNNQ on device performance, a comparative analysis was conducted between the reference QLEDs (without F6-TCNNQ) and those modified with F6-TCNNQ. As depicted in Figure. 4.11, the introduction of F6-TCNNQ leads to a notable enhancement in the EQE, with the maximum EQE increasing from 7.44% in the control devices to 12.71% in the modified ones. This corresponds to an improvement of approximately 71%, highlighting the effectiveness of F6-TCNNQ in boosting device efficiency.

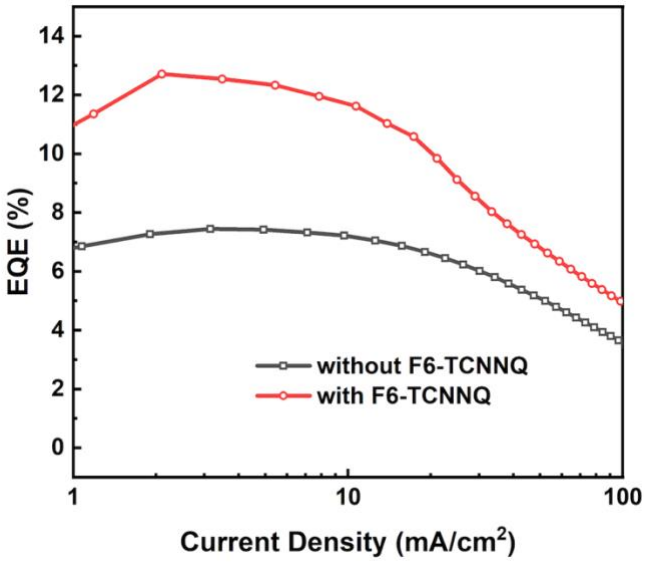

Figure 4.11 EQE of the QLEDs.

Further insight into the electrical and optical performance was obtained through current density–voltage–luminance (J-V-L) measurements, as shown in Figure. 4.12. The data indicate that both the control and F6-TCNNQ-treated QLEDs exhibit nearly identical turn-on voltages, each around 3 V. This observation suggests that the

incorporation of F6-TCNNQ does not significantly alter the charge injection threshold or compromise the initial operating voltage.

However, across the entire operational voltage window, devices incorporating F6-TCNNQ consistently demonstrate superior current densities and enhanced luminance levels compared to the control group. A clear example is observed at an applied bias of 8 V, where the luminance increases markedly from 1637 cd/m^2 (for the control device) to 2885 cd/m^2 in the F6-TCNNQ-based device. This represents a substantial enhancement of approximately 76%. Collectively, these improvements are indicative of more efficient carrier injection dynamics and enhanced radiative recombination processes, both of which contribute to the overall performance gains observed in the F6-TCNNQ-modified QLEDs.

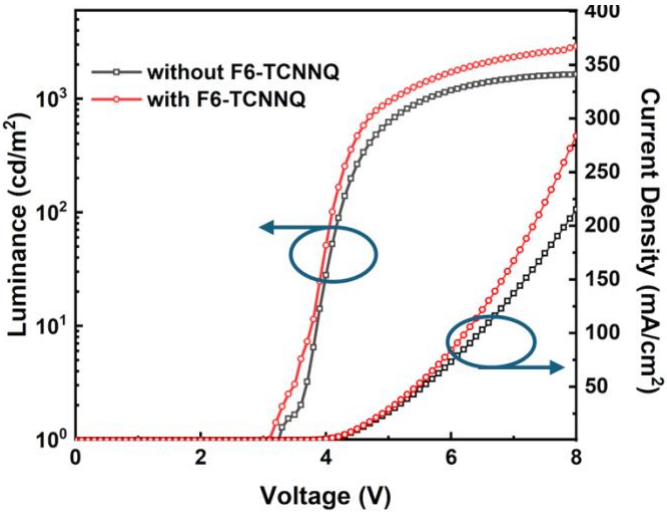

Figure 4.12 Current density-voltage-luminance of the QLEDs.

Additionally, after the introduction of the F6-TCNNQ interface layer, the turn-on voltage of the QLED increased a little. This change may be due to the dynamic adjustment of the hole injection barrier caused by interface energy level reconstruction. UPS test results show that the work function of F6-TCNNQ is approximately 5.6 eV, which is higher than the HOMO energy level of HIL PEDOT:PSS (-5.2 eV), thereby increasing the hole injection barrier from PEDOT:PSS to PVK, increasing the difficulty of hole injection, and leading to an increase in the turn-on voltage. Furthermore, the addition of F6-TCNNQ may have reduced the conductivity of the PVK layer, possibly due to a decrease in hole mobility caused by excessive oxidation. To reduce the turn-on voltage, future research could consider introducing gradient doping or a transition layer (such as MoO_3) to optimize energy level matching and minimize the injection barrier at each interface.

4.5 Summary

By introducing F6-TCNNQ into the interface of HTL/EML, the comprehensive performance indicators of the QLED device were significantly improved. The doping effect of F6-TCNNQ is mainly reflected in the following aspects:

Firstly, in terms of energy level regulation and carrier injection, the strong electronegativity of F6-TCNNQ leads to the formation of an electric dipole at the interface, resulting in an built-in electric field at the HTL/QD interface. This built-in

electric field effectively lowers the hole injection barrier, making it easier for holes to be injected from the HTL into the QD EML, significantly improving the hole injection efficiency.

Secondly, in terms of charge transport performance improvement, the doping of F6-TCNNQ optimizes the charge transport characteristics in the HTL. It adjusts the energy level of the HTL, reducing the interface barrier during hole transport, thereby increasing the hole mobility. Additionally, its deep energy level also acts as an electron barrier at the hole injection end of the EML, effectively improving the carrier radiative recombination in the EML.

In summary, the experimental results demonstrate that through interface engineering to optimize the HTL/EML interface, the EQE of ZnSeTe QLEDs has been significantly improved, increasing from 7.44% to 12.71%.

The increase of efficiency not only validates the effectiveness of the strategies we employed but also deepens our understanding of carrier behavior. The study of carrier behavior within devices is crucial as it directly affects charge balance, injection efficiency, and radiative recombination efficiency, being a key factor in enhancing the performance of QLEDs.

Our work not only provides a new pathway for enhancing the efficiency of QLEDs but also lays a solid foundation for further research and development in cadmium-free and lead-free QD materials and their device designs. Looking forward, the research on cadmium-free and lead-free materials will place greater emphasis on environmental

friendliness and sustainability. We anticipate that through continuous optimization of carrier transport and device structure, we can further improve the performance of QLEDs, promoting the widespread application of cadmium-free and lead-free QD materials in display technology, and contributing new momentum to the development of environmentally friendly electronic products

Chapter 5 Electronic leakage mechanism and its suppression strategy

5.1 Research background and core issues

Indium phosphide (InP) QDs are considered ideal alternatives to cadmium-based QDs due to their environmental friendliness and superior optoelectronic properties. However, the EQE of green InP QLEDs has been persistently limited by carrier imbalance. Early research has indicated that although optimization of the QD shell structure, such as the substitution of ZnS with a ZnSeS alloy shell, can mitigate lattice mismatch and suppress parasitic luminescence, non-radiative recombination processes in the HTL still significantly degrade device performance[97]. Theoretical analysis suggests that electron leakage from the QD layer to the anode is a major contributor to efficiency loss, yet its microscopic mechanism remains unclear, particularly lacking a systematic investigation into the unique band structure of the InP system[98].

This study focuses on elucidating the electron leakage pathways in green InP QLEDs and proposes the use of interface engineering to regulate the balance of carrier transport. Based on the principle of Fermi level alignment and multi-physics simulations, it reveals the critical role of the ITO anode's work function and the band

mismatch with InP QDs. By incorporating an ultra-thin lithium fluoride (LiF) interfacial layer, electron leakage is suppressed, and hole injection is enhanced, ultimately leading to a significant improvement in device efficiency.

5.1.1 Simulation

Simulation of carrier distribution was meticulously carried out using the advanced COMSOL Multiphysics software, which employed a set of coupled equations to accurately model the behavior of charge carriers. Specifically, Poisson's equation was used to describe the electrostatic potential distribution throughout the system, taking into account the spatial distribution of fixed charges and the influence of free charge carriers on the electric field. This equation ensures that the electric field is irrotational and is related to the charge density by Gauss's law.

In conjunction with Poisson's equation, the continuity equation was applied to govern the conservation of charge. This equation states that the rate of change of charge density in a given volume is equal to the divergence of the current density, which accounts for the generation, recombination, and flow of charge carriers within the material. The continuity equation, therefore, provides a crucial link between the charge dynamics and the transport phenomena occurring in the semiconductor.

The drift-diffusion equation was further utilized to describe the variation in carrier concentration, incorporating both the drift of carriers due to the electric field and their random thermal motion, or diffusion. For the energy band data in the simulations, well-

established references from the literatures were referenced, and the Fermi level data was meticulously obtained through ultraviolet photoelectron spectroscopy (UPS) measurements.

Electrical simulations focusing on the recombination rate were conducted using the Setfos 4.6 software, which incorporated both constant and field-dependent electron and hole mobilities, modeled in accordance with the Poole–Frenkel effect. The HOMO and LUMO values selected for the research are detailed in Figure. 5.3(a). The boundary conditions for charge carrier densities at the electrodes were meticulously set to ensure Fermi level alignment under thermal equilibrium conditions, reflecting the balance between the chemical potential of electrons and holes. The generation of excitons was confined to the EML, following the Langevin recombination model, which describes the probabilistic nature of carrier interactions leading to recombination. This comprehensive approach in the simulations encapsulates the intricate interplay between the electrostatics, charge conservation, and carrier transport phenomena in semiconductor devices.

5.1.2 Materials

The PEDOT:PSS (Clevios™ P VP Al 4083) used in this study was procured from Xi'an p-OLED Ltd. and applied without any additional dilution. PVK was purchased from Lumtec Ltd. and dissolved in chlorobenzene at a concentration of 8 $mg \cdot mL^{-1}$. Green InP/ZnS QDs were acquired from Fullnano Ltd. and suspended in octane at a

concentration of 10 mg·mL^{-1}. The green InP/ZnS QDs had a diameter of 5.0 ± 0.2 nm, with TOP/OA as ligands. ZnMgO nano particles were sourced from Mesolight Ltd. and dispersed in ethanol at a concentration of 20 mg·mL^{-1}. The LiF was also obtained from Lumtec Ltd.

5.1.3 Device fabrication

QLEDs were fabricated with a layered structure consisting of: indium tin oxide (ITO) / lithium fluoride (LiF) with varying thicknesses (0, 0.5, 0.75, 1.0, 1.25, 1.5, 1.75, and 2.0 nm)/ :PSS (25 nm)/ PVK (30 nm) / InP QDs (25 nm) / zic magnesium oxide (ZnMgO) (30 nm)/aluminum (Al) (100 nm). For photoluminescence (PL) comparison experiments, half-devices were assembled using the configurations, ensuring that the layer thicknesses matched those of the complete QLED devices. Additionally, hole-only devices (HODs) were manufactured with the structure ITO / LiF (0, 0.5, 1.0, 1.5, and 2.0 nm) / PEDOT:PSS (25 nm) / PVK (30 nm) / green InP / ZnS QDs (25 nm) / 1,3,5-tris (4-carbazolyl) benzene (TCTA) (10 nm) / 4,4'-bis [N-(1-naphthyl)-N-phenylamino] biphenyl (NPB) (10 nm) / 4,4',4"-tris (carbazol-9-yl) triphenylamine (HAT-CN) (15 nm) / Al (100 nm). Prior to assembly, the patterned ITO substrates underwent a cleaning and plasma treatment process to ensure optimal surface conditions. All functional layers, excluding LiF, were spin-coated at a speed of 3000 rpm for 45 seconds, followed by thermal annealing to improve film quality. The LiF and Al electrodes were then deposited using thermal evaporation at rates of 0.1 nm·s^{-1}

and 0.2 nm·s^{-1}, respectively, under a high vacuum environment of 5×10^-4 Pa to ensure uniform and controllable film thicknesses.

5.1.4 Characteristic

For the simulations and experiments, the energy levels were determined through ultraviolet photoelectron spectroscopy (UPS) measurements conducted on thin films using a PHI 5000 Versaprobe III system. A bias voltage of -3 V was applied during these measurements to accurately capture the electronic properties of the materials. The UPS spectra were interpreted to derive the energy levels by analyzing the binding energies of the electrons in the valence band. The cutoff energy in the spectra, which corresponds to the highest binding energy measurable, was used to estimate the work function of the material, a critical parameter for understanding electron injection and transport. Additionally, the alignment of the energy levels within the material's band structure was assessed by comparing the measured ionization potential with the electron affinity of adjacent layers, which is essential for evaluating charge injection and device performance. The shape and intensity of the UPS peaks also provided insights into the film's composition and quality. To obtain these results, the raw UPS spectra were processed to remove noise, normalized, and peak fitting techniques were applied to determine the positions and widths of the spectral features. The luminescent area of the devices was 2 mm x 2 mm. The PLQY and PL spectra were obtained using an absolute PLQY spectrometer with a 365 nm excitation wavelength. The devices were considered

Lambertian emitters, and current density-voltage-luminance (J-V-L) curves were measured using a Keithley 2614B source measurement unit in conjunction with a PIN25D silicon photodiode. All measurements were conducted at room temperature.

5.2 Theoretical modeling and simulation verification of electron leakage mechanisms

5.2.1 Band mismatch and Schottky barrier effect

The n-type semiconductor characteristics of InP QDs place their Fermi level ($E_f \approx$ -3.7 eV) close to the conduction band minimum (CBM, -3.5 eV), while the work function of the traditional ITO anode (WF ≈ 4.8 eV) is significantly higher (Figure 5.1a). According to the metal-semiconductor contact theory, a Schottky barrier (height $\Delta\Phi \approx 1.1$ eV) is formed at the interface, leading to the escape of conduction band electrons from the QDs to the ITO via thermal emission or tunneling effects[99]. This process is limited by the balance of the built-in electric field under no bias. However, under forward bias, the external electric field weakens the built-in barrier, resulting in an exponential increase in the electron leakage rate[100].

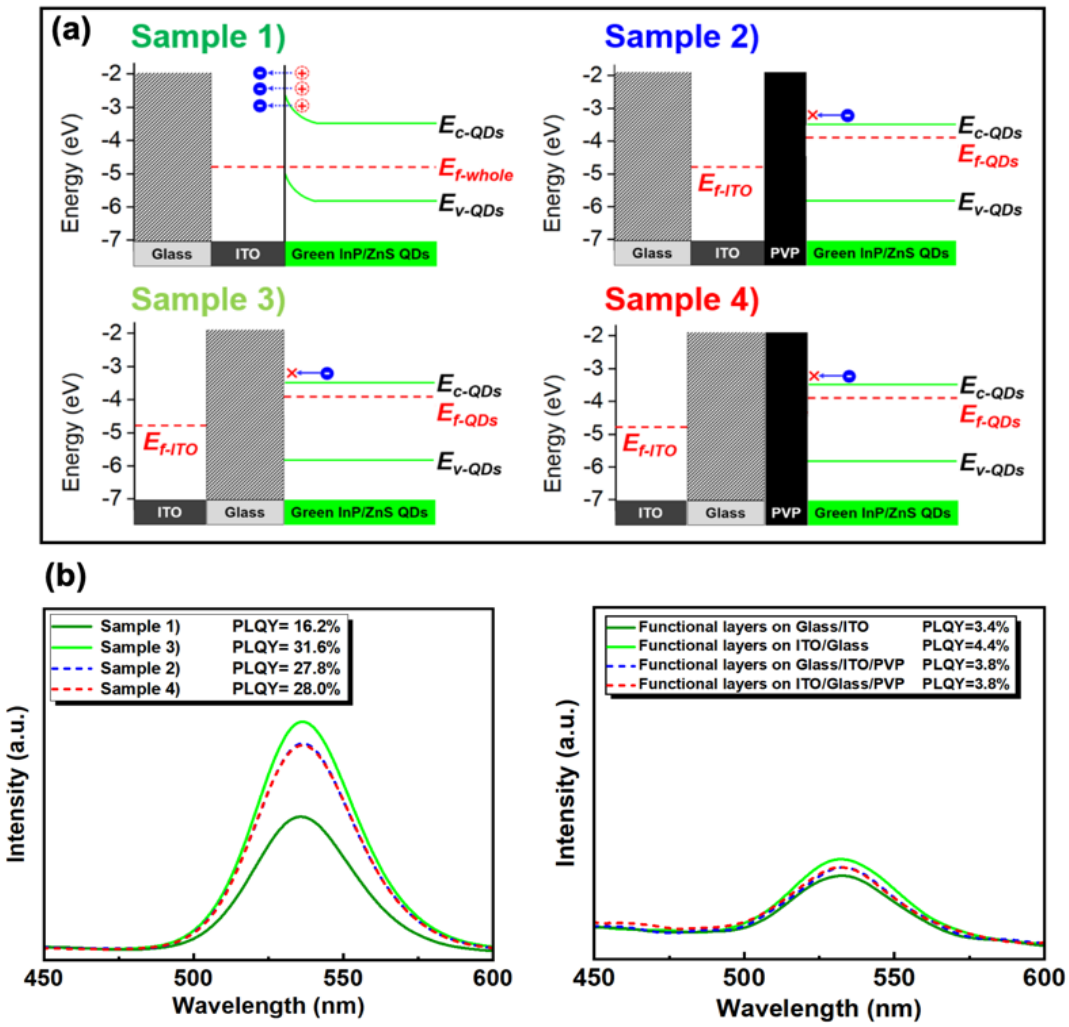

Figure 5.1 (a) Schematic of the Schottky contact band alignment at the ITO/InP QDs interface, green InP/ZnS QDs films deposited on four substrates (b) Photoluminescence (PL) spectra of these various samples and functional layers on four substrates.

5.2.2 Multi-scale simulation of carrier transport

Based on the COMSOL Multiphysics platform, a two-dimensional device model incorporating Poisson's equation and the continuity equation was constructed to

simulate the carrier distribution in different functional layers (Figure 5.2). The key findings are as follows.

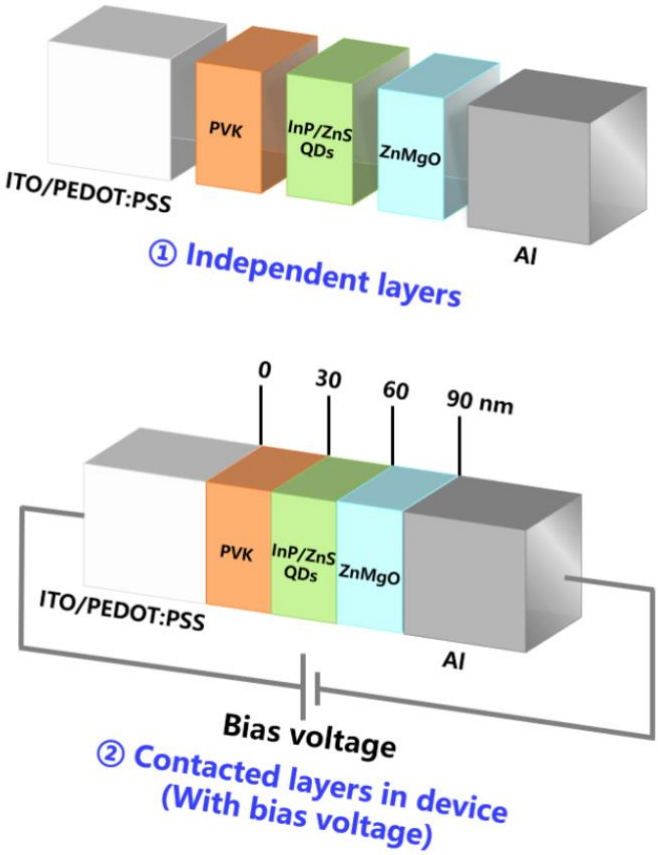

Figure 5.2 Device model structures in different functional layers

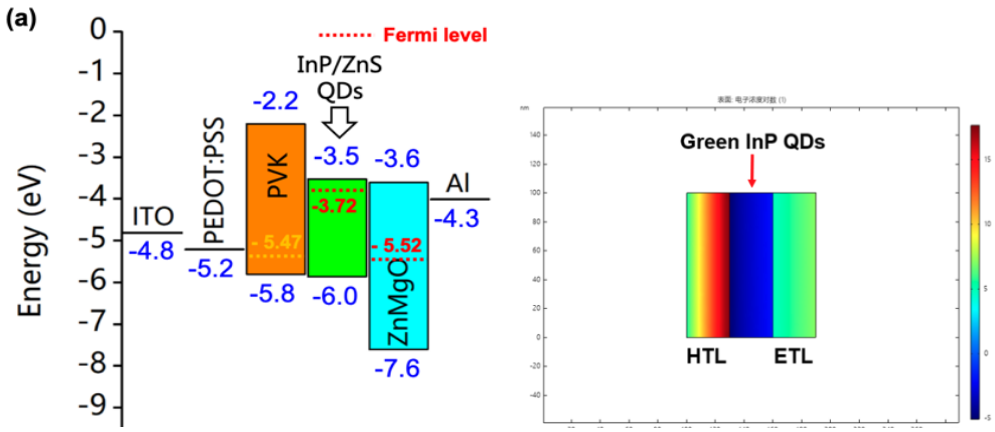

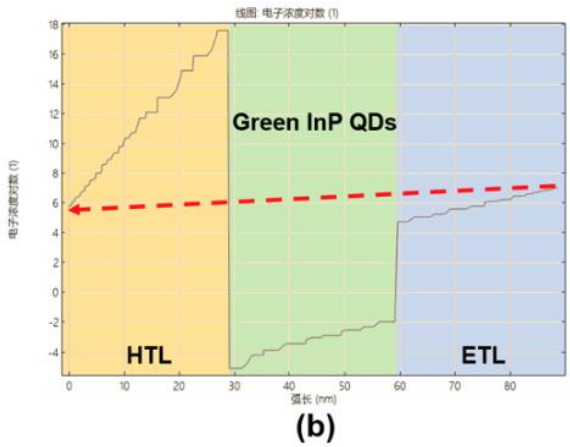

Figure 5.3 (a) The energy bands and Fermi levels with electron concentration distribution of green InP QLEDs (b) Simulated distribution curve of electron concentration across the device.

Analysis of independent functional layers: the intrinsic electron concentrations of the HTL PVK and the ETL ZnMgO are 1.2×10^{12} cm^{-3} and 3.5×10^{15} cm^{-3}, respectively, while the initial concentration of the InP QDs layer is as high as 2.8×10^{18} cm^{-3}.

Full Device Integration Simulation: Upon stacking the functional layers, the electron concentration in the InP QDs layer drops sharply to 4.6×10^{13} cm^{-3} (a reduction of five orders of magnitude), indicating continuous electron leakage from the QDs layer to the HTL side. Compared with the simulation results of CdSe QLEDs (where the QDs layer concentration remains at 1.7×10^{17} cm^{-3}), this confirms that the InP system experiences more significant electron loss due to its shallow Fermi level (Figure 5.4).

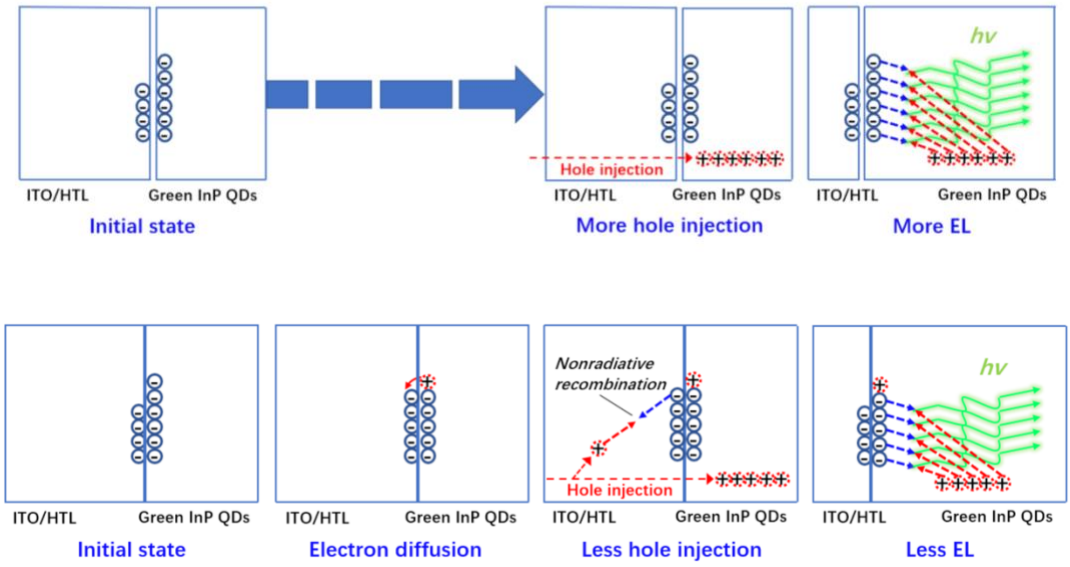

Figure 5.4 The process of electron diffusion occurs with/without contact.

Bias Dependence: When a forward bias of 5 V is applied, electron injection at the ZnMgO/Al interface is enhanced (with a peak concentration of 6.2×10^{16} cm^{-3}), but electrons in the QDs layer still flow towards the ITO side through a diffusion-migration coupling mechanism, forming an asymmetric carrier distribution (Figure 5.5).

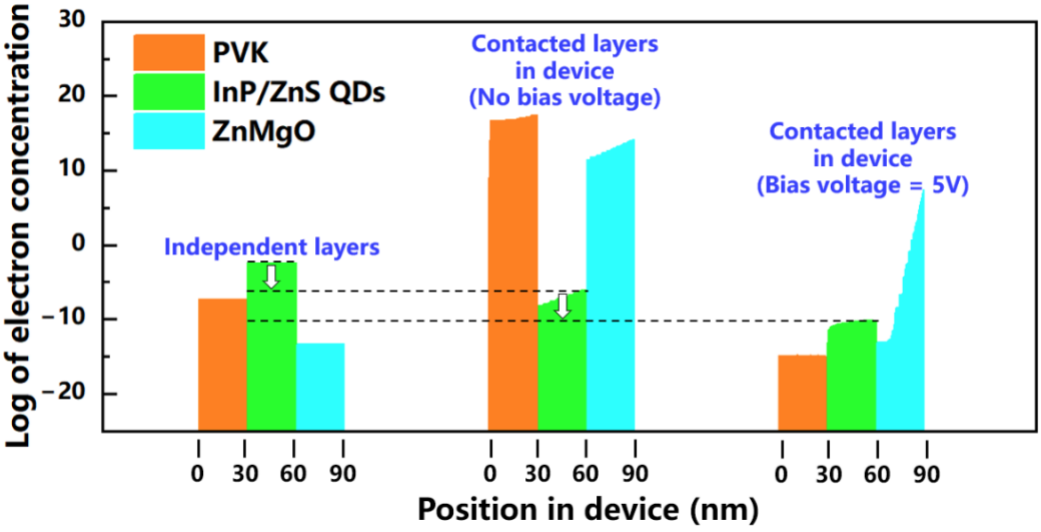

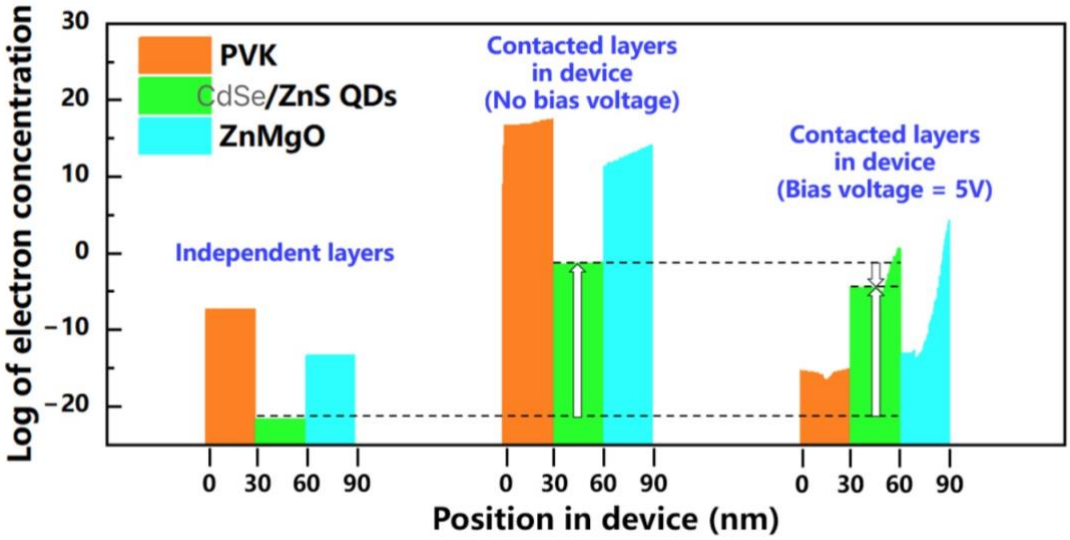

Figure 5.5 Numerical simulations of electron concentration distribution (with and without bias comparison) for green InP and CdSe QLEDs

The ITO anode was investigated in conjunction with the layer due to its superior conductivity. The electron concentrations in the PVK and ZnMgO layers were significantly higher than their levels when present individually. However, in the green InP/ZnS QD layer, a remarkable five-order-of-magnitude decrease in electron concentration was observed, contrasting with the electron concentration changes in the CdSe/ZnS QD layer of green CdSe QLEDs. In green InP QLEDs, despite the increase in voltage to 5V, the region of the ZnMgO layer near the Al cathode maintained a high electron concentration, yet the region closer to the QD layer exhibited a reduction, suggesting that electrons may have partially migrated into the QD layer.

Concurrently, the electron concentration in the green InP/ZnS QD layer further decreased, indicating that the injected electrons were not accumulated within this layer.

Owing to the closure of the circuit, electrons in the PVK layer rapidly flowed towards the ITO anode, resulting in a decreased concentration. In green CdSe QLEDs, it was observed that the electron concentration in the QD layer remained above the initial level. This electron leakage phenomenon may be a significant factor contributing to the inferior performance of green InP QLEDs compared to green CdSe QLEDs.

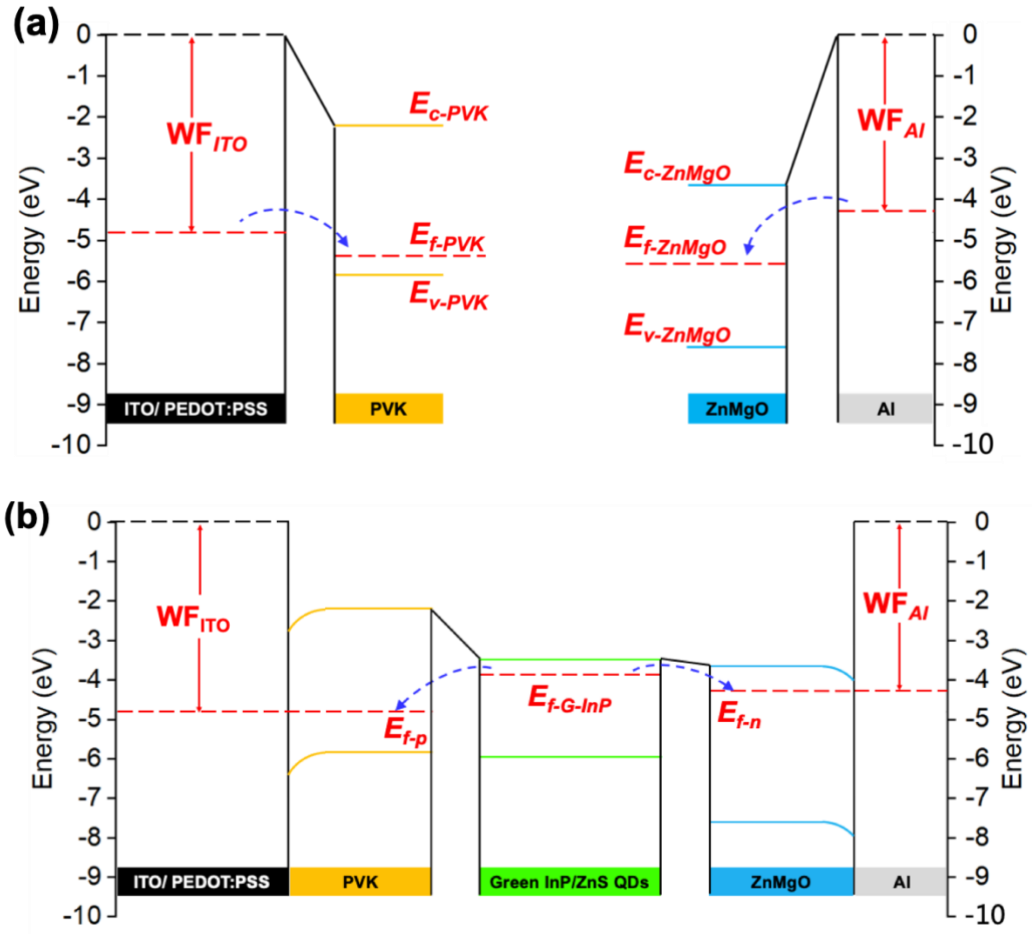

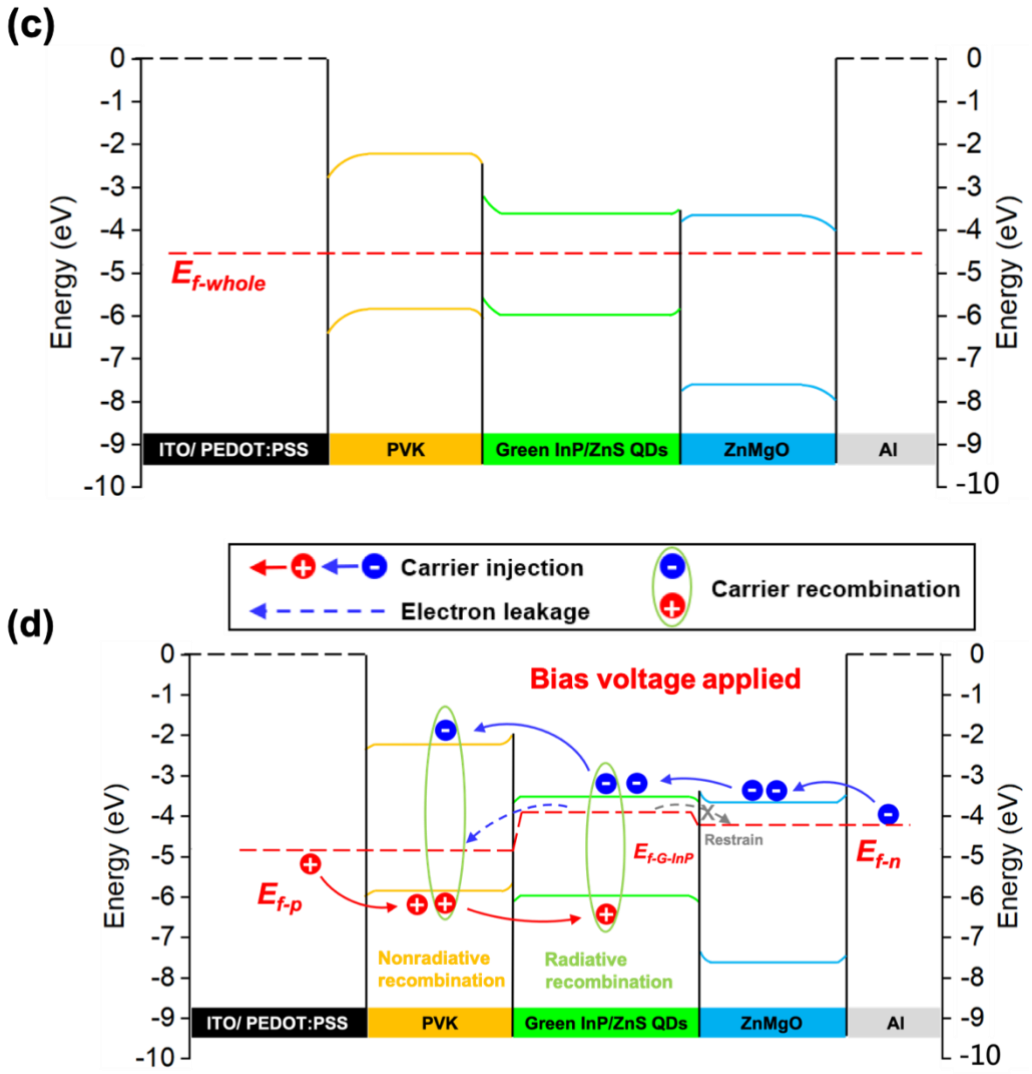

Figure 5.6 Schematic representation of energy band configurations in a green InP QLED at various stages: (a) Prior to contact between the HTL, ETL, and electrodes. (b) HTL and ETL in contact with electrodes, with the QDs layer remaining isolated. (c) An intact green InP QLED without any applied bias voltage. (d) The combined influence of diffusion and migration directing excessive electrons towards the HTL.

Through experimental and simulation studies on green InP QLEDs, we propose a new mechanism to explain electron leakage. In the structure of QLEDs, ITO / PEDOT:PSS and Al form Schottky contacts with PVK and ZnMgO, respectively (Figure 5.6(b)). Due to the difference in Fermi levels between different materials, electrons diffuse from regions with a shallower Fermi level to those with a deeper level, as indicated by the blue dashed lines in the figure. This diffusion leads to a significant increase in the electron concentration in the transport layers, causing the Fermi levels of the HTL and ETL to shift to Ef-p and Ef-n, respectively. Given the shallow Fermi level of the green InP/ZnS QD layer and the high work function of ITO, the Fermi level of the entire device exhibits a step-like distribution from deep to shallow, from Ef-p to Ef-G-InP, and then to Ef-n (Figure 5.6(b)). This energy level arrangement facilitates electron leakage from the ZnMgO/Al interface into the green InP QDs and further migration towards the ITO electrode.

The leaked electrons cause band bending (Figure 5.6(c)), similar to the electron diffusion phenomenon in heterojunctions. Under the action of the built-in electric field at the interface, the system reaches a dynamic equilibrium, preventing further electron leakage. However, when an external bias voltage is applied, the built-in electric field is neutralized, the bands flatten, and electron leakage continues (Figure 5.6(d)). During this process, electrons migrate from the cathode (Al) to the anode (ITO), and the combined effect of diffusion and migration leads to an excess of electrons entering the

HTL, disrupting the carrier balance, increasing non-radiative recombination in the HTL, and ultimately reducing the EQE of the QLED.

In contrast, in green CdSe QLEDs, Ef-p is always higher than Ef-CdSe, causing electrons to preferentially accumulate in the deeper Fermi level of the CdSe/ZnS QDs. This accumulation reduces non-radiative recombination in the HTL, allowing more holes to inject into the QD layer, thereby maintaining the high EQE of green CdSe QLEDs. This contrast reveals the significant impact of different QD materials on device performance, especially in terms of carrier management and non-radiative recombination differences.

5.3 Optimization of LiF interface layer and device performance characterization

5.3.1 Work function tuning and interface physical mechanisms

By modifying the ITO surface with an ultra-thin LiF layer (0.5-2.0 nm), UPS characterization revealed that its work function could be adjusted to as low as 4.41 eV (Figure 5.7). This tuning suppresses electron leakage through the following mechanisms:

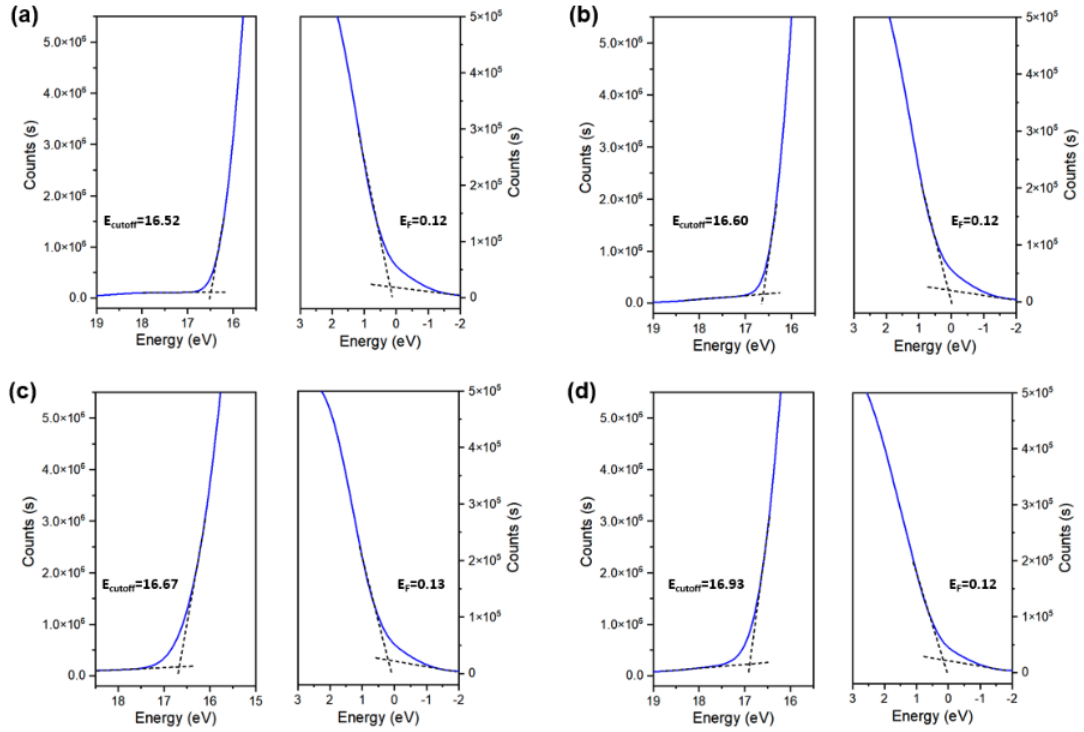

Figure 5.7 UPS results of ITO work function variation with different LiF thicknesses: (a) 0 nm; (b) 0.5 nm; (c) 1.0 nm; and (d) 1.5 nm.

Fermi Level Alignment: Reducing $\Delta\Phi$ to below 0.7 eV decreases the thermal emission electron flux (following the Richardson-Dushman equation: $J \propto T^2\exp(-\Delta\Phi/k_{BT})$)[101]; with Quantum Confinement Effect, the LiF layer (thickness <1 nm) induces the formation of an interface dipole, further reducing the effective barrier height (Figure 5.8(b))[102]; with hole tunneling enhancement: A narrow barrier (~0.3 eV) is formed at the LiF/ PEDOT:PSS interface, enhancing hole injection efficiency under high bias via Fowler-Nordheim tunneling ($J \propto E^2\exp(-B/E)$)[103].

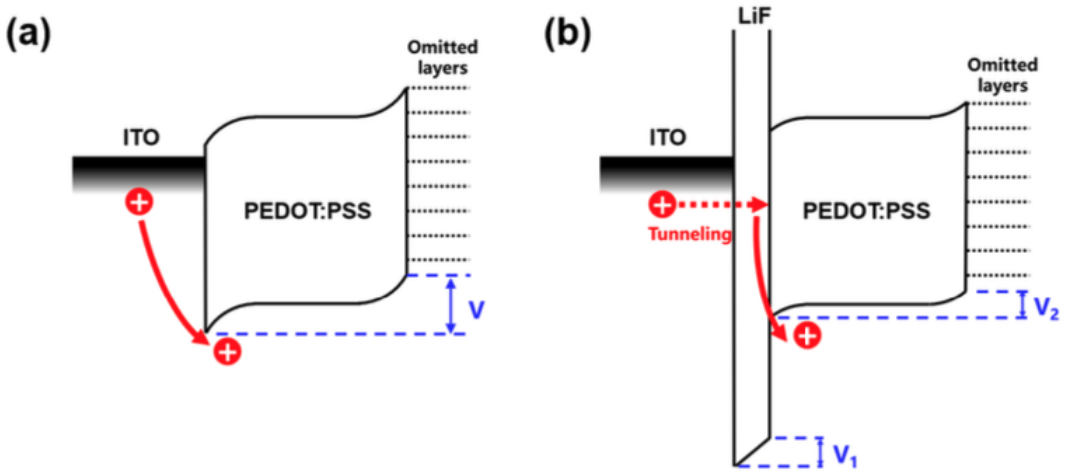

Figure 5.8 UPS results of ITO work function variation with different LiF thicknesses: (a) 0 nm; (b) 0.5 nm; (c) 1.0 nm; and (d) 1.5 nm.

5.3.2 Verification of electroluminescence performance enhancement

QLEDs with the structure ITO / LiF / PEDOT:PSS / PVK / QDs / ZnMgO / Al were fabricated, and the key experimental results are as follows:

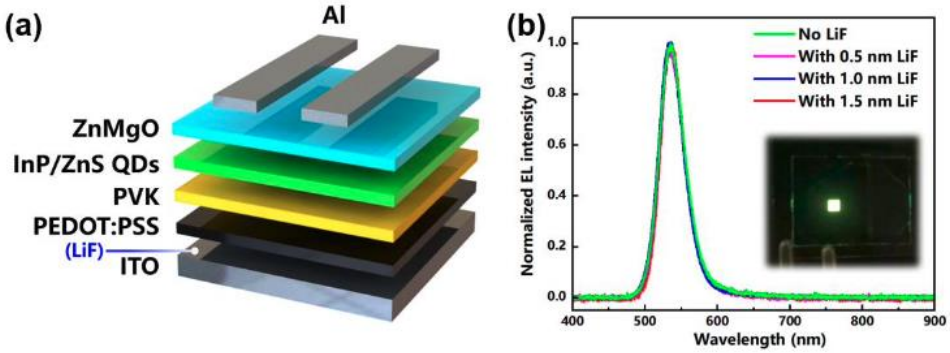

Figure 5.9 The (a)structure and (b)EL spectra of the verified QLEDs.

Luminance and Efficiency: Under the optimal LiF thickness (1.0 nm), the maximum luminance was enhanced from 22.1×10^3 cd/m^2 to 32.4×10^3 cd/m^2 (Figure 5.10(a)), attributed to the increased radiative recombination rate; The maximum EQE increased from 4.70% to 9.14%, and remained at 8.2% under 12.8 mA/cm^2, indicating significant improvement in efficiency roll-off (Figure 5.10(b)).

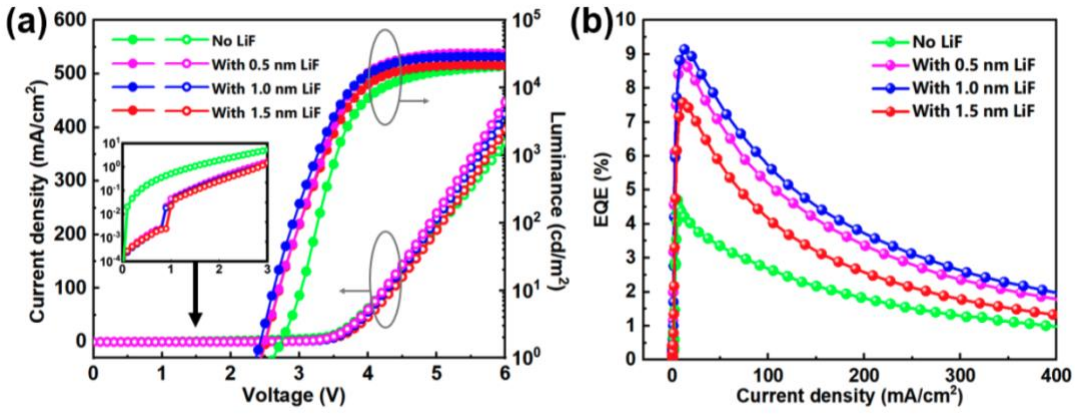

Figure 5.10 The(a)luminance, current density and (b) EQE of devices.

Carrier Injection Balance Analysis: The J-V curves of hole-only devices (HOD) showed that the LiF layer suppressed leakage current (J reduced by 37%) at low bias (<2 V), while at high bias (>3 V), hole tunneling dominated, achieving carrier injection balance (Figure 5.11).

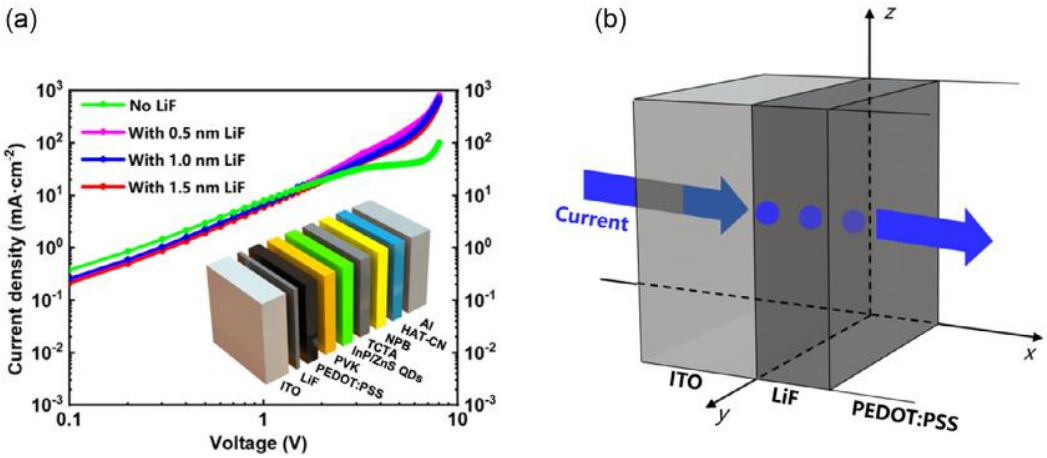

Figure 5.11 (a) The J-V characteristics of hole-only devices and (b) schematic illustration of tunneling mechanisms.

5.4 In-depth discussion and theoretical extensions

5.4.1 Kinetic competition mechanism of electron leakage

The essence of electron leakage is the synergistic effect of diffusion and migration:

Concentration gradient-driven: The significant concentration difference between the QDs layer (~10^{18} cm^{-3}) and the HTL (~10^{12} cm^{-3}) triggers Fickian diffusion (J_{diff} = -D∇n).

Electric field-driven migration: Under bias, electrons are drifted towards the anode by the Lorentz force (J_{drift} = μnE). The competition between these two processes leads to the accumulation of electrons within the HTL, which undergoes Auger

recombination or trap-assisted recombination with injected holes, reducing the radiative efficiency[104].

5.4.2 Kinetic competition mechanism of electron leakage

In addition to work function tuning, the LiF layer optimizes device performance through the following mechanisms:

(1) Defect passivation: Covers ITO surface defects such as oxygen vacancies, reducing carrier scattering[105];

(2) Optical Regulation: The ultra-thin LiF (~1 nm) has a negligible effect on the visible light transmittance ($\Delta T < 2\%$), avoiding optical output loss; Enhanced

(3) Thermal Stability: The high melting point of LiF (~845°C) suppresses interface degradation under high-temperature operation[10].

5.4.3 Comparative analysis with Cadmium-based QLEDs

CdSe QDs have a deep Fermi level (~4.2 eV) that matches well with ITO, naturally confining electrons within the QDs layer. In contrast, the shallow Fermi level of InP QDs leads to an asymmetric behavior where "electron leakage precedes hole injection," highlighting the necessity of band engineering in cadmium-free systems. This discrepancy can be quantitatively described by the modified Shockley-Read-Hall model: $\tau_{SRH}^{-1} = \sigma v_{th} N_t$, where the trap density Nt is higher in the InP system[106].

5.5 Summary

In this study, we systematically explored the carrier behavior in cadmium-free and lead-free InP QLEDs, focusing on the microscopic mechanisms of electron leakage, through a combination of experimental research and multi-physics simulations. We identified the Fermi level mismatch between the ITO anode and InP QDs as a key factor leading to electron escape. To address this issue, we proposed a strategy of using an ultra-thin LiF interface layer to modulate the work function of ITO, which effectively suppressed electron leakage and successfully enhanced the EQE of the devices from 4.70% to 9.14%. Additionally, this strategy also enhanced hole injection through tunneling effects, achieving carrier transport balance and significantly improving the overall performance of the devices.

In our conclusions, we highlighted several key points regarding carrier behavior in cadmium-free and lead-free InP QLEDs: Firstly, electron leakage is one of the main factors limiting device performance, primarily due to the energy level mismatch between the ITO anode and the QDs. Secondly, regulating the work function of ITO through interface engineering can effectively reduce electron leakage while promoting hole injection. Finally, achieving carrier transport balance is crucial for improving the efficiency and stability of QLEDs.

Chapter 6 Conclusion and future works

6.1 Conclusion

Overall, improving light extraction efficiency and optimizing carrier behavior in devices are two key factors in achieving high-performance cadmium-free and lead-free QLEDs. In order to achieve good external quantum efficiency (EQE), we analyze QLED from these two perspectives and propose optimization strategies.

Firstly, we analyzed the light extraction modes within the cadmium-free and lead-free QLEDs and proposed a combined scheme to improve light extraction efficiency under limited internal quantum efficiency (IQE), thereby obtaining higher-performing QLEDs. The thesis presents an effective, comprehensive strategy, involving the addition of an appropriately thick spacer layer, high-index substrates, and substrate surface roughening to sequentially extract light from the SPP mode, waveguide mode, and substrate mode to the air mode of QLEDs. This combined scheme promotes optical transmission between modes within the device through optical tunneling and microcavity design. After optimization, the light extraction efficiency was significantly improved, resulting in an EQE increase from 6.64% to 18.50% for blue ZnSe QLEDs. Approximately threefold EQE improvement provides a more universal optical optimization solution for cadmium-free and lead-free QLEDs.

To address the issue of efficiency reduction due to unbalanced carrier injection in cadmium-free and lead-free QLEDs, an innovative design based on an electric dipole layer was proposed to enhance hole injection. An innovative electric dipole layer material, 2,2'-(perfluoronaphthalene-2,6-diylidene)dimalononitrile (F6-TCNNQ), was also applied to cadmium-free and lead-free QLEDs. The EDL creates a built-in electric field at the HTL/EML interface, enhancing hole injection and improving carrier recombination. The introduction of F6-TCNNQ also optimizes the energy alignment of the interface, reducing the hole injection barrier to EML. This scheme elevates the ZnSeTe blue QLED EQE by 71% (from 7.44% to 12.71%) and provides a universal approach to high-performance cadmium-free and lead-free QLEDs.

In cadmium-free and lead-free QLEDs, there may be electron leakage inside the device, which can lead to carrier imbalance, especially when the EML with a shallow Fermi level. The large Fermi energy difference between QDs and the ITO anode is considered the main driving factor for electron leakage. The path of the leaked electrons has been identified, and a modification strategy using LiF has been proposed, which has been validated by both simulation and experiments. The ultra-thin LiF layer also improves hole injection through the tunneling effect. Green InP QLEDs achieve more balanced carrier injection and 9.14% (from 4.70% to 9.14%) enhanced EQE.

6.2 Future works

Under the impetus of an ever-growing demand for more vibrant visual effects and sustainable solutions, the pursuit of high-performance, energy-efficient display and lighting technologies shows no signs of abating. QLEDs owing to their tunable bandgaps, high PLQY, narrow FWHM, expansive color gamut, cost-effective, solution-based fabrication, and compatibility with inkjet printer fabrication, have emerged as highly competitive contenders of new display technologies. As environmental and human health concerns increasingly capture public attention, the development of cadmium-free and lead-free eco-friendly QLEDs becomes particularly crucial.

Looking forward, our work provides important guidance for further optimizing the performance of cadmium-free and lead-free QLEDs. In future research, we will continue to delve into light extraction and carrier behavior, especially in the following two areas:

In-depth understanding of carrier transport mechanisms: We will further investigate the transport process of carriers between the QD layer and the electrode interface to reveal more factors affecting carrier behavior, providing a theoretical basis for further improvements in device performance.

Combination of interface engineering and material optimization: On the basis of our existing work, we will continue to explore more effective interface control methods and develop new types of organic-inorganic hybrid materials to achieve more efficient hole injection and more balanced carrier transport. Through these efforts, we aim to further enhance the EQE of cadmium-free and lead-free QLEDs and move closer to market applications.

Finally, for our analysis of the three perspectives and three optimization schemes of the device, we will seriously consider the synergistic optimization scheme of light extraction and carrier behavior in the future. Firstly, consider the energy level matching and carrier injection balance in the device structure, and then combine with the thin film preparation process and interface control to select an appropriate optimization scheme. In addition, the conditions applicable to the optimization scheme, including the material properties of each functional layer, should be summarized and considered for use in more optoelectronic devices with similar structures, possibly including different luminescent materials. Last but not least, try to apply the three optimization schemes together in the cadmium-free and lead-free QLED, and adjust the adaptability to get higher performance devices to serve the industry.

In summary, this study provides important scientific and technical support for the development of cadmium-free and lead-free QLEDs. We believe that through continuous research and optimization, cadmium-free and lead-free QLEDs will

demonstrate even better performance, paving the way for new display and lighting technologies in the future.

References

1. Annual Energy Outlook 2023 - U.S. Energy Information Administration (EIA). https://www.eia.gov/outlooks/aeo/index.php.
2. Li, L. & Reiss, P. One-pot Synthesis of Highly Luminescent InP/ZnS Nanocrystals without Precursor Injection. *J. Am. Chem. Soc.* **130**, 11588–11589 (2008).
3. Kim, S. *et al.* Highly Luminescent InP/GaP/ZnS Nanocrystals and Their Application to White Light-Emitting Diodes. *J. Am. Chem. Soc.* **134**, 3804–3809 (2012).
4. Sumanth Kumar, D., Jai Kumar, B. & Mahesh, H. M. Chapter 3 - Quantum Nanostructures (QDs): An Overview. in *Synthesis of Inorganic Nanomaterials* (eds. Mohan Bhagyaraj, S., Oluwafemi, O. S., Kalarikkal, N. & Thomas, S.) 59–88 (Woodhead Publishing, 2018). doi:10.1016/B978-0-08-101975-7.00003-8.
5. Dubertret, B. *et al.* In Vivo Imaging of Quantum Dots Encapsulated in Phospholipid Micelles. *Science* **298**, 1759–1762 (2002).
6. Kairdolf, B. A. *et al.* Semiconductor Quantum Dots for Bioimaging and Biodiagnostic Applications. *Annu. Rev. Anal. Chem.* **6**, 143–162 (2013).
7. Zhou, J., Yang, Y. & Zhang, C. Toward Biocompatible Semiconductor Quantum Dots: From Biosynthesis and Bioconjugation to Biomedical Application. *Chem. Rev.* **115**, 11669–11717 (2015).
8. Meinardi, F., Bruni, F. & Brovelli, S. Luminescent solar concentrators for building-integrated photovoltaics. *Nat. Rev. Mater.* **2**, 1–9 (2017).
9. Carey, G. H. *et al.* Colloidal Quantum Dot Solar Cells. *Chem. Rev.* **115**, 12732–12763 (2015).
10. Ren, A., Yuan, L., Xu, H., Wu, J. & Wang, Z. Recent progress of III–V quantum dot infrared photodetectors on silicon. *J. Mater. Chem. C* **7**, 14441–14453 (2019).
11. Chen, B. *et al.* Low Dark Current High Gain InAs Quantum Dot Avalanche Photodiodes Monolithically Grown on Si. *ACS Photonics* **7**, 528–533 (2020).
12. Park, Y.-S., Roh, J., Diroll, B. T., Schaller, R. D. & Klimov, V. I. Colloidal quantum dot lasers. *Nat. Rev. Mater.* **6**, 382–401 (2021).
13. Caruge, J. M., Halpert, J. E., Wood, V., Bulović, V. & Bawendi, M. G. Colloidal quantum-dot light-emitting diodes with metal-oxide charge transport layers. *Nat. Photonics* **2**, 247–250 (2008).
14. Lim, J., Park, Y.-S. & Klimov, V. I. Optical gain in colloidal quantum dots achieved with direct-current electrical pumping. *Nat. Mater.* **17**, 42–49 (2018).
15. Dai, X., Deng, Y., Peng, X. & Jin, Y. Quantum-Dot Light-Emitting Diodes for Large-Area Displays: Towards the Dawn of Commercialization. *Adv. Mater.* **29**, 1607022 (2017).
16. Shen, H. *et al.* Visible quantum dot light-emitting diodes with simultaneous high brightness and efficiency. *Nat. Photonics* **13**, 192–197 (2019).

17. Chow, W. W. & Jahnke, F. On the physics of semiconductor quantum dots for applications in lasers and quantum optics. *Prog. Quantum Electron.* **37**, 109–184 (2013).
18. Shu, Y. *et al.* Quantum Dots for Display Applications. *Angew. Chem.* **132**, 22496–22507 (2020).
19. Pietryga, J. M. *et al.* Spectroscopic and Device Aspects of Nanocrystal Quantum Dots. *Chem. Rev.* **116**, 10513–10622 (2016).
20. Dai, X. *et al.* Solution-processed, high-performance light-emitting diodes based on quantum dots. *Nature* **515**, 96–99 (2014).
21. Zhang, H., Sun, X. & Chen, S. Over 100 cd A−1 Efficient Quantum Dot Light-Emitting Diodes with Inverted Tandem Structure. *Adv. Funct. Mater.* **27**, 1700610 (2017).
22. Zhang, H., Chen, S. & Sun, X. W. Efficient Red/Green/Blue Tandem Quantum-Dot Light-Emitting Diodes with External Quantum Efficiency Exceeding 21%. *ACS Nano* **12**, 697–704 (2018).
23. Wu, Z., Liu, P., Zhang, W., Wang, K. & Sun, X. W. Development of InP Quantum Dot-Based Light-Emitting Diodes. *ACS Energy Lett.* **5**, 1095–1106 (2020).
24. Liu, X.-K. *et al.* Metal halide perovskites for light-emitting diodes. *Nat. Mater.* **20**, 10–21 (2021).
25. Wang, Y. *et al.* Spectrally stable blue electroluminescence of mixed-halide perovskite light-emitting diodes featuring ion migration inhibition. *Org. Electron.* **86**, 105919 (2020).
26. Brunetti, V. *et al.* InP/ZnS as a safer alternative to CdSe/ZnS core/shell quantum dots : in vitro and in vivo toxicity assessment. *Nanoscale* **5**, 307–317 (2013).
27. Directive - 2011/65 - EN - rohs 2 - EUR-Lex. https://eur-lex.europa.eu/eli/dir/2011/65/oj.
28. European Commission To Prohibit Cadmium From TVs And Displays By October 2019 | Printed Electronics Now. https://www.printedelectronicsnow.com/contents/view_breaking-news/2017-08-09/european-commission-to-prohibit-cadmium-from-tvs-and-displays-by-october-2019/.
29. Battaglia, D. & Peng, X. Formation of High Quality InP and InAs Nanocrystals in a Noncoordinating Solvent. *Nano Lett.* **2**, 1027–1030 (2002).
30. Wen, Z. *et al.* Color revolution: toward ultra-wide color gamut displays. *J. Phys. Appl. Phys.* **54**, 213002 (2021).
31. Chen, J., Hardev, V., Hartlove, J., Hofler, J. & Lee, E. 66.1: Distinguised Paper: A High-Efficiency Wide-Color-Gamut Solid-State Backlight System for LCDs Using Quantum Dot Enhancement Film. *SID Symp. Dig. Tech. Pap.* **43**, 895–896 (2012).
32. Colvin, V. L., Schlamp, M. C. & Alivisatos, A. P. Light-emitting diodes made from cadmium selenide nanocrystals and a semiconducting polymer. *Nature* **370**, 354–357 (1994).

33. Hao, J. *et al.* A facile route to synthesize CdSe/ZnS thick-shell quantum dots with precisely controlled green emission properties: towards QDs based LED applications. *Sci. Rep.* **9**, 12048 (2019).
34. Cao, W. *et al.* Highly stable QLEDs with improved hole injection via quantum dot structure tailoring. *Nat. Commun.* **9**, 2608 (2018).
35. Jo, J.-H. *et al.* Photostability enhancement of InP/ZnS quantum dots enabled by In2O3 overcoating. *J. Alloys Compd.* **647**, 6–13 (2015).
36. Liu, H. *et al.* Near-infrared lead chalcogenide quantum dots: Synthesis and applications in light emitting diodes*. *Chin. Phys. B* **28**, 128504 (2019).
37. Song, J. *et al.* Quantum Dot Light-Emitting Diodes Based on Inorganic Perovskite Cesium Lead Halides (CsPbX3). *Adv. Mater. Deerfield Beach Fla* **27**, 7162–7167 (2015).
38. Li, X. *et al.* CsPbX3 Quantum Dots for Lighting and Displays: Room-Temperature Synthesis, Photoluminescence Superiorities, Underlying Origins and White Light-Emitting Diodes. *Adv. Funct. Mater.* **26**, 2435–2445 (2016).
39. Li, Z. *et al.* Modulation of recombination zone position for quasi-two-dimensional blue perovskite light-emitting diodes with efficiency exceeding 5%. *Nat. Commun.* **10**, 1027 (2019).
40. Qi, H. *et al.* Research progress and challenges of blue light-emitting diodes based on II–VI semiconductor quantum dots. *J. Mater. Chem. C* **8**, 10160–10173 (2020).
41. Ossila | Low Price Lab Equipment & Materials | Enabling Science. *Ossila* https://www.ossila.com/.
42. Stouwdam, J. W. & Janssen, R. A. J. Red, green, and blue quantum dot LEDs with solution processable ZnO nanocrystal electron injection layers. *J. Mater. Chem.* **18**, 1889–1894 (2008).
43. Manders, J. R. *et al.* High efficiency and ultra-wide color gamut quantum dot LEDs for next generation displays. *J. Soc. Inf. Disp.* **23**, 523–528 (2015).
44. Mashford, B. S. *et al.* High-efficiency quantum-dot light-emitting devices with enhanced charge injection. *Nat. Photonics* **7**, 407–412 (2013).
45. Shen, W. *et al.* Synthesis of highly fluorescent InP/ZnS small-core/thick-shell tetrahedral-shaped quantum dots for blue light-emitting diodes. *J. Mater. Chem. C* **5**, 8243–8249 (2017).
46. Zhang, H. *et al.* High-Brightness Blue InP Quantum Dot-Based Electroluminescent Devices: The Role of Shell Thickness. *J. Phys. Chem. Lett.* **11**, 960–967 (2020).
47. Zhang, W. *et al.* InP/ZnS/ZnS Core/Shell Blue Quantum Dots for Efficient Light-Emitting Diodes. *Adv. Funct. Mater.* **30**, 2005303 (2020).
48. Kim, K.-H. *et al.* Cation-Exchange-Derived InGaP Alloy Quantum Dots toward Blue Emissivity. *Chem. Mater.* **32**, 3537–3544 (2020).
49. Xiang, C. *et al.* Solution processed multilayer cadmium-free blue/violet emitting quantum dots light emitting diodes. *Appl. Phys. Lett.* **101**, 053303 (2012).
50. Ji, W. *et al.* High color purity ZnSe/ZnS core/shell quantum dot based blue light emitting diodes with an inverted device structure. *Appl. Phys. Lett.* **103**, 053106 (2013).

51. Wang, A. *et al.* Bright, efficient, and color-stable violet ZnSe-based quantum dot light-emitting diodes. *Nanoscale* **7**, 2951–2959 (2015).
52. Jang, E.-P. *et al.* Synthesis of Alloyed ZnSeTe Quantum Dots as Bright, Color-Pure Blue Emitters. *ACS Appl. Mater. Interfaces* **11**, 46062–46069 (2019).
53. Park, S. *et al.* Development of highly efficient blue-emitting ZnSexTe1-x/ZnSe/ZnS quantum dots and their electroluminescence application. *J. Ind. Eng. Chem.* **88**, 348–355 (2020).
54. Kim, T. *et al.* Efficient and stable blue quantum dot light-emitting diode. *Nature* **586**, 385–389 (2020).
55. COMSOL: Multiphysics Software for Optimizing Designs. *COMSOL* https://www.comsol.com/.
56. Piprek, J. Simulation of GaN-based Light-Emitting Devices. in *Simulation of Semiconductor Processes and Devices 2004* (eds. Wachutka, G. & Schrag, G.) 101–108 (Springer Vienna, Vienna, 2004). doi:10.1007/978-3-7091-0624-2_25.
57. Advanced Modeling of Solar Cells and OLEDs. *Fluxim* https://www.fluxim.com/setfos-intro.
58. Fischetti, M. V., Laux, S. E. & Lee, W. Monte Carlo simulation of hot-carrier transport in real semiconductor devices. *Solid-State Electron.* **32**, 1723–1729 (1989).
59. Goldstein, J. I. *et al. Scanning Electron Microscopy and X-Ray Microanalysis*. (Springer, 2017).
60. Reimer, L. Scanning Electron Microscopy: Physics of Image Formation and Microanalysis, Second Edition. *Meas. Sci. Technol.* **11**, 1826 (2000).
61. Skoog, D. A., Holler, F. J. & Crouch, S. R. *Principles of Instrumental Analysis*. (Cengage Learning, 2017).
62. Perkampus, H.-H. *UV-VIS Spectroscopy and Its Applications*. (Springer Science & Business Media, 2013).
63. Würth, C., Geissler, D., Behnke, T., Kaiser, M. & Resch-Genger, U. Critical review of the determination of photoluminescence quantum yields of luminescent reporters. *Anal. Bioanal. Chem.* **407**, 59–78 (2015).
64. de Mello, J. C., Wittmann, H. F. & Friend, R. H. An improved experimental determination of external photoluminescence quantum efficiency. *Adv. Mater.* **9**, 230–232 (1997).
65. Hüfner, S. *Photoelectron Spectroscopy: Principles and Applications*. (Springer Science & Business Media, 2003).
66. Seah, M. P. & Dench, W. A. Quantitative electron spectroscopy of surfaces: A standard data base for electron inelastic mean free paths in solids. *Surf. Interface Anal.* **1**, 2–11 (1979).
67. Mustafa, H. A. M. & Jameel, D. A. Modeling and the main stages of spin coating process: A review. *J. Appl. Sci. Technol. Trends* **2**, 119–123 (2021).
68. Ohring, M. *Materials Science of Thin Films: Depositon and Structure*. (Academic Press, 2002).

69. Venables, J. *Introduction to Surface and Thin Film Processes*. (Cambridge University Press, 2000).
70. Manova, D., Gerlach, J. W. & Mändl, S. Thin Film Deposition Using Energetic Ions. *Materials* **3**, 4109–4141 (2010).
71. Schubert, E. F. *Light-Emitting Diodes (3rd Edition, 2018)*. (E. Fred Schubert, 2018).
72. *Thin Film Transistors*.
73. Meng, S.-S., Li, Y.-Q. & Tang, J.-X. Theoretical perspective to light outcoupling and management in perovskite light-emitting diodes. *Org. Electron.* **61**, 351–358 (2018).
74. Meerheim, R., Furno, M., Hofmann, S., Lüssem, B. & Leo, K. Quantification of energy loss mechanisms in organic light-emitting diodes. *Appl. Phys. Lett.* **97**, 253305 (2010).
75. LAN, L.-H. *et al.* Progress of Light Extraction Technology for Organic Light-Emitting Diodes. *Acta Phys.-Chim. Sin.* **33**, 1548–1572 (2017).
76. Cho, C.-Y. *et al.* Enhanced light extraction in light-emitting diodes with photonic crystal structure selectively grown on p-GaN. *Appl. Phys. Lett.* **96**, 181110 (2010).
77. Chen, S. & Kwok, H. S. Light extraction from organic light-emitting diodes for lighting applications by sand-blasting substrates. *Opt. Express* **18**, 37–42 (2010).
78. Zhou, J. *et al.* Roughening the white OLED substrate's surface through sandblasting to improve the external quantum efficiency. *Org. Electron.* **12**, 648–653 (2011).
79. Möller, S. & Forrest, S. R. Improved light out-coupling in organic light emitting diodes employing ordered microlens arrays. *J. Appl. Phys.* **91**, 3324–3327 (2002).
80. Kim, H. S. *et al.* Novel fabrication method of microlens arrays with High OLED outcoupling efficiency. *Opt. Laser Technol.* **77**, 104–110 (2016).
81. Huang, Y.-H. *et al.* Enhancing light out-coupling of organic light-emitting devices using indium tin oxide-free low-index transparent electrodes. *Appl. Phys. Lett.* **104**, 183302 (2014).
82. Hsu, C. M., Zeng, Y. X., Lin, B. T., Lin, W. M. & Wu, W. T. Enhanced light extraction of organic light-emitting diodes using recessed anodes. *Appl. Surf. Sci.* **309**, 33–37 (2014).
83. Do, Y. r. *et al.* Enhanced Light Extraction from Organic Light-Emitting Diodes with 2D SiO2/SiN Photonic Crystals. *Adv. Mater.* **15**, 1214–1218 (2003).
84. Xiao, Y. *et al.* Surface plasmon-enhanced electroluminescence in organic light-emitting diodes incorporating Au nanoparticles. *Appl. Phys. Lett.* **100**, 013308 (2012).
85. Shen, H. *et al.* Phosphine-free synthesis of high quality ZnSe, ZnSe/ZnS, and Cu-, Mn-doped ZnSe nanocrystals. *Dalton Trans.* 10534 (2009) doi:10.1039/b917674h.
86. Gong, K. & Kelley, D. F. Lattice Strain Limit for Uniform Shell Deposition in Zincblende CdSe/CdS Quantum Dots. *J. Phys. Chem. Lett.* **6**, 1559–1562 (2015).
87. Han, C.-Y. *et al.* More Than 9% Efficient ZnSeTe Quantum Dot-Based Blue Electroluminescent Devices. *ACS Energy Lett.* **5**, 1568–1576 (2020).

88. Sun, Y. *et al.* Efficient quantum dot light-emitting diodes with a $Zn_{0.85}$ $Mg_{0.15}$ O interfacial modification layer. *Nanoscale* **9**, 8962–8969 (2017).
89. Zhang, Z. *et al.* High-Performance, Solution-Processed, and Insulating-Layer-Free Light-Emitting Diodes Based on Colloidal Quantum Dots. *Adv. Mater.* **30**, 1801387 (2018).
90. Kim, H.-M., Cho, S., Kim, J., Shin, H. & Jang, J. Li and Mg Co-Doped Zinc Oxide Electron Transporting Layer for Highly Efficient Quantum Dot Light-Emitting Diodes. *ACS Appl. Mater. Interfaces* **10**, 24028–24036 (2018).
91. Bao, Z. *et al.* ZnSe:Te/ZnSeS/ZnS nanocrystals: an access to cadmium-free pure-blue quantum-dot light-emitting diodes. *Nanoscale* **12**, 11556–11561 (2020).
92. Zhang, F. & Kahn, A. Investigation of the High Electron Affinity Molecular Dopant F6-TCNNQ for Hole-Transport Materials. *Adv. Funct. Mater.* **28**, 1703780 (2018).
93. Shaw, P. E., Ruseckas, A. & Samuel, I. D. W. Distance dependence of excitation energy transfer between spacer-separated conjugated polymer films. *Phys. Rev. B* **78**, 245201 (2008).
94. The Stationary Semiconductor Device Equations | SpringerLink. https://link.springer.com/book/10.1007/978-3-7091-3678-2.
95. Miller, A. & Abrahams, E. Impurity Conduction at Low Concentrations. *Phys. Rev.* **120**, 745–755 (1960).
96. Evarestov, R. A., Kitaev, Yu. E., Limonov, M. F. & Panfilov, A. G. Optical Phonons and Their Role in High-Tc Superconductivity Mechanism. *Phys. Status Solidi B* **179**, 249–297 (1993).
97. Lim, J. *et al.* InP@ZnSeS, Core@Composition Gradient Shell Quantum Dots with Enhanced Stability. *Chem. Mater.* **23**, 4459–4463 (2011).
98. Yang, X. *et al.* Full visible range covering InP/ZnS nanocrystals with high photometric performance and their application to white quantum dot light-emitting diodes. *Adv. Mater. Deerfield Beach Fla* **24**, 4180–4185 (2012).
99. Physics of Semiconductor Devices | Wiley Online Books. https://onlinelibrary.wiley.com/doi/book/10.1002/0470068329.
100. Deng, Y. *et al.* Deciphering exciton-generation processes in quantum-dot electroluminescence. *Nat. Commun.* **11**, 2309 (2020).
101. Rhoderick, E. H. *Metal-Semiconductor Contacts*. (Clarendon Press, 1978).
102. Zhou, L. *et al.* Screen-Printed Poly(3,4-Ethylenedioxythiophene):Poly(Styrenesulfonate) Grids as ITO-Free Anodes for Flexible Organic Light-Emitting Diodes. *Adv. Funct. Mater.* **28**, 1705955 (2018).
103. Electron emission in intense electric fields. *Proc. R. Soc. Lond. Ser. Contain. Pap. Math. Phys. Character* (1928) doi:10.1098/rspa.1928.0091.
104. Xing, J. *et al.* Vapor Phase Synthesis of Organometal Halide Perovskite Nanowires for Tunable Room-Temperature Nanolasers. *Nano Lett.* **15**, 4571–4577 (2015).

105. Kim, Y. H. *et al.* Highly Conductive PEDOT:PSS Electrode with Optimized Solvent and Thermal Post-Treatment for ITO-Free Organic Solar Cells. *Adv. Funct. Mater.* **21**, 1076–1081 (2011).
106. Shockley, W. The Theory of p-n Junctions in Semiconductors and p-n Junction Transistors. *Bell Syst. Tech. J.* **28**, 435–489 (1949).